JOURNAL OF GEOPHYSICAL RESEARCH, VOL. 96, NO. B11, PAGES 18,147–18,182, OCTOBER 10, 1991

Constraints on Upper Mantle Discontinuities From Observations of Long-Period Reflected and Converted Phases

PETER M. SHEARER

Institute of Geophysics and Planetary Physics, University of California, San Diego, La Jolla

Stacked images combining over 5 years of long-period Global Digital Seismograph Network data reveal many phases associated with reflections and conversions from upper mantle discontinuities. These images show travel time and amplitude relative to a reference phase which is aligned and normalized on all seismograms prior to stacking. Results obtained for P, S, SS, and PP reference arrivals resolve numerous phases from discontinuities near 410 and 660 km, while some of the stacks also show evidence for a weaker discontinuity near 520 km. Phases of particular interest include P and SH multiples resulting from topside reflections, precursors to SS from underside reflections, and P-to-SV converted phases. These phases can be clearly seen both in the waveform stacks and in cross-correlation analysis of individual seismograms. Travel times for these arrivals are converted to discontinuity depths relative to velocities in the Preliminary Reference Earth Model, and empirical corrections are applied for the effects of lateral velocity variations in the upper mantle. Average apparent depths to the discontinuities for the different phases agree to within ±3 km for the 410-km discontinuity, to within ±4 km for the 520-km discontinuity, and to within ±8 km for the 660-km discontinuity. The best global averages are obtained from the SS precursor data which indicate discontinuities at 415, 519, and 659 km. Discontinuity depths obtained from the P-to-SV converted phases at over 35 individual seismic stations exhibit variations of less than ±20 km. Apparent depths to the 660-km discontinuity consistently show greater variability than depths to the 410-km discontinuity, supporting recent laboratory results which indicate that the Clapeyron slope for the 660-km discontinuity is significantly larger in magnitude than the slope for the 410-km discontinuity. Precursors to SS (seen between 110° and 180°) are particularly useful for mapping possible lateral variations in discontinuity depths since each arrival can be associated with a single underside reflection point. Apparent discontinuity depths computed from SS precursors for different tectonic regions agree to within about ±5 km. The SS precursors have especially good coverage near the subducting slabs in the northwest Pacific. Analysis of apparent discontinuity depths in this area suggests the presence of a broad 1000- to 1500-km-wide region near the slab in which the 660-km discontinuity is depressed by about 20 km. Measuring absolute amplitudes for these phases is difficult due to the large corrections required to compensate for the effects of incoherent stacking. Relative amplitude analysis suggests that the P and S wave impedance changes at 410 km are about 0.8–1.1 times the size of the changes at 660 km and that the contrasts at 520 km are between 0.3 and 0.6 of the changes at 410 km.

INTRODUCTION

Seismic evidence for discontinuities in the upper mantle began over 50 years ago with the recognition of a sharp bend in the P wave travel time curve near 20° range [*Byerly*, 1926; *Jeffreys*, 1936]. Discontinuities near 410 and 660 km are now a standard feature of almost all upper mantle velocity models, based on detailed travel time and synthetic seismogram analyses of both P and S wave phases. However, there is not yet general agreement concerning the the brightness, sharpness, and depth distribution of these features or of the possible existence of additional discontinuities. Knowledge of these details, and relating them to the results of high-pressure mineral physics experiments, is crucial in determining the thermal and chemical structure of the upper mantle and helping to answer fundamental and controversial questions in mantle chemistry and dynamics. Do the discontinuities result purely from phase changes or do compositional changes also occur? Is there whole mantle convection, stratified convection, or some intermediate convection regime? Do slabs penetrate into the lower mantle? Reviews of these topics are given by *Silver et al.* [1988], *Jeanloz* [1989], *Jordan et al.* [1989], and *Olson et al.* [1990].

The 410- and 660-km discontinuities have also been detected from observations of secondary arrivals resulting from topside P reflections [e.g., *Nguyen-Hai*, 1963; *Husebye and Madariaga*, 1970; *Davies et al.*, 1971; *Gutowski and Kanesewich*, 1974; *Ward*, 1978], bottomside P reflections [e.g., *Engdahl and Flinn*, 1969; *Bolt*, 1970; *Adams*, 1971; *Husebye et al.*, 1977; *Nakanishi*, 1988; *Wajeman*, 1988; *Davis et al.*, 1989], P-to-S conversions at discontinuities beneath the receivers [e.g., *Vinnik*, 1977; *Vinnik et al.*, 1983; *Paulssen*, 1985, 1988; *Kind and Vinnik*, 1988], near-receiver S-to-P and/or near-source P-to-S conversions [e.g., *Faber and Müller*, 1980, 1984; *Baumgardt and Alexander*, 1984; *Bock*, 1988], and near-source S-to-P conversions [e.g., *Barley et al.*, 1982; *Bock and Ha*, 1984; *Richards and Wicks*, 1990]. These observations are valuable because they can provide better lateral resolution and, at least at short periods, give better constraints on the sharpness of discontinuities than is possible from travel time analyses (the term "discontinuity" will be used loosely in this paper to refer to either a sharp interface or an enhanced velocity gradient steep enough to reflect seismic energy within a frequency band of interest). However, since the discontinuities are fairly weak (less than 10% velocity changes), these are low-amplitude arrivals which are difficult to observe, particularly at intermediate- to high-frequencies (above 0.1 Hz). At lower frequencies it appears that these phases are more easily seen due to the greater coherence of the long-period waveforms. *Revenaugh and Jordan* [1987, 1989, 1991*a*,*b*] have established the existence of discontinuity reflections in long-period ScS multiples for a variety of paths around deep focus events in the southwest Pacific.

This paper presents details of a global body wave stacking

Paper number 91JB01592.
0148-0227/91/91JB-01592$05.00

technique, first described by *Shearer* [1990], which directly images a large number of upper mantle discontinuity phases. The method works by normalizing the time and amplitude of each seismogram prior to stacking by aligning a reference phase. Stacks of over 5 years of long-period Global Digital Seismograph Network (GDSN) data clearly show many phases caused by reflections and conversions at discontinuities in the upper mantle at depths of about 410, 520, and 660 km. Some of these phases are particularly well resolved and suited for more detailed analysis. These include *P*-to-*SV* converted phases which follow *P* on the radial component, *P* and *S* wave multiples off the top of the discontinuities, and precursors to *SS* resulting from bottomside reflections. In many cases, discontinuity phases can be identified on individual seismograms, providing constraints regarding possible lateral variations in discontinuity depths and amplitudes. Results are obtained both for global averages and for specific regions.

The *P* and *SH* wave stacks shown in this paper differ somewhat from earlier versions shown by *Shearer* [1990]. The current stacks contain more data and have clearer images due to the application of a median filter to smooth the image. A different stacking procedure which uses an automatic gain control (AGC) algorithm is described by *Shearer* [1991]. The AGC method permits direct imaging of complete global seismic record sections but shows much less detail in particular regions than the reference phase method described here. Most of the upper mantle discontinuity phases shown in this paper cannot be seen in the AGC images.

GDSN Data Set

Data from the GDSN have recently become available on optical disk (CD-ROM), the most convenient format for automatic processing of large portions of the data set. The results shown in this paper are derived from the first five of these CDs, which contain events greater than magnitude 5.5 from January 1980 through September 1985. This data set contains 46,763 three-component long-period seismograms from 2115 events. However, in order to avoid complications due to depth phases (near-source reflections off the free surface), only events shallower than 50 km are used in the stacks shown here. This limits the data to 32,376 seismograms from 1474 events (about 22 stations per event). Figure 1 shows the event and station locations for the seismograms considered in this paper. These locations are typical of global seismic data sets, with seismic stations sited mostly on the continents and earthquakes occurring mainly along plate boundaries. Only a fraction of the source-receiver

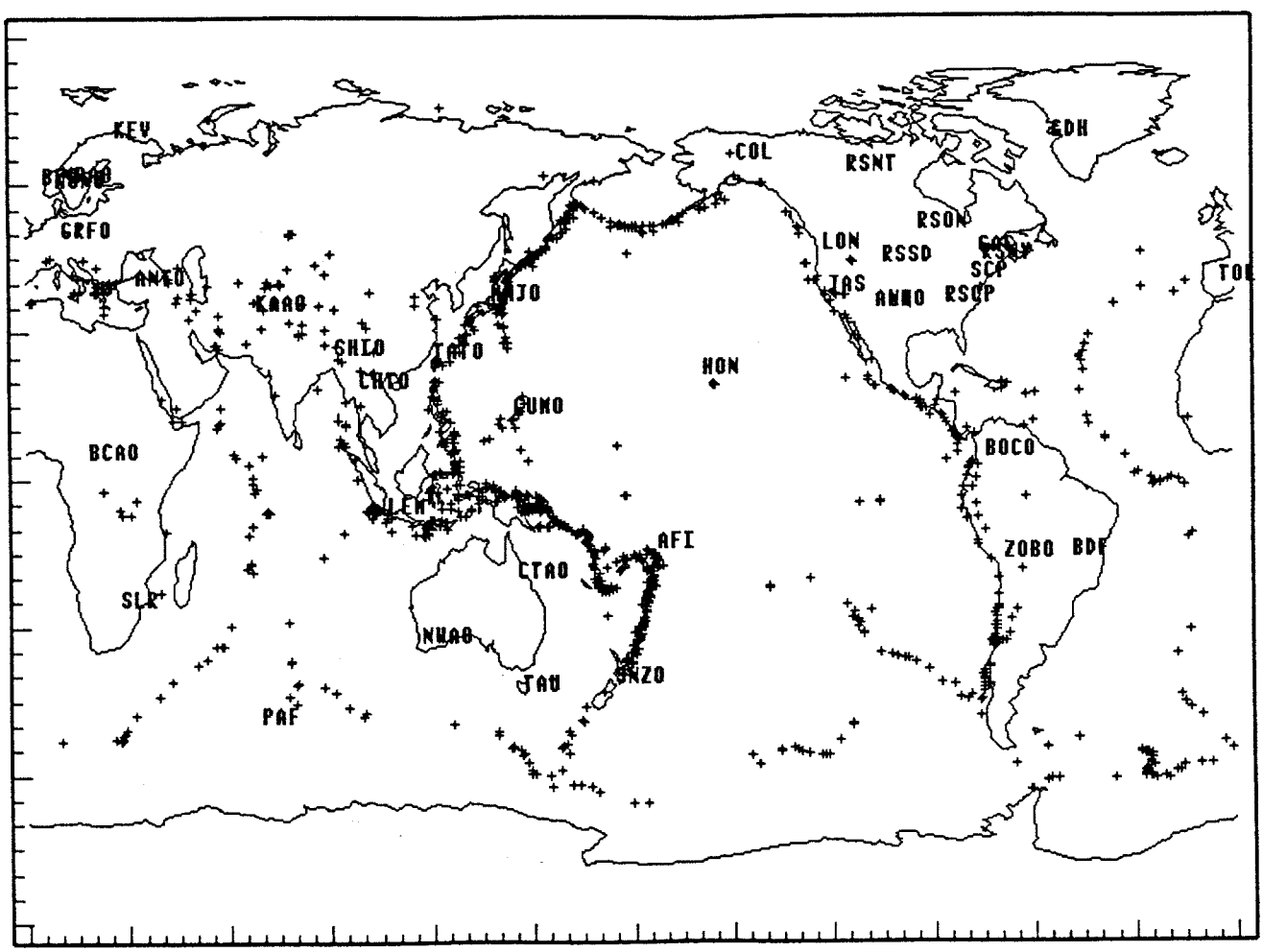

Fig. 1. Source and receiver locations for the GDSN seismograms used in this paper. The GDSN long-period data contain 1474 shallow events (less than 50 km deep) between January 1980 and September 1985. Seismic stations are indicated by their names.

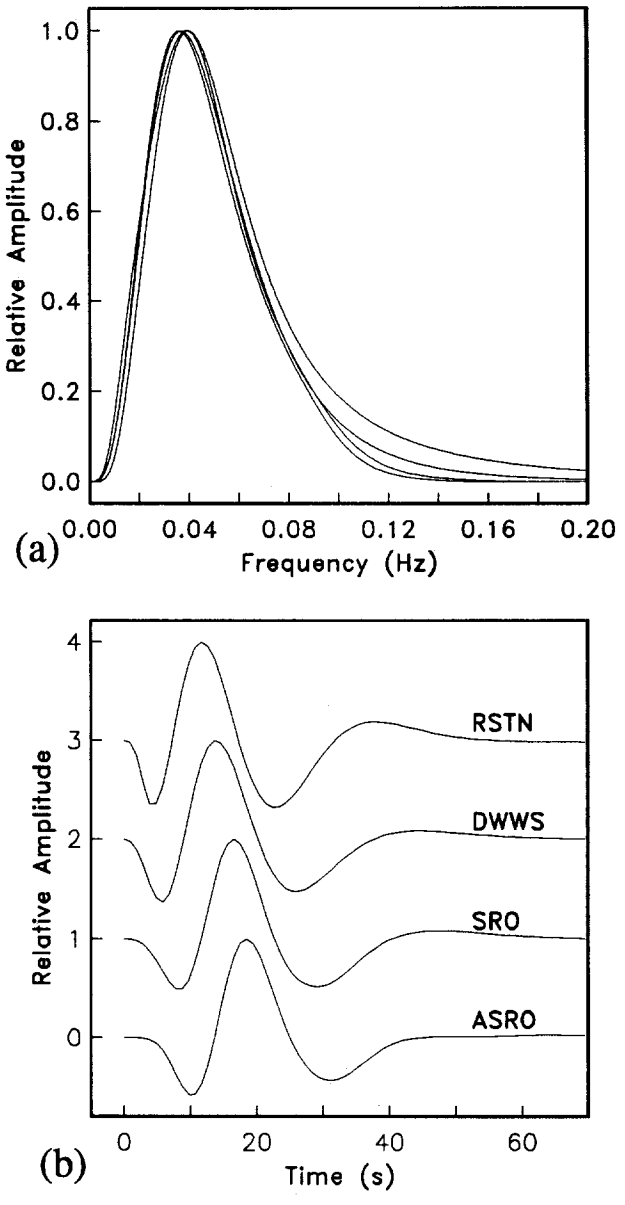

Fig. 2. The response of four different long-period GDSN instruments, showing (*a*) frequency response and (*b*) impulse response to a delta function at zero time.

pairs shown in this plot are actually used in the stacks, since seismograms are used only if they exceed a threshold signal-to-noise ratio (see below).

My analysis is limited to the long-period GDSN data, which record three components (vertical and two horizontals) sampled at 1 Hz. Long-period seismic data are particularly suited for stacking because of the coherence and simplicity of typical long-period waveforms. The GDSN long-period data contain seismograms from four major instrument types (Regional Seismic Test Network (RSTN), Digital World Wide Standardized Seismograph Network (DWWS), Seismic Research Observatory (SRO), and Abbreviated SRO (ASRO)). Figure 2 shows the spectral sensitivity and impulse response for each instrument. The frequency response is very similar, strongly peaked at about 25-s period with little sensitivity above 10 s. The largest difference between the instruments is a phase lag of several seconds which can be seen in the impulse response functions (Figure 2*b*). The stacking procedure corrects for these phase shifts by aligning a reference phase. The remaining differences in the waveforms are relatively minor and are ignored for the results shown here.

STACKING PROCEDURE

A reference phase is used to normalize the amplitude and phase of each seismogram prior to stacking. This eliminates the need to scale seismograms by source size and range, while preserving amplitude and polarity information (relative to the reference phase). This procedure is ideal for resolving upper mantle discontinuity phases, since they usually follow or precede a major seismic arrival which can be used as a reference. The stacking method works as follows:

1. The analysis is restricted to events shallower than 50 km to eliminate complications due to depth phases. Differences in depth shallower than 50 km cause variations in the long-period waveforms but do not show up as separate pulses.

2. The amplitude and start time of each seismogram are normalized with respect to a reference seismic phase. This procedure increases the coherence of the stack and reduces the effects of differing source functions and instrument responses and errors in earthquake depths and origin times. *P*, *S*, *SS*, and *PP* reference arrivals are used in the stacks shown in this paper.

3. The maximum amplitude in the seismogram is found within 60-s windows both preceding and following the theoretical arrival time of the reference phase. These amplitudes are used as a measure of the size of the noise level before the reference phase arrival and of the signal contained in the reference phase. The seismogram is discarded if the signal-to-noise ratio is less than 10 (*P* and *S* reference phases) or 5 (*SS* and *PP* reference phases). This ensures that only the higher-quality data are used in the stack.

4. The amplitude scaling and start time of each seismogram are adjusted such that the maximum amplitude of the reference phase is unity at zero time. The polarity of the seismogram is switched if necessary. This has the effect of aligning the peaks in the reference phase for all the seismograms in the stack.

5. Values obtained from each trace are averaged within bins of range and travel time to produce a stacked record section combining all the data.

6. To smooth and reduce noise in the image, a median filter is applied which replaces each array value by the median of the 9-point square centered on the data value. An example showing the application of this filter is given by *Shearer* [1991].

7. The results are shown in a display in which positive and negative amplitudes are represented with different colors so that the polarity and phase of the various arrivals can be seen directly.

This procedure is illustrated in Figure 3 which shows seismograms before and after alignment. Figure 3*a* shows unaligned *SH* seismograms for stations at source-receiver ranges between 73.9° and 74.9° from January 1980 to September 1981. The dashed lines show a 1-min window beginning at the theoretical *S* arrival time. *SS* can be seen arriving several minutes later. These seismograms satisfy the signal-to-noise criteria; the maximum amplitude in the 1-min window shown is at least 10 times greater than the maximum amplitude in the preceding minute. Notice that the

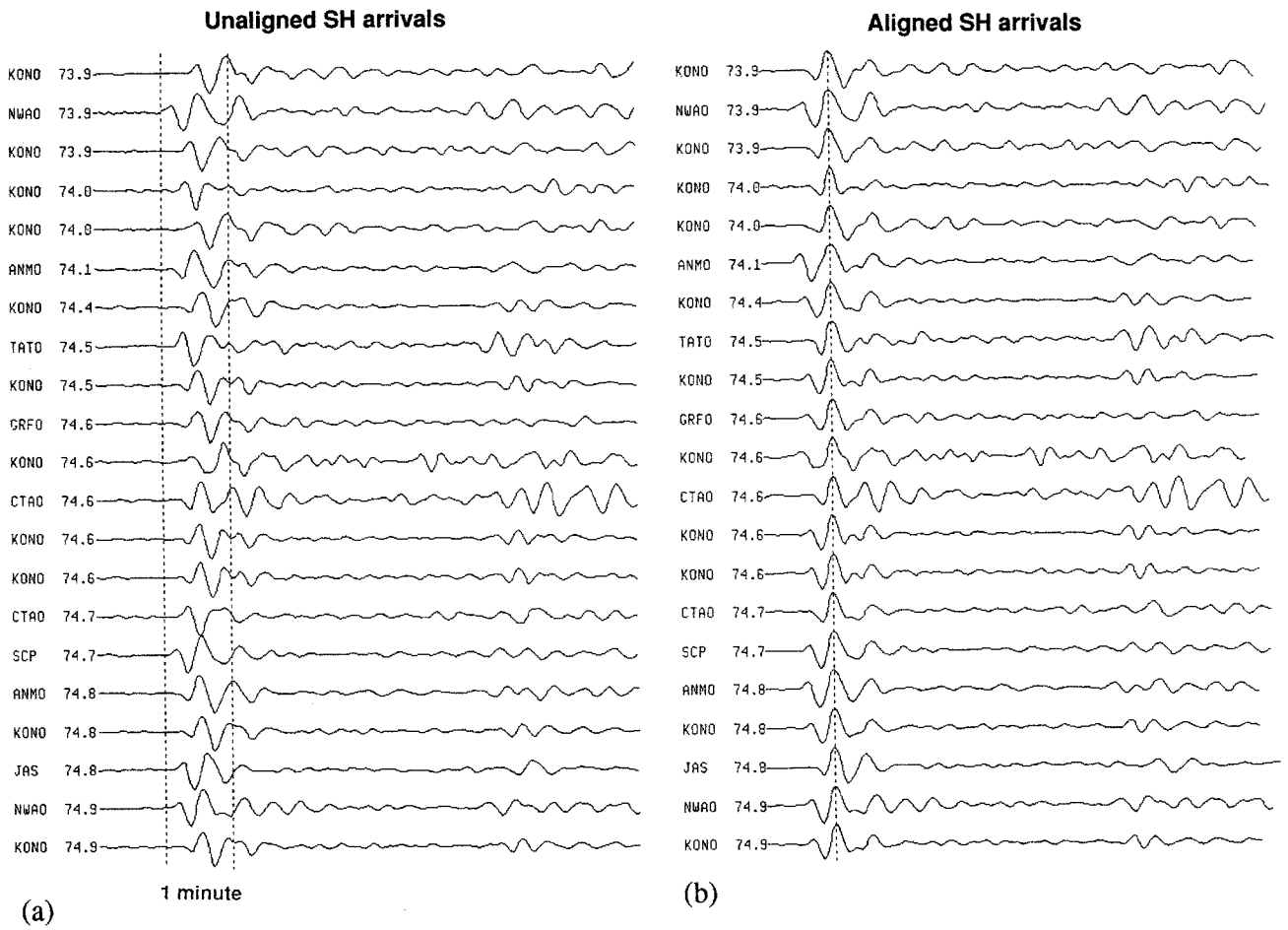

Fig. 3. An example showing the operation of the reference phase stacking procedure. (*a*) Eight minutes of long-period transverse-component seismograms at about 74° range. A 1-min time window beginning at the predicted S arrival time is indicated by the dashed lines; this window generally contains the highest amplitude in the long-period SH arrival. SS can be seen arriving about 5 min after S. All seismograms have been normalized to unit amplitude. (*b*) The result of aligning all of the seismograms on their peak SH amplitude (positive or negative), reversing the polarity if necessary. This alignment is done prior to stacking in order to increase the coherence of the stack.

SH waveforms in Figure 3*a* exhibit considerable variation between seismograms, mainly because of differences in event depths. These variations include time shifts, polarity reversals, and general pulse shape differences. A direct stack of these seismograms would not be very successful because of this waveform incoherence. The stacking procedure works by finding the largest amplitude in the 1-min window shown in Figure 3*a* and then aligning all the seismograms to this reference time (Figure 3*b*). When the resulting seismograms are stacked, the result is an effective source function which is peaked as sharply as is possible without applying any signal processing. Figure 4 shows the stacked reference phase waveforms for SH between 85° and 95° range. These pulses are typical of the waveform shapes which result from this stacking method, regardless of which reference phase is used. The central peak is bracketed by negative sidelobes about 40% to 60% of the peak amplitude and positive sidelobes about 5% to 15% of the peak amplitude. Note the similarity in these effective source functions to the GDSN impulse responses shown in Figure 2*b*.

An alternative to this stacking procedure would be to compute the cross-correlation function between each seismogram and its reference pulse and stack the cross-correlation functions [e.g., *Vinnik*, 1977; *Paulssen*, 1988]. This would have the advantage of producing relatively symmetric and peaked pulse shapes for each seismogram prior to stacking and is certainly the method of choice for broadband data in which the reference pulse shapes can be quite complicated. For the relatively narrow-band GDSN long-period data, however, the cross-correlation method would probably give very similar results to the alignment procedure used in the waveform stacks shown here (a cross-correlation technique is used later in this paper in order to identify upper mantle discontinuity phases on individual seismograms). The simplicity of the alignment technique shown in Figure 3 is appealing since it is easy to compute and produces results which are straightforward to interpret. In the future, it may be possible to improve these images by applying reflection seismology techniques such as deconvolution or phase velocity filtering.

RESULTS

Plates 1–5 show results for stacks using P, S, PP, and SS reference phases, while Figures 5 – 9 plot corresponding travel time curves calculated using the Preliminary Reference Earth Model (PREM) [*Dziewonski and Anderson*, 1981]. Major seismic phases are shown as solid lines, and upper mantle discontinuity phases are shown as dashed lines. Although PREM contains discontinuities at 400 and 670 km, the

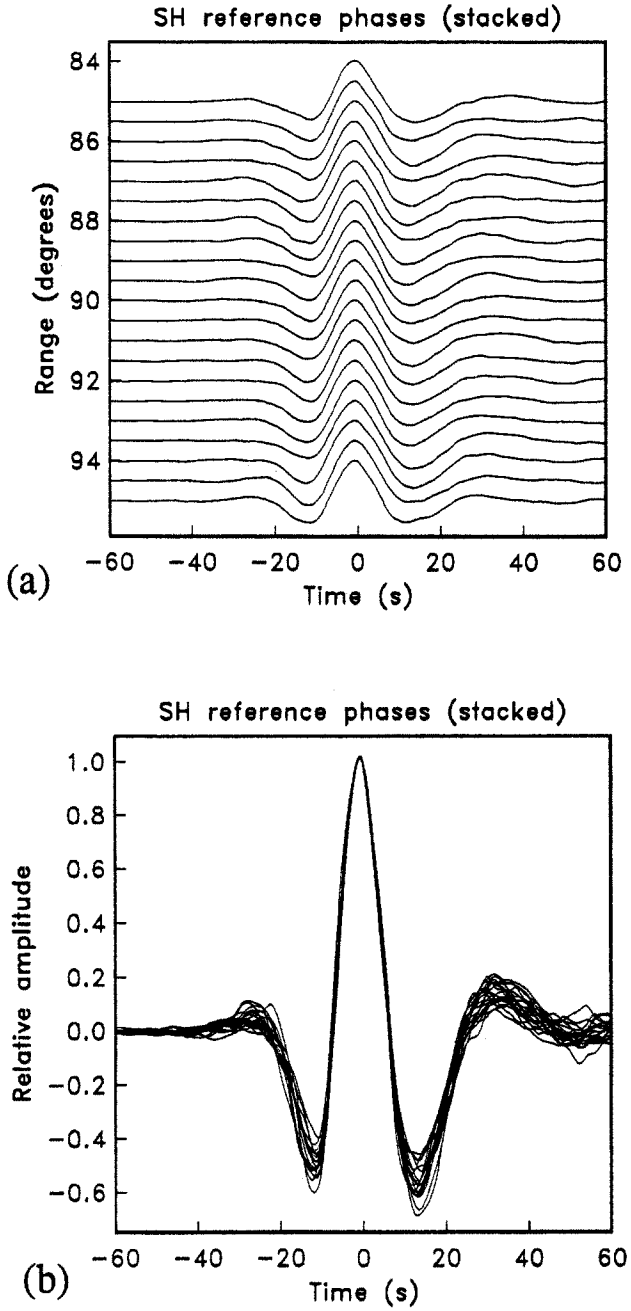

Fig. 4. Stacked reference phases from the *SH* wave stack between 85° and 95°, shown (*a*) in record section format and (*b*) overlapping. Clipped color images of these waveforms can be seen in Plate 3.

reflections and phase conversions were assumed to occur at 410 and 660 km during the ray tracing to be more consistent with the actual position of the phases (see below). Color plotting is crucial for identification of some of the more subtle features in these images, which are not apparent in standard "record section" plots.

P Wave Stack (Vertical Component)

Plate 1 shows the result of aligning the *P* wave arrival and stacking on the vertical component at ranges between 20° and 120° and travel times up to 6 min following the *P* wave arrival. The data are binned and averaged in increments of 0.5° in range and 3 s in time; 4361 seismograms are stacked for an average of about 22 seismograms per range bin. Positive amplitudes are shown in red, negative amplitudes in blue. Notice that the *P* wave arrival has been aligned at zero time, and the maximum amplitudes shown are only a tenth the size of the *P* wave amplitude. This enhances the appearance of the weaker seismic phases, at the expense of "clipping" the strong arrivals. At ranges beyond about 95° the *P* wave has been diffracted around the core-mantle boundary. P_{diff} is a weaker phase than direct *P*, reducing the number of quality records available for stacking. This causes the stack to become noticeably noisier at ranges beyond 100°, due to smaller numbers of traces at these ranges. The white vertical line at 108° is a result of no data falling within this range bin.

Figure 5 shows theoretical differential travel times calculated by tracing rays through PREM. Major phases are shown as solid lines; these include *P*, *PP*, *PPP*, *PcP*, *PKiKP*, *S*, and *ScP*. The phase of a particular seismic arrival can be identified by its color pattern. For example, the blue-red-blue pattern of the core reflected phase *PcP* indicates that it has not been phase shifted relative to the direct *P* arrival. In contrast, the red-blue-red-blue pattern of the surface-reflected phase *PP* shows the $\pi/2$ phase shift (the Hilbert transform) known to occur for this phase [*Choy and Richards*, 1975].

The dashed lines in Figure 5 show some of the upper mantle discontinuity phases discussed in this paper, and Figure 10 shows examples of ray paths for these phases. Perhaps most visible are the two phases, *P*410*sP* and *P*660*sP*, which follow *PP* and contain a single *S* leg between the 410- and 660-km discontinuities and the surface ("410" and "660" will be used in the phase names and discussion, although the actual discontinuity depths may be slightly different). These phases can be followed from 30° to 120° range. Notice that Figure 10*a* shows only one of the four possible geometries for these phases; the *S* leg could replace any of the *P* legs shown and the same travel time would result. Analogous to these phases are the arrivals which follow *PPP* (i.e. *P*410*sPP* and *P*660*sPP*) which also contain a single *S* leg between the discontinuities and the surface. These phases are visible beyond about 50°.

Weak phases can be seen following the direct *P* wave arrival by about 1.5–2.5 min at ranges between 70° and 120°. These are *P* wave multiples (*Pp*410*p* and *Pp*660*p*) which result from topside reflections off upper mantle discontinuities. Anomalous arrivals between *P* and *PP* have sometimes been explained in terms of these phases [e.g., *Nguyen-Hai*, 1963; *Husebye and Madariaga*, 1970; *Davies et al.*, 1971; *Gutowski et al.*, 1974; *Ward*, 1978]. Notice that they are phase reversed relative to the *P* wave, a result of the surface reflection. An apparent phase can be seen between the *Pp*410*p* and *Pp*660*p* arrivals in a location which corresponds to a topside reflection from a 520-km discontinuity (i.e., to *Pp*520*p*). Analogous phases appear in the *S* and *SS* stacks and will be discussed later in this paper. Also shown in Figure 5 are travel time curves for the bottomside reflected phases *P*410*P* and *P*660*P* which precede *PP* [e.g., *Nguyen-Hai*, 1963; *Ward*, 1978; *Bolt*, 1970; *Adams*, 1971]. These phases are only marginally visible in the stacked image, most clearly between 90° and 115°. Noticeably absent in Plate 1 is any indication of a multiple from a 220-km discontinuity (*Pp*220*p*) which would appear between *P* and *Pp*410*p*.

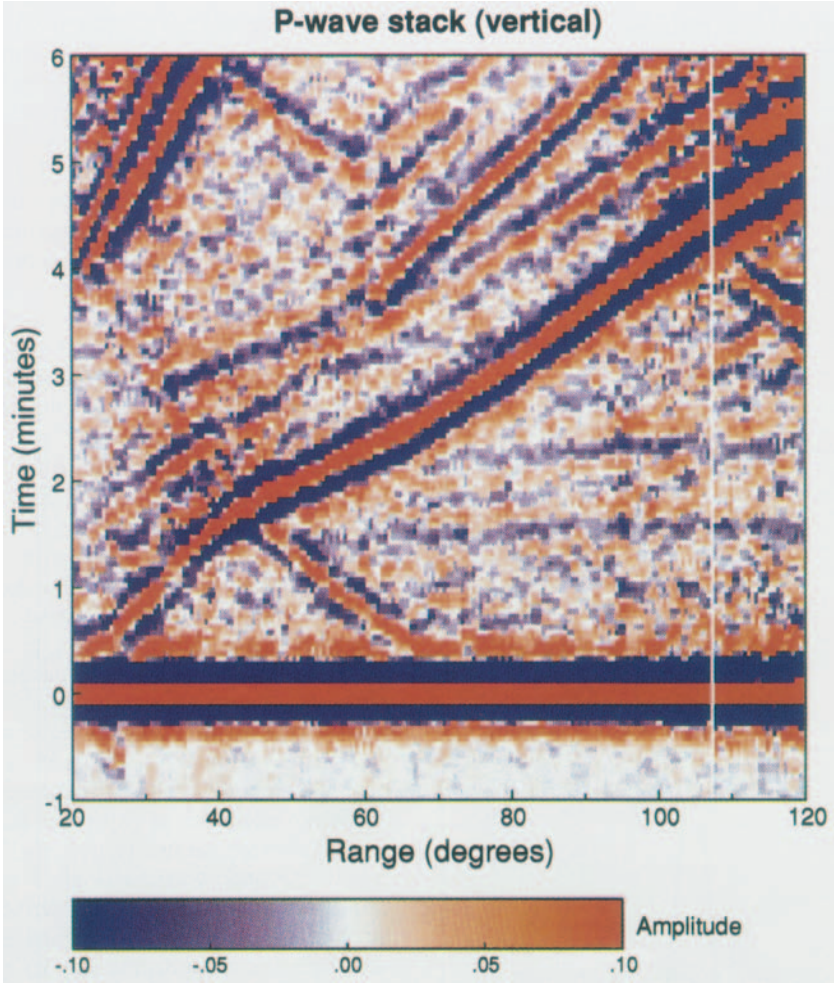

Plate 1. Stacked color image of long-period GDSN data (vertical component), aligned on P as a reference phase. Positive amplitudes are shown in red, negative amplitudes in blue, with the scale ranging up to 0.1 of the maximum P wave amplitude. The white vertical streak near 108° is a result of no data falling within this range bin.

P Wave Stack (Radial Component)

Plate 2 shows the result of stacking on the radial horizontal seismometer component after aligning the P wave arrival as in the previous example. The binning increments are the same, but results are displayed out to 12 min in order to show some of the details near the S wave arrival. The maximum amplitude shown is 0.15 of the P wave amplitude. Figure 6 shows differential travel times for the phases visible in this stack. These include P, PP, PPP, PcS, S, ScS, SKS, PS, and PPS. Notice that PcS is visible out to 90°, well beyond the ray theoretical limit for this phase. At ranges between 65° and 90°, this phase is actually PcS_{diff}, with the P wave diffracting around the core-mantle boundary.

Preceding the S arrival are two phases, $S410p$ and $S660p$, which result from SV-to-P conversions at the 410- and 660-km discontinuities beneath the station (see Figure 10). Also visible in Plate 2 are the analogous SKS precursors, $SKS410p$ and $SKS660p$. These phases have previously been observed in long-period data by *Faber and Müller* [1980, 1984], *Baumgardt and Alexander* [1984], and *Bock* [1988]. These arrivals may also contain energy from P-to-SV conversions at discontinuities below the events (i.e. $p410S$ and $p660S$); these arrive at the same time as the SV-to-P converted phases, and both sets of arrivals are seen most clearly on the radial component [*Faber and Müller*, 1984]. Notice that $S410p$ and $S660p$ can be seen at ranges as small as 60° and 80°, respectively, much closer than the ray theoretical limits shown in Figure 6, but in agreement with the results of synthetic seismogram modeling [*Faber and Müller*, 1980].

Two phases which follow direct P by about 40 to 90 s can be seen as blue streaks in Plate 2, $P410s$ and $P660s$. These result from P-to-SV conversions at discontinuities below the recording stations [e.g., *Vinnik*, 1977; *Paulssen*, 1985, 1988; *Kind and Vinnik*, 1988]. The time separation between these phases is too short to permit a 520-km discontinuity to be seen, since the dominant period of the pulses is about 25 s. The blue streak visible between P and $P410s$ is a sidelobe artifact of direct P, because it remains parallel to P even at short ranges, whereas a converted phase from a discontinuity shallower than 410 km would become increasingly delayed at close ranges. Also visible in Plate 2 are hints of topside P multiples, some of which can be seen more clearly in the vertical-component stack (Plate 1). Travel times for these phases are shown as dotted lines in Figure 6. Notice that the phase $Pp410s$ arrives at almost the same time as $Pp660p$.

It is interesting to note that while P-to-SV near-receiver conversions following P can easily be seen on the radial-component stack (Plate 2), the corresponding SV-to-P near-source converted phases (e.g., $s410P$ and $s660P$) cannot

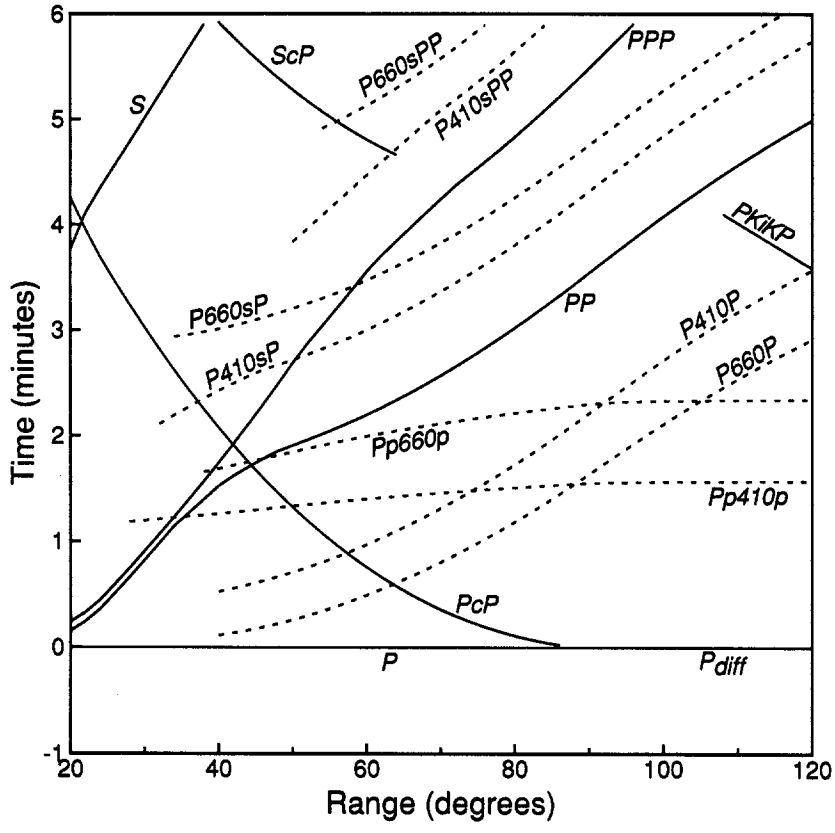

Fig. 5. Travel time curves relative to P for primary seismic phases (solid) and upper mantle discontinuity phases (dashed) for comparison with the stacked image shown in Plate 1. Curves were calculated using PREM, with interfaces assumed at 410-km and 660-km depth.

be seen in the vertical-component stack (Plate 1). SV-to-P conversions have been observed in the P coda for selected deep subduction zone events [e.g., *Barley et al.*, 1982; *Bock and Ha*, 1984; *Richards and Wicks*, 1990]. The absence of these phases in the vertical component stack could be a result of at least three factors. First, the noise levels in the P coda may be higher on the vertical component compared to the radial component. Second, the stacking procedure adjusts the polarities of the P wave reference phase prior to stacking. However, in the case of $s410P$ and $s660P$, the rays begin as SV waves leaving the source. The radiation patterns of SV and P are sufficiently different that the polarity of SV will vary even for identical P polarities. Thus the P wave stacking procedure is only optimal for waves which leave the source as P waves and may cause incoherent stacking for phases which leave the source as SV waves. However, this effect does not prevent clear images of direct SV from appearing in the vertical- and radial-component stacks. Third, source depth variations will cause time shifts and some incoherent stacking in SV-to-P converted phases if direct P is used as a reference phase.

S Wave Stack (Transverse Component)

Plate 3 shows the result of aligning the SH wave and stacking on the transverse horizontal component at ranges between 40° and 120° and travel times up to 7 min following the SH wave arrival. The data are binned and averaged in increments of 0.5° in range and 2 s in time; 3753 seismograms are stacked for an average of about 23 seismograms per range bin. The maximum amplitude shown is 0.1 of the S wave amplitude. As in the P wave stacks, the image becomes noisier at ranges beyond about 100°, due to the relatively small number of quality S_{diff} arrivals at these ranges. Figure 7 shows travel times for seismic phases visible in the transverse component stack. The S, SS, SSS, and ScS phases are visible. Notice that as expected [*Choy and Richards*, 1975], the SS phase is Hilbert transformed relative to S.

Also clearly apparent in this stack are the SH wave multiples resulting from topside reflections off the 410- and 660-km discontinuities ($Ss410s$ and $Ss660s$, see Figure 10). These are phase reversed relative to S and are visible between about 70° and 115°. As in the case of the P wave multiples, a phase also appears between these reflections which is apparently caused by a discontinuity at about 520 km. This feature is better resolved in the SH stack because of the relatively large time separation between the $Ss410s$ and $Ss660s$ arrivals. I will discuss the implications of this phase and the possibility that it is an artifact of the sidelobes of the 410- and 660-km discontinuity phases later in this paper. Figure 7 also shows travel times for the bottomside reflected phases, $S410S$ and $S660S$, which precede SS. These phases, like SS, are Hilbert transformed relative to S and are faintly

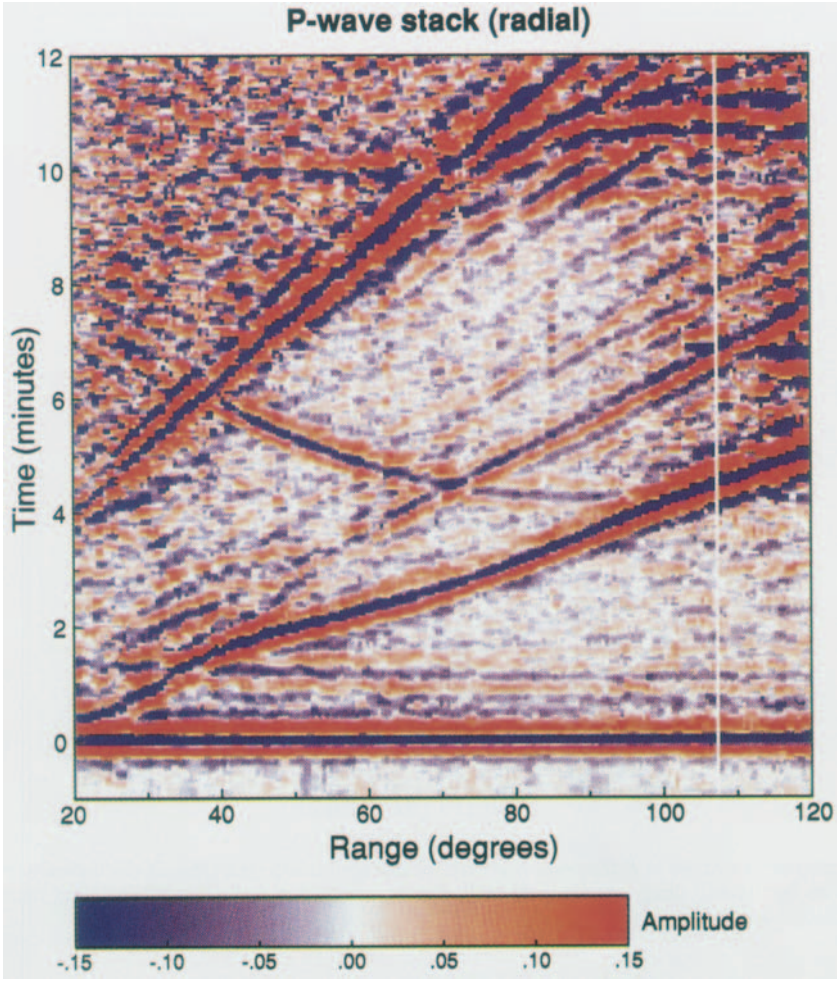

Plate 2. Stacked color image of long-period GDSN data (radial component), aligned on P as a reference phase. Positive amplitudes are shown in red, negative amplitudes in blue, with the scale ranging up to 0.15 of the maximum P wave amplitude. The white vertical streak near 108° is a result of no data falling within this range bin.

visible in the stacked image, with $S660S$ particularly apparent between 75° and 95°. These precursors to SS can be seen much more clearly on the SS wave stack (see below). A hint of the topside ScS multiple off the 660-km discontinuity ($ScSs660s$) can be seen near 65° range. As in the case of the P wave stack, there is no visible phase corresponding to a multiple off a 220-km discontinuity.

SS Wave Stack (Transverse Component)

Plate 4 shows the result of aligning the SS wave and stacking on the transverse horizontal component at ranges between 80° and 180° and travel times up to 10 min before and 5 min after the SS wave arrival. The data are binned and averaged in increments of 0.5° in range and 3 s in time; 3302 seismograms are stacked for an average of about 17 seismograms per range bin. The maximum amplitude shown is 0.05 of the SS wave amplitude. The image becomes very sparse and noisy between 170° and 180°, reflecting the lack of data near the antipode. Figure 8 shows travel time curves for phases visible in this stack, including S, SS, SSS, and $ScSScS$. Notice that S amplitudes are diminished beyond 100°, due to the decay of S_{diff} in the core shadow zone, and that S is Hilbert transformed relative to SS.

The prominent blue streaks which precede SS by 2–4 min are bottomside reflections from upper mantle discontinuities ($S410S$ and $S660S$, see Figure 10). They can be seen between about 110° and 180° and are not phase reversed relative to SS. As in the case of the P and SH multiples, an additional streak appears between these phases which is apparently caused by a discontinuity at 520 km. Also visible in this stacked image are the topside S multiples, $Ss410s$ and $Ss660s$, which, like direct S, are Hilbert transformed relative to SS. These phases are seen much more clearly in the S wave stack (Plate 3). Suggestions of additional upper mantle discontinuity phases are visible between SS and SSS. These include the topside multiples of SS ($SSs410s$ and $SSs660s$) and the bottomside reflected precursors to SSS ($SS410S$ and $SS660S$). Hints of $ScS410ScS$ and $ScS660ScS$, the bottomside precursors to $ScSScS$, are marginally apparent between $S410S$ and SS. As in the case of the P and S wave stacks, there is no visible phase corresponding to a reflection off a 220-km discontinuity.

PP Wave Stack (Vertical Component)

Plate 5 shows the result of aligning the PP wave and stacking on the vertical component at ranges between 80°

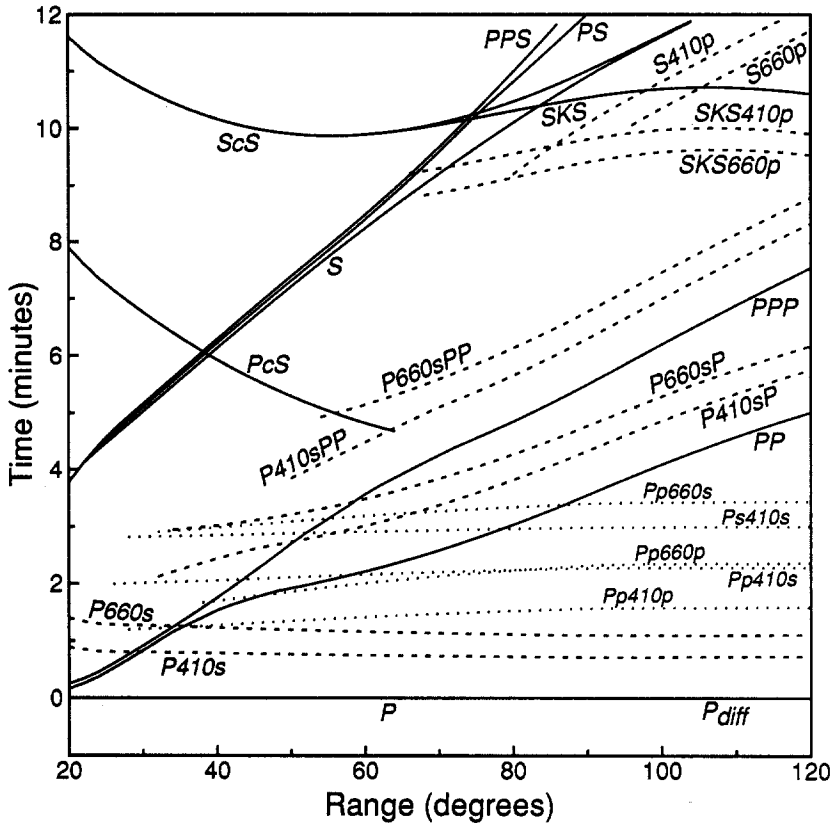

Fig. 6. Travel time curves relative to P for primary seismic phases (solid) and upper mantle discontinuity phases (dashed) for comparison with the stacked image shown in Plate 2. Curves were calculated using PREM, with interfaces assumed at 410-km and 660-km depth.

and 180° and travel times up to 7 min before and 5 min after the PP wave arrival. The data are binned and averaged in increments of 0.5° in range and 3 s in time; 2485 seismograms are stacked for an average of about 12 seismograms per range bin. The maximum amplitude shown is 0.1 of the PP wave amplitude. The image becomes very sparse and noisy between 170° and 180°, due to the lack of data near the antipode. Figure 9 shows travel time curves for phases visible in this stack, including P, PKP, PP, PKS, and PPP. P wave amplitudes are diminished beyond 100°, reflecting the decay of P_{diff} in the core shadow zone. The various branches of PKP (e.g., AB, BC, and DF) are labeled on Figure 9, although $PKP(BC)$ is not well separated from the other branches for these long-period data. Notice that $PKP(AB)$ extends to almost 200°, well beyond the ray theoretical limit of about 170° (shown as the point A in Figure 9). This $PKP(AB)_{diff}$ phase can also be seen in automatic gain control stacks of GDSN long-period data [*Shearer*, 1991].

Various upper mantle discontinuity phases are seen in this image. The bottomside reflection off the 410-km discontinuity ($P410P$) is visible between about 105° and 145°, although the corresponding 660-km phase ($P660P$) is not apparent. The absence of $P660P$ is probably due to interference with other phases such as PKP and the topside P multiple $Pp660p$, although it is puzzling that at least a portion of $P660P$ cannot be seen near 120°. The topside multiples of PKP ($PKPp410p$ and $PKPp660p$) are seen following PKP between about 145° and 175°. They are particularly bright following $PKP(BC)$ due to the larger amplitude of this phase. Since both the BC and DF branches of PKP are Hilbert transformed relative to PP, the corresponding multiples are also Hilbert transformed, making it difficult to pick out individual arrivals in this region. Additional upper mantle discontinuity phases can be seen following PP and PPP, including $P410sP$, $P660sP$, $P410sPP$, and $P660sPP$ (see Figure 10 for the ray geometry of these phases).

Discussion

The stacked images shown in Plates 1–5 have many advantages in studying long-period seismic data. At a glance they indicate the relative times, polarities, and amplitudes of both major and minor phases. They reveal patterns that would be difficult to see on individual seismograms. Many of the weaker phases appear on individual long-period seismograms as a single low-amplitude bump. One can only have confidence in the existence of these phases when they are observed on dozens of seismograms to form a consistent arrival. To my knowledge, the phases PcS_{diff}, PKP_{diff}, and many of the upper mantle discontinuity phases seen in these images have not previously been recognized. Although many aspects of these images are interesting, the focus of this paper is on the upper mantle discontinuity phases. Four of these phase geometries are particularly well resolved and isolated from other arrivals (the P-to-SV conversions, the P and S multiples, and the SS precursors) and will be analyzed in more detail.

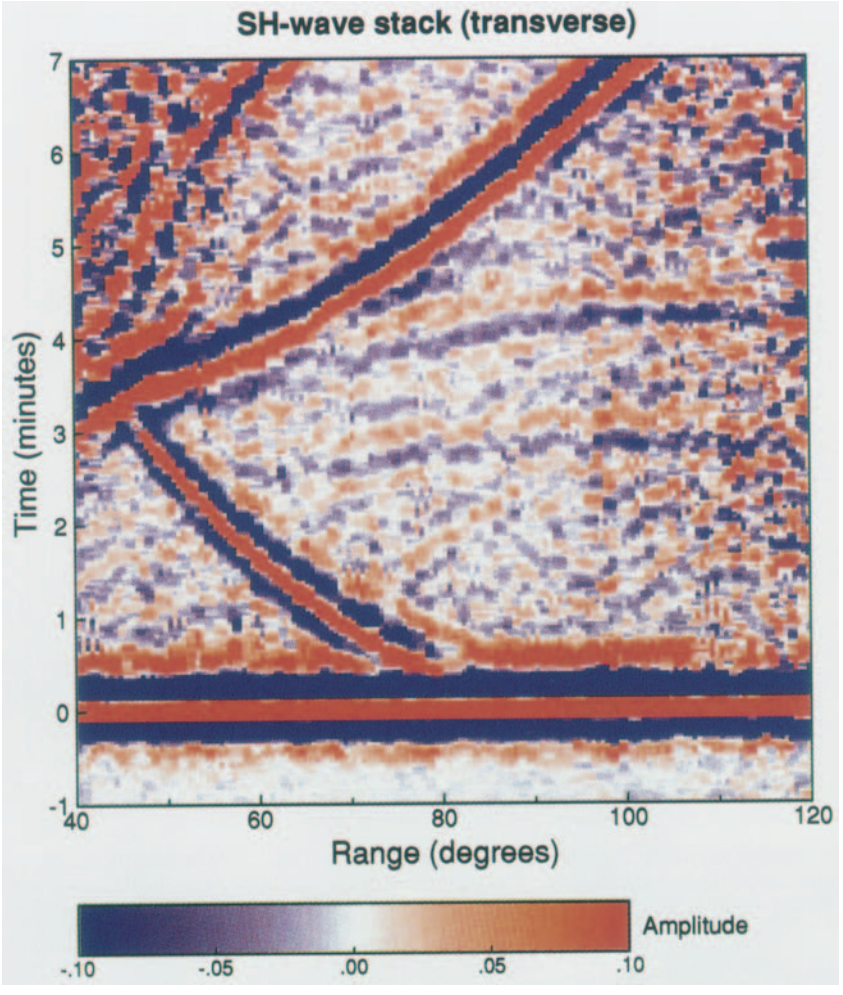

Plate 3. Stacked color image of long-period GDSN data (transverse component), aligned on S as a reference phase. Positive amplitudes are shown in red, negative amplitudes in blue, with the scale ranging up to 0.1 of the maximum S wave amplitude.

The precursors to S and SKS (e.g., $S410p$, etc.) can be seen in the radial component P wave stack (Plate 2), but not very clearly. Stacks using P as a reference arrival are not ideal for observing these phases since they travel through the mantle as S waves and arrive much later than P. In principle, better results could be obtained for the S precursors if S were used as a reference phase. However, attempts to stack by aligning SV proved to be difficult, since SV waveforms are complicated due to the effects of surface reflections and $P - SV$ crustal arrivals such as shear-coupled PL [e.g., *Oliver*, 1961; *Frazer*, 1977; *Baag and Langston*, 1985].

Observations of transverse energy arriving from P-to-SV converted arrivals have been used to constrain shear wave splitting and upper mantle anisotropy [*Vinnik et al.*, 1984, 1989; *Kosarev et al.*, 1984; *Kind et al.*, 1985]. Although difficult to see in long-period data, conceivably these arrivals might be imaged by examining the transverse component from a P wave stack. However, this analysis is complicated by the fact that SH wave polarities are uncorrelated to P or SV wave polarities. Thus transverse wave energy will generally not stack coherently unless an SH-polarized wave is used as a reference phase. This difficulty is avoided if the absolute value is taken of the transverse-component amplitudes prior to stacking (at the cost of sacrificing polarity information). Transverse-component stacks obtained in this way using a P wave reference phase do not show anomalous arrivals near the time of the SV-polarized $P410s$ and $P660s$ phases. This is most likely due to the intrinsic difficulty in resolving short shear wave splitting delay times (e.g., <1–2 s) with long-period data, rather than to any lack of anisotropy in the upper mantle.

CROSS-CORRELATION ANALYSIS

As an alternative to the stacking procedure discussed above, a cross-correlation method can be used to resolve upper mantle discontinuity phases. This has the advantage of permitting the computation of discontinuity depths for each seismogram individually to see if these results are consistent with the stacked images. The cross-correlation analysis proceeds as follows:

1. The same seismograms are used as in the stacking method, i.e., those from events shallower than 50 km with acceptable signal-to-noise ratios.

2. For each reference phase, a 41-s wavelet centered on the maximum amplitude point is used to extract a reference waveform, and the cross-correlation function between this wavelet and the rest of the seismogram is computed.

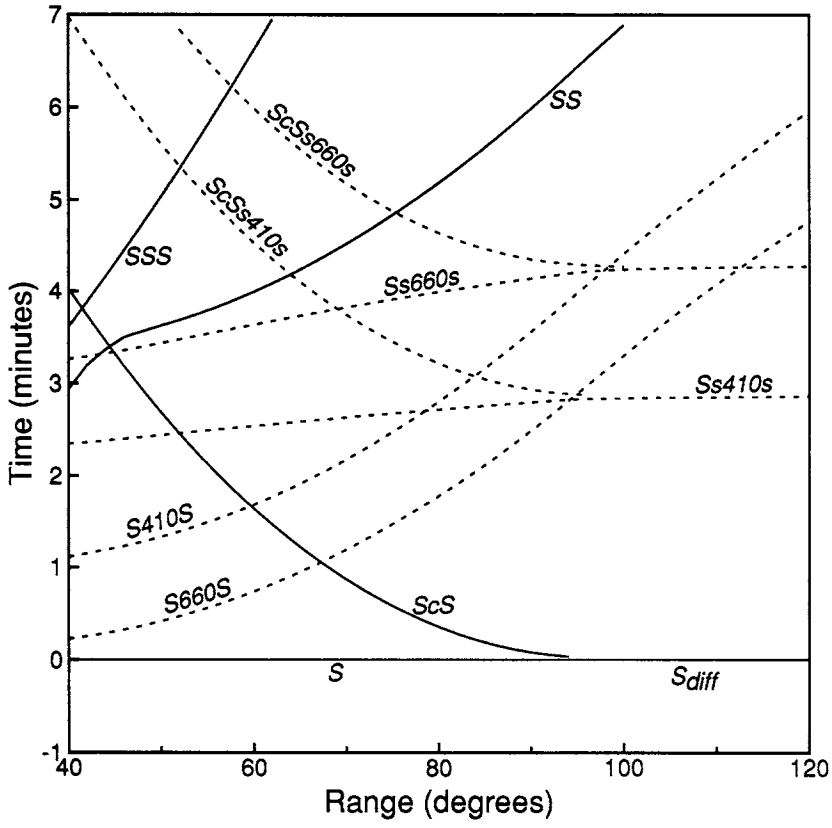

Fig. 7. Travel time curves relative to S for primary seismic phases (solid) and upper mantle discontinuity phases (dashed) for comparison with the stacked image shown in Plate 3. Curves were calculated using PREM, with interfaces assumed at 410-km and 660-km depth.

3. Peaks and troughs in the cross-correlation function are identified and saved. This procedure finds the time shifts to pulses in the seismogram which are similar in shape to the reference arrival and thus may represent other phases.

4. Assuming a particular discontinuity phase of interest and an upper mantle velocity model, these points may be converted directly into apparent discontinuity depths.

Figure 11*a* shows the results of this procedure applied to the 3753 seismograms in the SH wave stack. In order to resolve the SH multiples from upper mantle discontinuities, points are plotted only if the correlation coefficient r between the reference wavelet and the seismogram is less than -0.7 (the correlation coefficient is negative since these arrivals are phase reversed relative to S). Both $Ss410s$ and $Ss660s$ are visible in this plot, as well as the apparent $Ss520s$ multiple seen in the stacked image. Using an upper mantle velocity model, discontinuity depths can be calculated for each point in this plot. This is illustrated in Figure 11*b*, which now plots the points directly versus apparent discontinuity depth assuming PREM as a reference earth model. Notice that the slight curvature in the travel times for $Ss410s$ and $Ss660s$ shown in Figure 11*a* is removed in Figure 11*b* since the calculation takes into account the theoretical travel time curves for these phases.

The choices of a 41-s window for the reference wavelet and a threshold for the correlation coefficient of 0.7 are somewhat arbitrary, but the results which follow are relatively insensitive to variations in these parameters. Plots similar to Figure 11 can be obtained using an 11-s reference phase window and a correlation coefficient threshold of 0.9. The data are sufficiently band-limited that computed cross-correlation functions do not differ greatly from the original seismograms. Thus it is likely that comparable results could be obtained by counting the peaks and troughs in the raw waveforms, without computing any cross-correlation functions.

Figure 12*a* shows the apparent discontinuity depths predicted by cross-correlation analysis, using four different types of discontinuity phases and assuming PREM for the upper mantle velocities. These phases include P-to-SV conversions recorded on the radial component between ranges of 40° and 105°, P wave and S wave multiples between 70° and 110° recorded on the vertical and transverse components, respectively, and SS precursors recorded on the transverse component between 110° and 180°. The vertical-component P wave is used as the reference wavelet for both the P multiples and the P-to-SV converted phases, SH is used as a reference for the S multiples, and SS is used for the SS precursors. Points are plotted only for $r > 0.7$ (or $r < -0.7$ for phase reversed arrivals) and are binned in 2-km depth increments. The plots have been smoothed by convolution with a $\cos^2$ function of 30-km half width, with the y axis showing the number of points within a 10-km depth interval. Peaks are seen near 410, 520, and 660 km for all four of these phases, except no 520-km peak is present for the P-to-SV converted phases. The lack of a 520-km peak in this case is to be expected, given the small time separation between the 410- and 660-km phases in the long-period P-to-SV conversions.

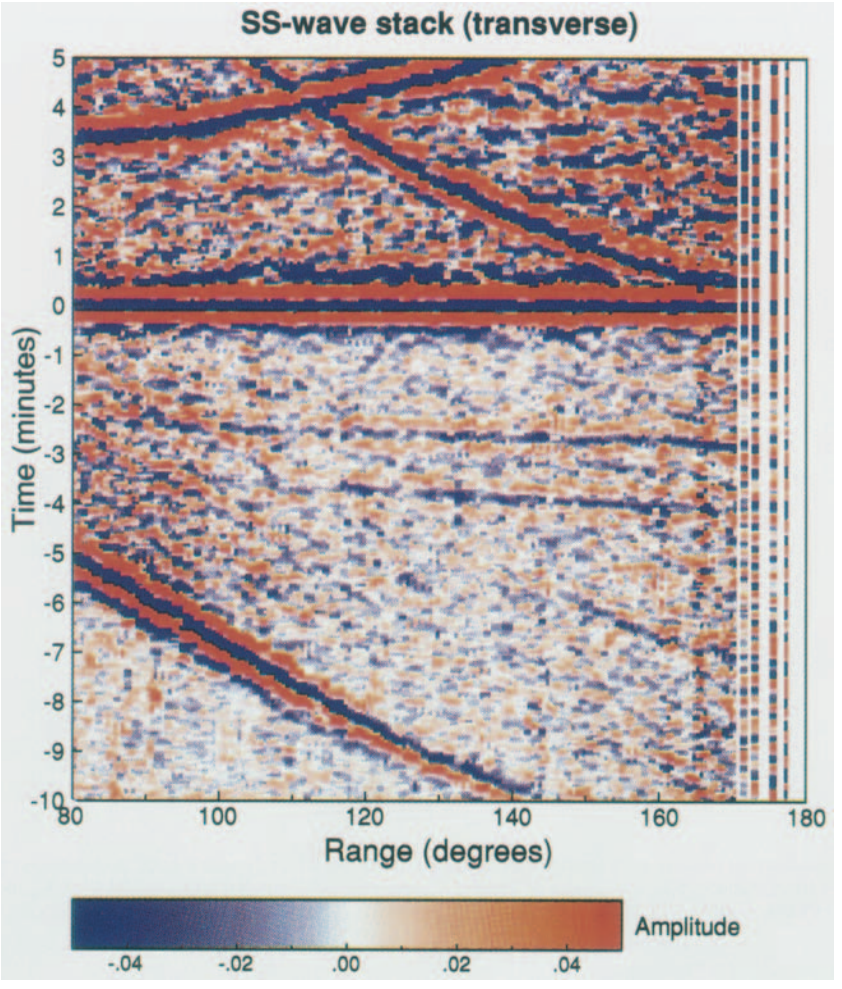

Plate 4. Stacked color image of long-period GDSN data (transverse component), aligned on SS as a reference phase. Positive amplitudes are shown in red, negative amplitudes in blue, with the scale ranging up to 0.05 of the maximum SS wave amplitude.

One might argue that the 520-km peak in Figure 12*a* is not especially significant since comparable levels are seen at depths below about 350 km, so that this peak may simply be an artifact of the negative sidelobes of the 410- and 660-km phases. However, this interpretation does not explain why the 520-km peak should be closer to the 410-km peak than to the 660-km peak. In addition, the number of cross-correlation peaks identified seems to diminish with discontinuity depth: there are significantly higher levels above 410 km than below 660 km, perhaps reflecting increased lateral heterogeneity and scattering in the uppermost mantle. While the 520-km peak is a stable feature between the different discontinuity phases, there are no prominent peaks above 410 km which are consistent from plot to plot. This is illustrated in Figure 12*b*, which plots the difference between the number of positive and negative peaks in the cross-correlation function. In this case the levels are greatly reduced at shallow depths, and the 520-km peak is now higher than any feature except the 410- and 660-km peaks. This reflects the lack of a coherent arrival from a discontinuity shallower than 410 km. For each of the four phases considered, the 660-km peak is slightly broader than the 410-km peak. This is not likely to be caused by differences in signal-to-noise levels since 660-km discontinuity phases generally have comparable or higher amplitudes than the corresponding 410-km phases. The broader 660-km peaks are consistent with greater variability in apparent depths, suggesting either larger depth variations for the 660-km interface or significant lateral heterogeneity in the transition zone.

Average apparent depths to the 410-, 520- and 660-km discontinuities (d_{410}, d_{520}, and d_{660}) are listed in Table 1. These are computed by identifying the 60-km-wide window around each peak for which the mean discontinuity depth is equal to the midpoint of the window. Standard errors for the uncertainty in these estimates (e_{410}, e_{520}, and e_{660}) are obtained by randomly resampling the data using a bootstrap method [e.g., *Efron and Tibshirani*, 1986]. The isotropic version of PREM was used as a reference Earth model but with the oceans filled in (α = 5.8 km/s, β = 3.2 km/s) to allow the computation of results for surface shear wave sources. Since the actual discontinuities in PREM are at 400 and 670 km, some inconsistency is introduced by using this model to compute depths to discontinuities near 410 and 660 km. However, the errors introduced are small since the integrated travel time is relatively insensitive to minor variations in the depth of the discontinuities. For consistency, PREM is used to compute all the travel times in this paper, and it should be understood that the resulting

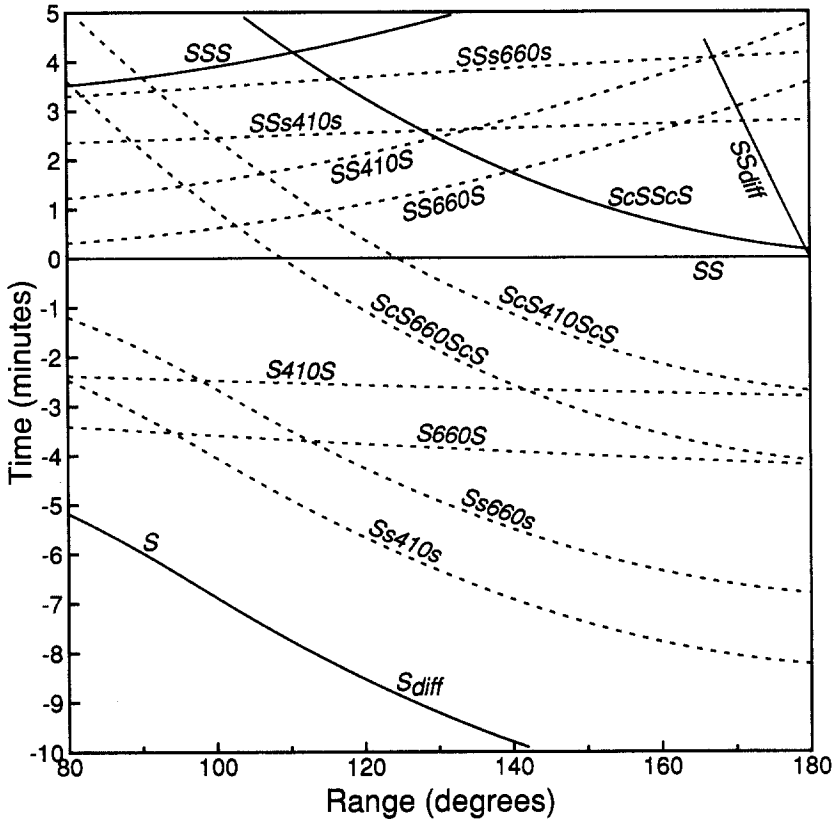

Fig. 8. Travel time curves relative to SS for primary seismic phases (solid) and upper mantle discontinuity phases (dashed) for comparison with the stacked image shown in Plate 4. Curves were calculated using PREM, with interfaces assumed at 410-km and 660-km depth.

apparent discontinuity depths are relative to the PREM model. Corresponding vertical travel times (t_{410}, t_{520}, and t_{660}) for these apparent depths are also listed in Table 1. These times represent the one-way vertical S wave travel time for the SH multiples and SS precursors, the one-way P wave travel time for the P multiples, and the one-way $S - P$ travel time for the P-to-SV conversions.

These apparent discontinuity depths depend upon the velocity in the upper mantle above the discontinuities: slower velocities would result in greater apparent discontinuity depths even if the true discontinuity depths were constant. Thus lateral heterogeneity in the upper mantle will introduce errors into the computed discontinuity depths. In an attempt to compensate for the effects of upper mantle heterogeneity, I applied corrections to these data based on the long-period $SS - S$ residuals measured by *Woodward and Masters* [1991]. Since SS and S have similar paths near the source and receiver, these data provide a direct measure of two-way shear wave travel time differences due to propagation through the upper mantle near the SS bounce point (although midmantle heterogeneity may cause some contamination by introducing travel time differences along the S leg [see *Masters and Bolton*, 1990]). Thus these data are ideal for correcting the S multiples and SS precursor phases for the effects of upper mantle heterogeneity and, with proper scaling, can also be used to correct the P multiples and P-to-SV converted phases. These corrections are most appropriate for the 660-km discontinuity phases since they compensate for the integrated travel time differences due to heterogeneity between the surface and 660 km. Corrections can also be applied to the 410-km phases, but these will be less accurate to the extent that transition zone heterogeneity is important (i.e., heterogeneity between 410 and 660 km).

Times for discontinuity phases were adjusted using a smoothed global model of the raw $SS - S$ residual data set (R.L. Woodward, personal communication, 1990), hereafter referred to as WM.SS-S, and apparent discontinuity depths recalculated. These corrected mean depths are listed in Table 1 as d'_{410}, d'_{520}, and d'_{660} with associated standard errors e'_{410}, e'_{520}, and e'_{660}. The WM.SS-S value at the SS bounce point was used to correct the SS precursor data, while the average of the source and receiver $SS - S$ residuals was used to correct the S multiple data. For the P multiples, the WM.SS-S model was reduced by a factor of 2 (see *Woodward and Masters* [1991] for a discussion of the scaling between $SS - S$ and $PP - P$ residuals) and the average of the source and receiver values applied as a correction. For the P-to-SV converted arrivals, the WM.SS-S model was reduced by a factor of 4, and a correction applied for the WM.SS-S value at the receiver. The residuals in WM.SS-S were computed relative to PREM (with the oceans filled in, see above), adjusted for ellipticity but uncorrected for topography and bathymetry variations. Since the effects of these variations are thus included in the WM.SS-S model, corrections applied using this model adjust for the effects of topography/bathymetry differences as well as velocity variations. The pattern of velocity anomalies in the WM.SS-S model is roughly similar to other upper mantle models such as M84C [*Woodhouse and Dziewonski*, 1984] and MDLSH [*Tanimoto*, 1990]. However, Woodward and Masters found

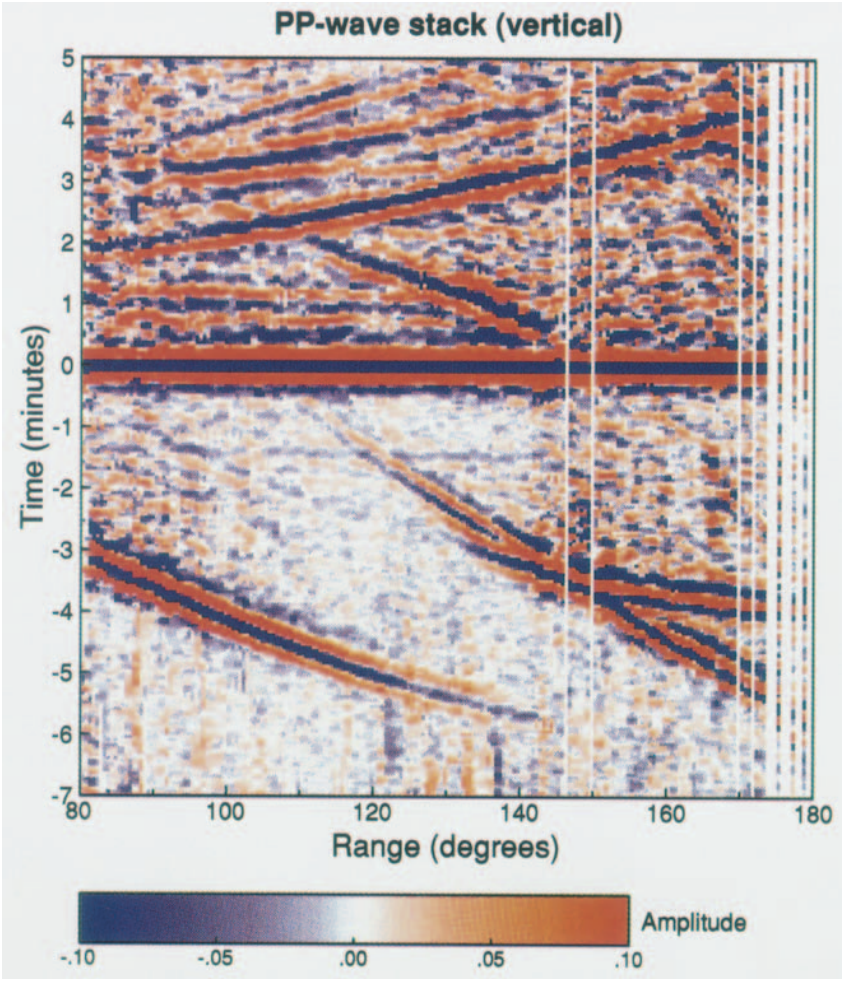

Plate 5. Stacked color image of long-period GDSN data (vertical component), aligned on PP as a reference phase. Positive amplitudes are shown in red, negative amplitudes in blue, with the scale ranging up to 0.1 of the maximum PP wave amplitude.

that M84C underpredicted the observed $SS - S$ residuals by about a factor of two, while MDLSH overpredicted the residuals by 50%.

Apparent depths to the 410-km discontinuity shown in Table 1 range from 409 to 415 km for the uncorrected discontinuity phases and from 414 to 419 km for the WM.SS-S adjusted depths. A global average of the WM.SS-S residuals is slightly negative, reflecting the fact that most SS bounce points are at the seafloor rather than at the Earth's surface as assumed in calculating the reference travel times. Correcting for these negative residuals has the effect of moving the apparent discontinuity depths to somewhat deeper values. Apparent depths to the 520-km discontinuity range from 514 to 521 km for the uncorrected discontinuity phases and from 519 to 526 km for the WM.SS-S adjusted depths. Apparent depths to the 660-km discontinuity range from 650 to 666 km for the uncorrected discontinuity phases and from 653 to 669 km for the WM.SS-S adjusted depths. The 16-km spread in the mean apparent depths to the 660-km discontinuity is puzzling, given the relatively close agreement in the apparent depths to the 410- and 520-km discontinuities between the different phases. Depths to the 660-km discontinuity based on the S multiple and SS precursor phases agree rather well, suggesting that the problem may be an incorrect P-to-S velocity ratio in the transition zone. However adjusting this ratio cannot simultaneous explain the increased apparent depths to the 660 from the P multiples (sensitive to the P travel time) and the even larger apparent depths to the 660 from the P-to-SV conversions (sensitive to the $S - P$ travel time). It is unlikely that increasing the amount of data would remove this discrepancy since it is well outside the standard errors on the estimates obtained using the bootstrap method. While the P multiples and S multiples are sensitive to both the source and receiver structures, the P-to-SV conversions sample only near the receiver. Thus it is conceivable that the greater apparent depth to the 660-km discontinuity for the P-to-SV conversions reflects lateral depth variations in the 660-km discontinuity with generally greater depths beneath the continents where the majority of seismic stations are located or that a few anomalous stations are overrepresented in the data set.

RESULTS FOR INDIVIDUAL STATIONS

Since the P-to-SV converted phases are sensitive only to the discontinuity depths near the receivers, it is possible to examine results for individual seismic stations. Figure 13 shows the number of cross-correlation peaks obtained as a function of apparent discontinuity depth for 37 stations. This plot is analogous to Figure 11*a*, but each individual trace has been scaled to the same total size. The number to the right of

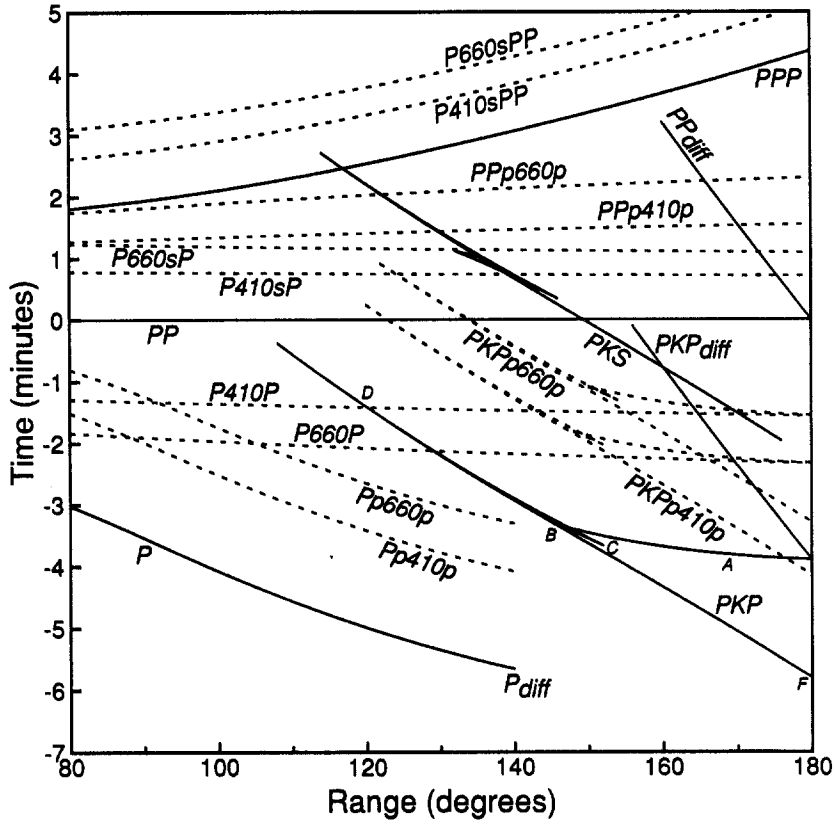

Fig. 9. Travel time curves relative to PP for primary seismic phases (solid) and upper mantle discontinuity phases (dashed) for comparison with the stacked image shown in Plate 5. Curves were calculated using PREM, with interfaces assumed at 410-km and 660-km depth. The various branches of PKP are indicated by letters.

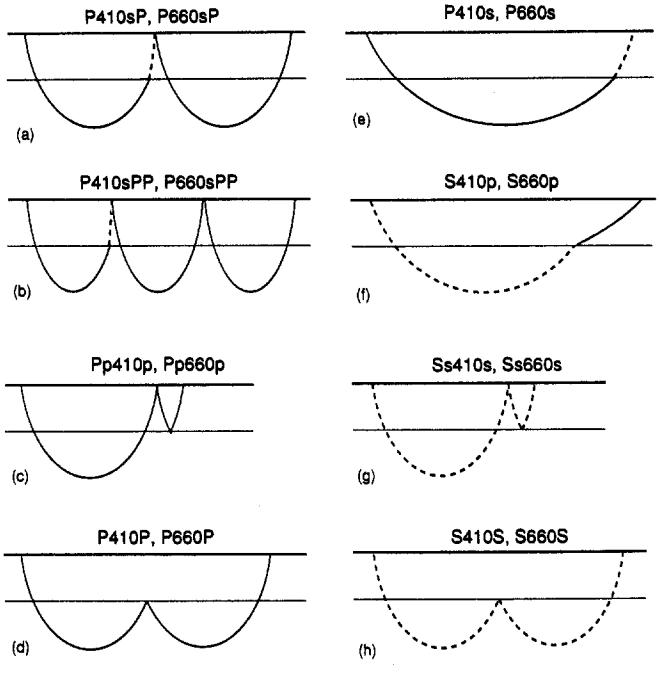

Fig. 10. Some of the upper mantle discontinuity phases visible in Plates 1–5. P waves are shown as solid lines, and S waves are shown as dashed lines, with the thin horizontal line representing either the 410-, the 520-, or the 660-km discontinuity. Lowercase p and s represent short ray segments between the discontinuities and the surface. Phases (*a*)–(*d*) can be seen most clearly on the vertical-component stacks (Plates 1 and 5), (*e*) and (*f*) most clearly on the radial-component stack (Plate 2), and (*g*) and (*h*) on the transverse-component stacks (Plates 3 and 4).

each station name indicates the number of cross-correlation peaks within 50 km of 660 km. The quantity of data varies between stations; some stations such as NWAO, KONO, and GRFO are well sampled, while others such as LEM and AFI are represented by only a small number of data points. For most of the stations, peaks near 410 and 660 km can be identified, with generally cleaner results obtained for the stations with the most data. Some of the stations exhibit peaks at other depths or multiple peaks, but there is little consistent pattern to these features. It is unclear if these complications represent additional discontinuities or scattering due to lateral heterogeneity or are a result of inadequate sampling of intrinsically noisy data. Some, if not all, of the peaks between 200 and 250 km probably represent sidelobe artifacts of direct P (see Plate 2).

The technique used in generating Figure 13, identifying P-to-SV converted phases by cross correlating the P wave on the vertical component with the radial component, has many similarities to the receiver function method [e.g, *Burdick and Langston*, 1977; *Owens et al.*, 1984, 1987; *Ammon et al.*, 1990]. Receiver function analysis has generally been used to obtain crustal structure but has recently also been successful in identifying upper mantle discontinuities [*Gurolla and Minster*, 1990]. It is interesting to note how relatively easily upper mantle discontinuities can be seen in long-period data (i.e., often from only a few seismograms), compared to the difficulty in seeing these phases in broadband or high-frequency data [e.g., *Paulssen*, 1988]. This does not necessarily imply a lack of sharpness in the discontinuities, since noise levels are much greater at high frequencies due to increasing scattering from upper mantle heterogeneity.

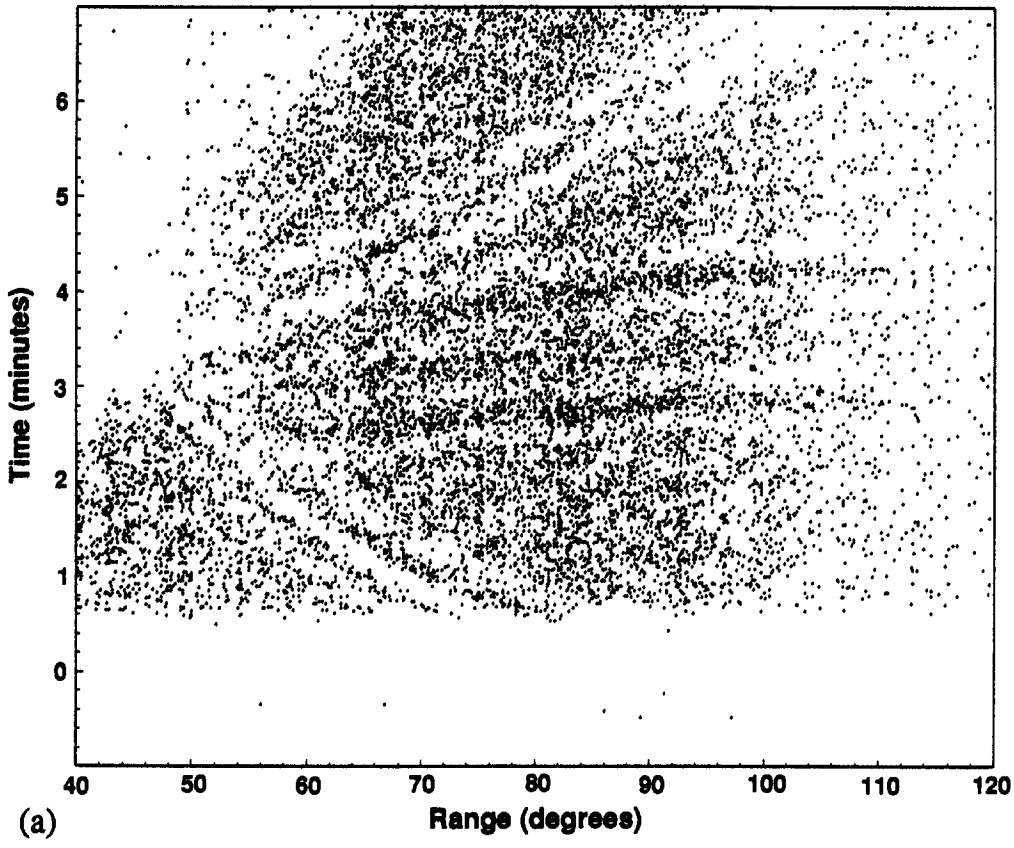

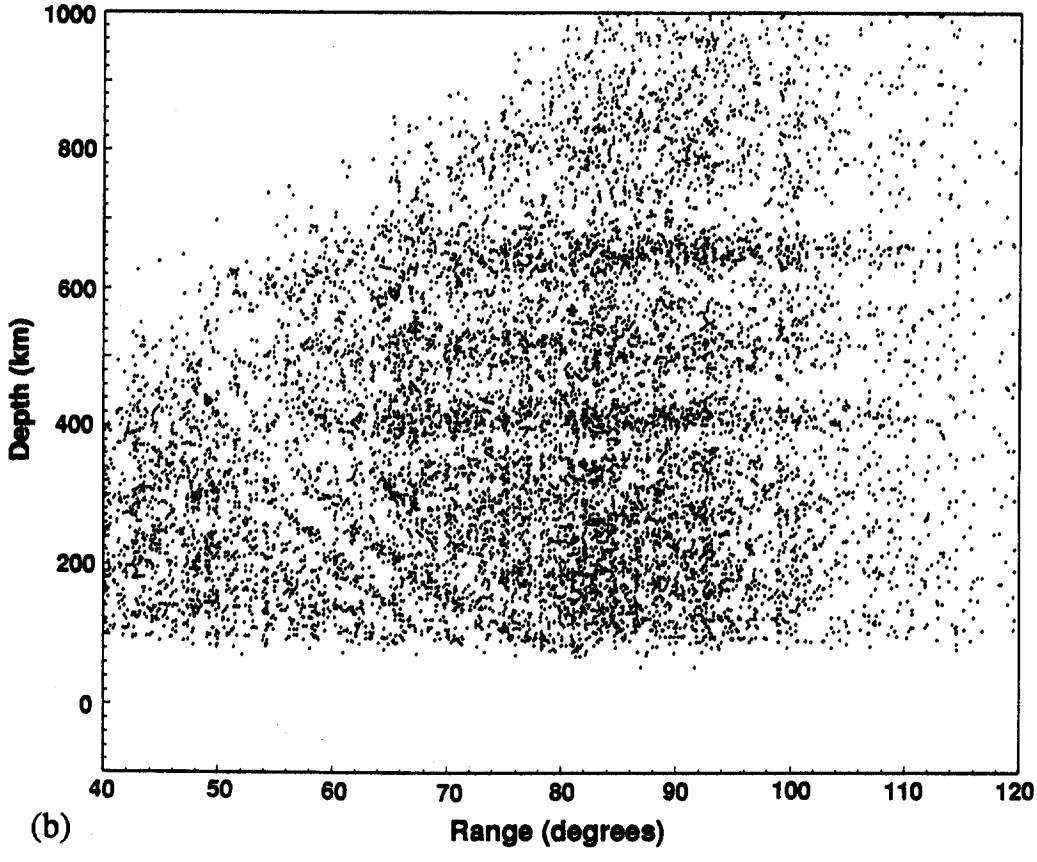

Fig. 11. Cross-correlation peaks for SH wave data, shown (a) as times from the reference phase (compare with Plate 3) and (b) as apparent discontinuity depths. The correlation coefficient r for each peak is less than -0.7 in order to resolve the phase-reversed reflections off the top of the upper mantle discontinuities.

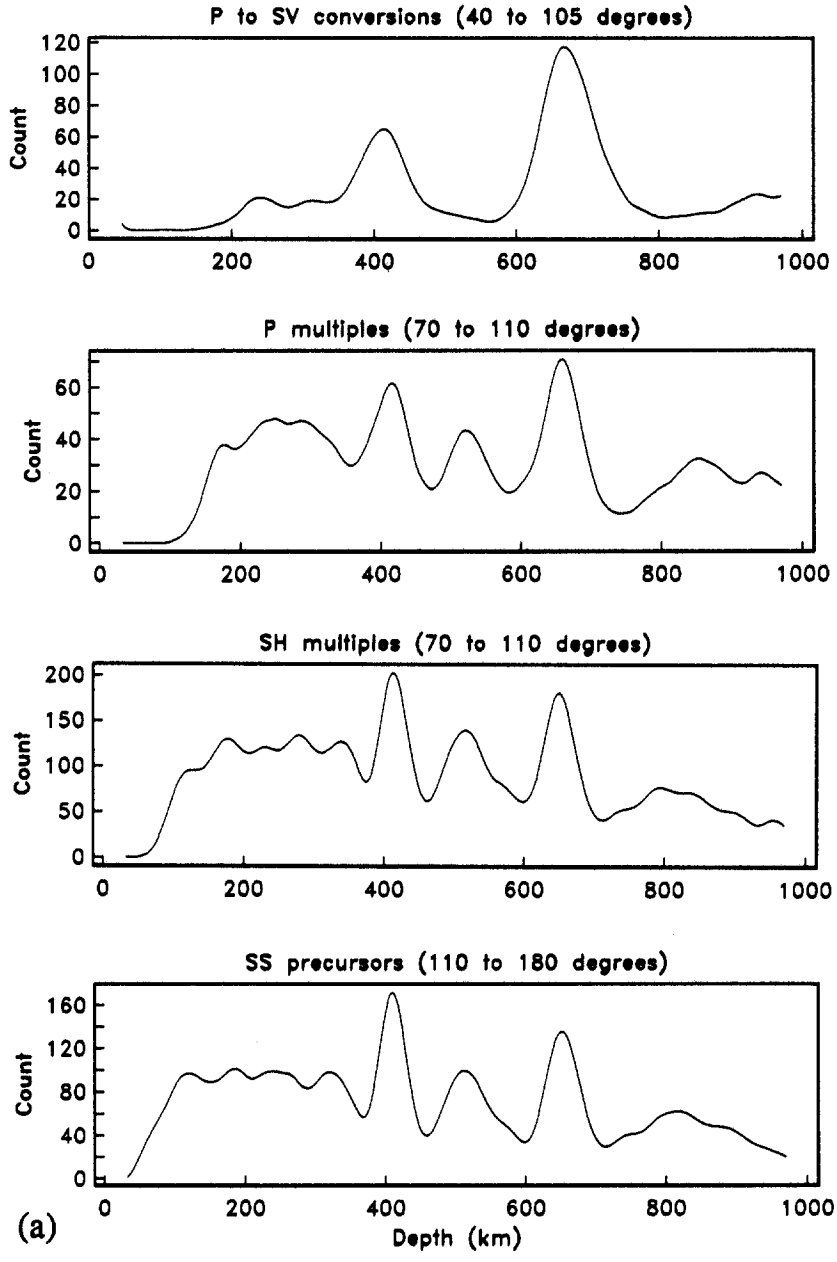

Fig. 12. Number of cross-correlation peaks as a function of apparent discontinuity depths for P-to-SV converted waves, P wave multiples, SH wave multiples, and SS precursors. Results have been smoothed and are shown in terms of number of peaks per 10-km depth increment. (*a*) Only positively correlated peaks are shown; (*b*) the difference between the positively and negatively correlated peaks is plotted (a positive correlation is one in which the observed polarity agrees with that predicted for the appropriate upper mantle discontinuity phase).

In principle, it might be possible to resolve dipping discontinuities or upper mantle anisotropy beneath seismic stations by observing azimuthal variations in apparent discontinuity depths. A preliminary analysis of the data shown in Figure 13 indicates that the azimuthal coverage at individual stations is generally very limited, making it difficult to detect reliably any azimuthal patterns. However, it is possible that more detailed analyses of individual stations may be able to demonstrate such effects.

Average apparent depths to the 410- and 660-km discontinuities are listed in Table 2 for those stations which show clear peaks in Figure 13 and have enough data for the bootstrap method to produce consistent estimates of standard errors. As in the analysis of the global averages listed in Table 1, depths are calculated both from the raw and WM.SS-S corrected data. Table 2 also lists the tectonic region of each station using the regionalization of *Jordan* [1981], and the $SS - S$ residual from the WM.SS-S model. Apparent depths to the discontinuities vary by less than about ±20 km, although the true scatter is probably less due to the large standard errors associated with many of the depth estimates. The average of the individual estimates of d'_{660} is 665 km as compared to the value of 669 km obtained using all of the data together. This indicates that the 669 km value may be biased due to a few stations with large amounts of data and large apparent depths to the 660-km discontinuity. Figure 14 compares 410-km

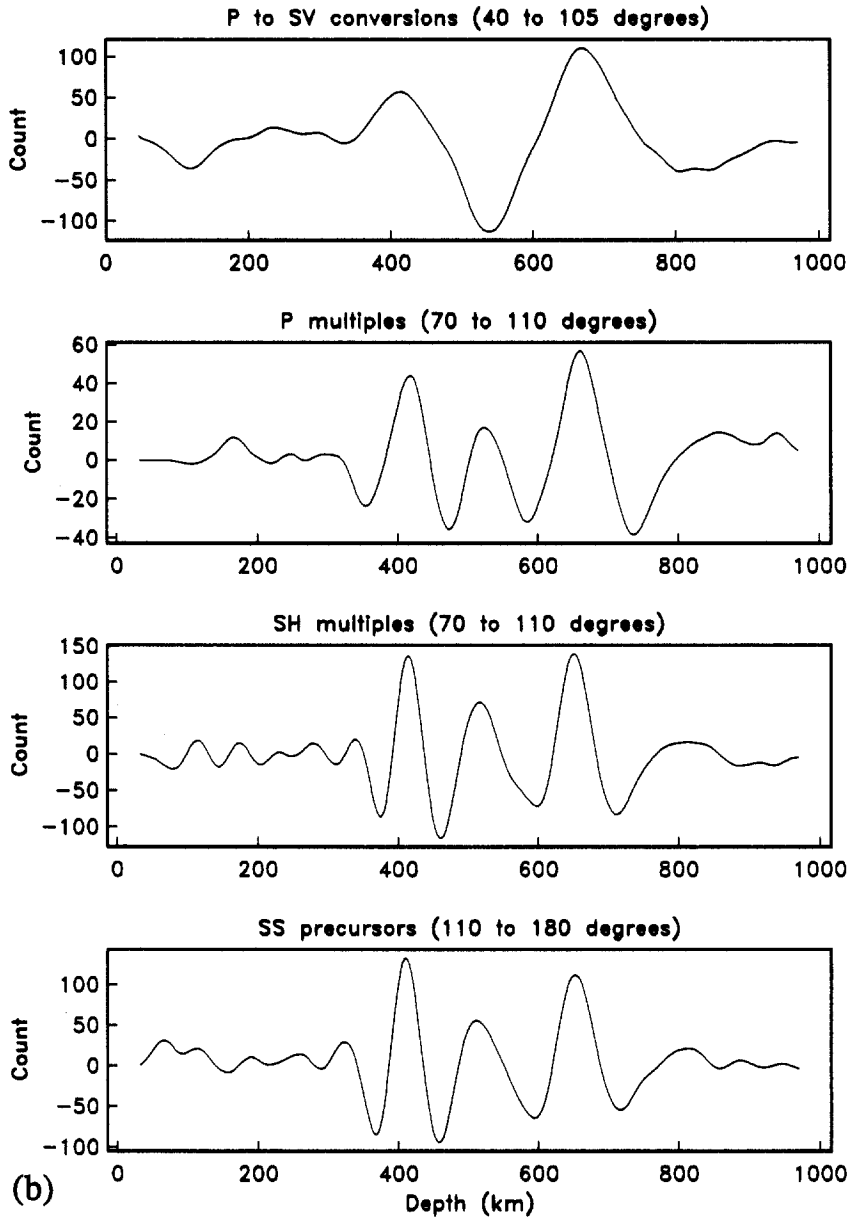

Fig. 12. (continued)

depths versus 660-km depths for both the raw and WM.SS-S corrected data. These plots exhibit considerable scatter with little correlation between the 410- and 660-km depths.

DISCONTINUITY DEPTHS FROM *SS* PRECURSORS

The precursors to *SS* are particularly useful for mapping possible lateral variations in discontinuity depths since each arrival can be associated with a single underside reflection point. Figure 15 shows *SS* midpoints and local ray azimuths for the *SS* precursor data used in this paper at ranges between 110° and 180°. These points are reasonably well distributed geographically, with particularly good coverage in the Pacific and Indian oceans at locations midway between the subduction zone earthquakes of the western Pacific and seismic stations in Europe and North America. Reliable estimates of discontinuity depths are not possible at each individual point shown in Figure 15 but can be obtained by examining groups of a dozen or more seismograms.

TABLE 1. Apparent Discontinuity Depths for Different Discontinuity Phases

Phase	t_{410}	d_{410}	e_{410}	d'_{410}	e'_{410}	t_{520}	d_{520}	e_{520}	d'_{520}	e'_{520}	t_{660}	d_{660}	e_{660}	d'_{660}	e'_{660}
P/SV conversions	41.5	412	4	414	4						63.4	666	2	669	3
P multiples	50.5	415	2	419	3	61.7	521	2	526	4	75.4	659	2	663	2
SH multiples	92.1	414	1	417	1	111.8	515	2	519	2	136.6	650	1	653	1
SS precursors	91.2	409	1	415	1	111.5	514	3	519	2	137.1	652	1	659	1

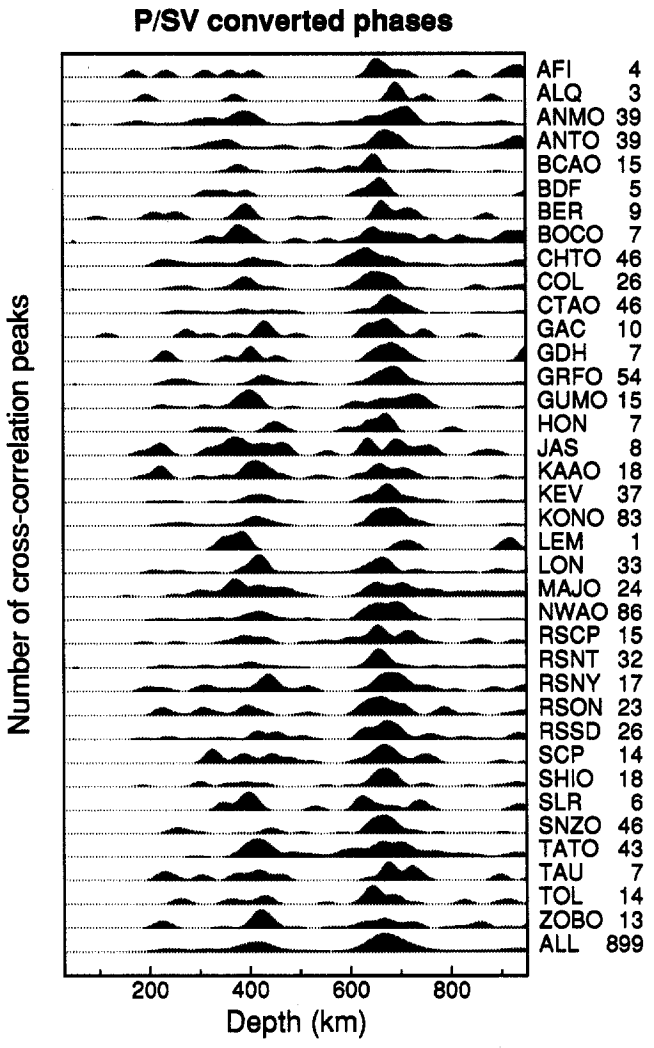

Fig. 13. Number of cross-correlation peaks as a function of apparent discontinuity depths for P-to-SV converted waves at 37 GDSN seismic stations. Each trace has been smoothed and self-scaled to unit amplitude; the numbers to the right of the station names indicate the number of peaks identified within 50 km of the 660-km discontinuity. The bottom trace shows the sum of all of the data and is identical to the P-to-SV curve in Figure 12.

Results for Different Tectonic Regions

In order to study possible regional differences in discontinuities depths, we divided the SS precursor data using the tectonic regionalization of *Jordan* [1981]. Figure 16 plots cross-correlation count versus apparent discontinuity depth for young oceans (<25 Ma), intermediate age oceans (25–100 Ma), old oceans (>100 Ma), Phanerozoic orogenic zones, and continental platforms and shields. The platform and shield data are combined due to the paucity of bounce points on the shields. The orogenic zone includes a wide variety of terrains including subduction zones and tectonically active continental regions. Figure 16*a* plots the number of waveforms with correlation coefficients relative to SS of 0.7 or greater, while Figure 16*b* plots the difference between the positive ($r > 0.7$) and negatively correlated pulses ($r < -0.7$). For each region, peaks can be identified for the 410-, 520-, and 660-km discontinuities. None of the regions show clear evidence for a 220-km discontinuity.

Table 3 lists apparent discontinuity depths for each of these five general tectonic regions, both for the raw data (d_{410}, d_{520}, and d_{660}) and the WM.SS-S corrected data (d'_{410}, d'_{520}, and d'_{660}). Standard errors for these estimates (obtained using the bootstrap method) are also listed (e_{410}, e'_{410}, etc.), as well as the one-way vertical S wave travel times to the discontinuities (t_{410}, t_{520}, and t_{660}). Notice the relatively good agreement in the apparent depths to the discontinuities between the different regions (412 ± 5 km, 518 ± 8 km, and 653 ± 8 km). These differences become even smaller after corrections are applied for upper mantle heterogeneity using the WM.SS-S model (415 ± 3 km, 518 ± 6 km, and 659 ± 5 km). The variations in the uncorrected apparent depths are consistent with known differences in upper mantle structure between the different regions. Old oceans, platforms and shields are generally cold and fast, resulting in shallower apparent discontinuity depths. In contrast, young oceans are typically hot and slow, causing deeper apparent discontinuity depths. The WM.SS-S corrections account for these differences in upper mantle structure and reduce the spread in discontinuity depths between the different regions. Figure 17 plots 410- versus 660-km depths for each of the five regions, both for the raw and WM.SS-S corrected data. Notice that the 660-km discontinuity exhibits considerably greater depth variations than the 410-km discontinuity.

Discontinuity Depths Near Subducting Slabs

An important question in mantle dynamics is the extent to which the upper mantle discontinuities are deformed by the presence of a subducting slab of relatively cold, dense material. The SS precursor bounce points (Figure 15) have particularly good coverage in the northwest Pacific, near the Kurile-Kamchatka and Japan subduction zones. Figure 18 shows an expanded map of this region, and the approximate position of where the subducting slabs intersect the 660-km discontinuity. This intersection curve was estimated from seismicity maps and analyses of deep seismicity and slab structure by *Isacks and Molnar* [1971] and *Burbach and Frohlich* [1986]. The curve is fairly well constrained for the Kurile-Kamchatka and Japan trenches, but some extrapolation at the bend was necessary in connecting these features.

In principle, information is available concerning discontinuity depths at each of the bounce points shown in Figure 18. However, the data are sufficiently noisy that stable discontinuity depths are obtained only if results are combined from a number of points. Before attempting to resolve fine details in discontinuity topography, it is important to examine the theoretical resolving power of the long-period SS precursor data set. The resolution of a reflected seismic phase can be estimated from the size of the Fresnel zone. Figure 19 plots the travel time difference in seconds for deviations in SS bounce point positions at ranges of 120°, 140°, and 160°. These plots were calculated for surface reflections; analogous plots for underside 410- and 660-km reflections are not significantly different. Notice that the SS bounce point is a saddle point rather than a minimum time path, consistent with the Hilbert transformed nature of this phase. The shape of this saddle point changes with range, becoming elongated in the off-axis direction for longer ranges. Due to the spherical geometry, SS at 180° is a pure maximum time point, with zero resolution in the off-axis direction. Energy will constructively interfere for travel times varying by $\pm T/4$, where T is the period of the wave. The long-period GDSN data contain little energy above 20 s, so the first Fresnel zone is approximated by the ±5-s contours in Figure 19, a

TABLE 2. Apparent Discontinuity Depths From P/SV Conversions at Different Stations

Station	Region	$SS-S$	t_{410}	d_{410}	e_{410}	d'_{410}	t_{660}	d_{660}	e_{660}	d'_{660}
AFI	C	-3.2					62.9	660	8	667
ANMO	Q	3.6	40.0	396	7	388	63.9	673	20	680
ANTO	Q	-2.3					63.9	673	7	679
BCAO	P	-0.3	39.8	394	18	391	61.8	646	3	647
BDF	S	-4.0					62.8	659	7	665
BER	Q	-0.5	39.6	392	5	393	63.3	665	5	667
BOCO	P	-1.3	39.2	388	12	390	62.6	656	13	657
CHTO	Q	1.6	41.3	410	6	407	61.4	641	13	640
COL	Q	2.3	39.7	393	8	388	62.6	657	11	655
CTAO	Q	1.9	40.8	404	21	409	64.5	680	3	675
GAC	S	-0.7	42.9	427	12	429	63.0	662	12	664
GDH	S	-2.5	40.7	403	4	408	63.4	667	12	672
GRFO	Q	-1.5	42.9	428	4	432	64.4	679	6	682
GUMO	Q	-4.0	40.5	401	4	410	63.5	667	16	674
HON	B	-3.8					63.1	663	9	670
KAAO	Q	-0.9	41.5	413	4	415	62.9	660	7	662
KEV	S	-4.5	41.9	417	9	424	64.0	673	6	683
KONO	Q	-0.7	41.9	417	4	419	63.9	673	7	675
LEM	Q	-2.4	38.7	383	13	387				
LON	Q	2.2	41.9	417	4	412	62.9	661	4	655
MAJO	Q	-0.8	40.9	405	18	403	62.7	658	9	658
NWAO	S	-4.0	41.9	416	6	425	63.2	664	12	666
RSCP	Q	-0.4	41.0	406	13	404	62.5	655	5	657
RSNT	S	0.5	40.7	403	7	401	62.7	658	3	656
RSNY	Q	-0.1	43.3	432	12	432	64.0	674	11	673
RSON	S	-0.7	40.4	400	10	401	62.6	657	8	659
RSSD	P	0.0	42.3	421	11	425	63.6	668	13	666
SCP	P	0.4					63.5	667	8	666
SHIO	Q	-1.5	41.0	407	13	409	63.4	667	8	669
SLR	S	-4.7	40.2	398	6	409	62.2	651	21	647
SNZO	Q	0.1	43.3	431	19	432	63.1	662	4	662
TATO	Q	0.6	41.8	415	7	414	63.3	665	11	664
TAU	Q	0.5	41.8	415	10	413	63.9	673	7	673
TOL	Q	-2.6	42.3	421	13	419	62.1	651	13	653
ZOBO	Q	0.4	42.4	422	5	422	62.9	660	13	661
All	Q	0.4	41.5	413	4	415	63.4	667	2	669

region about 15° across. However, the Fresnel zone may considerably underestimate the actual resolution of the data. In the case of PcP reflections off the core-mantle-boundary, *Weber and Davis* [1990], citing work of *Kampfmann and Müller* [1989] and *Safar* [1989], argue that the actual area contributing energy coherently to a single receiver is only a third the size of the Fresnel zone. If these arguments can be extended to SS reflections, then the resolution of the SS precursors is about 5°.

Assuming the slab intersection curve shown in Figure 18, the data may be binned by distance from the slab intersection, and discontinuity depth estimates obtained for each range bin. Figure 20 plots apparent 410- and 660-km discontinuity depths for both the raw and WM.SS-S corrected data as a function of closest perpendicular distance to the slab intersection curve. Depths are shown at 2° range increments with each point including data within a 4° range window. Apparent depths to the discontinuities for the WM.SS-S corrected data vary by less than ±12 km for the 410-km discontinuity and by less than ±22 km for the 660-km discontinuity. Apparent depths to the 660-km discontinuity are depressed by about 20 km in a broad 10°- to 15°-wide region in the vicinity of the subducting slab. This feature is not symmetric about the slab intersection point, extending further to the west (backarc) side of the descending slab. Because of the limited resolution of these long-period reflections, it is conceivable that a steep depression or break in the 660-km discontinuity could be missed if it were only a few degrees wide. It also appears from Figure 20 that apparent depths to the 410-km discontinuity may be depressed by 10 km in the vicinity of the slab, although this feature is not as clear as the dip in the 660-km discontinuity. Figure 21 plots apparent depths to the 660-km discontinuity versus depths to the 410-km discontinuity for the points shown in Figure 20. These depths are somewhat correlated, at least for the uncorrected data, with the 660-km discontinuity exhibiting significantly greater depth variations than the 410-km discontinuity.

AMPLITUDE ANALYSIS

A detailed comparison between the amplitudes of the upper mantle discontinuity phases shown in Plates 1–5 and those of synthetic seismograms is beyond the scope of this paper. However, the amplitude of a discontinuity phase compared to a reference phase is mainly determined by the reflection and/or transmission coefficient at the discontinuity. By using ray theory, it is possible to obtain approximate values for the P and S wave reflection coefficients and the P-to-SV transmission coefficients at each discontinuity from the amplitudes of the appropriate upper mantle discontinuity phases. These coefficients are directly related to the velocity and density contrasts across the discontinuities, and conceivably it might even be possible to determine separately both the density and velocity jumps by comparing results

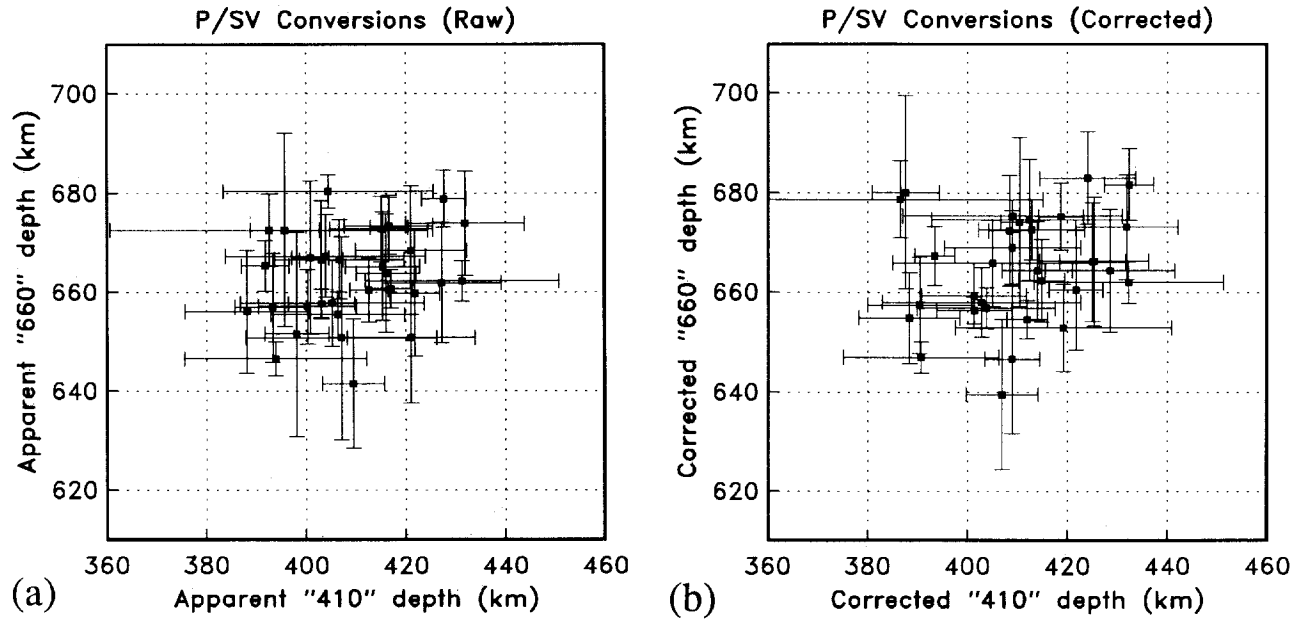

Fig. 14. The 410- versus 660-km apparent discontinuity depths from P-to-SV converted phases at individual seismic stations obtained using (*a*) raw times and (*b*) WM.SS-S corrected times. These data points, including standard error bars, are also listed in Table 2.

for different phases and ranges. For example, the SH wave reflection coefficient, which affects the amplitude of the S multiples and SS precursors, is sensitive to the S wave impedance change ($\beta\rho$) across the discontinuity (where β is the shear velocity and ρ is density). In contrast, the P-to-SV converted phases are mainly sensitive to the S velocity jump β alone. By comparing the amplitudes for these phases, it should be possible to determine both the velocity and density jumps at the discontinuities.

However, obtaining accurate and unbiased estimates of the amplitudes of these phases is not easy. There are two main difficulties: the weak amplitude of the phases and the

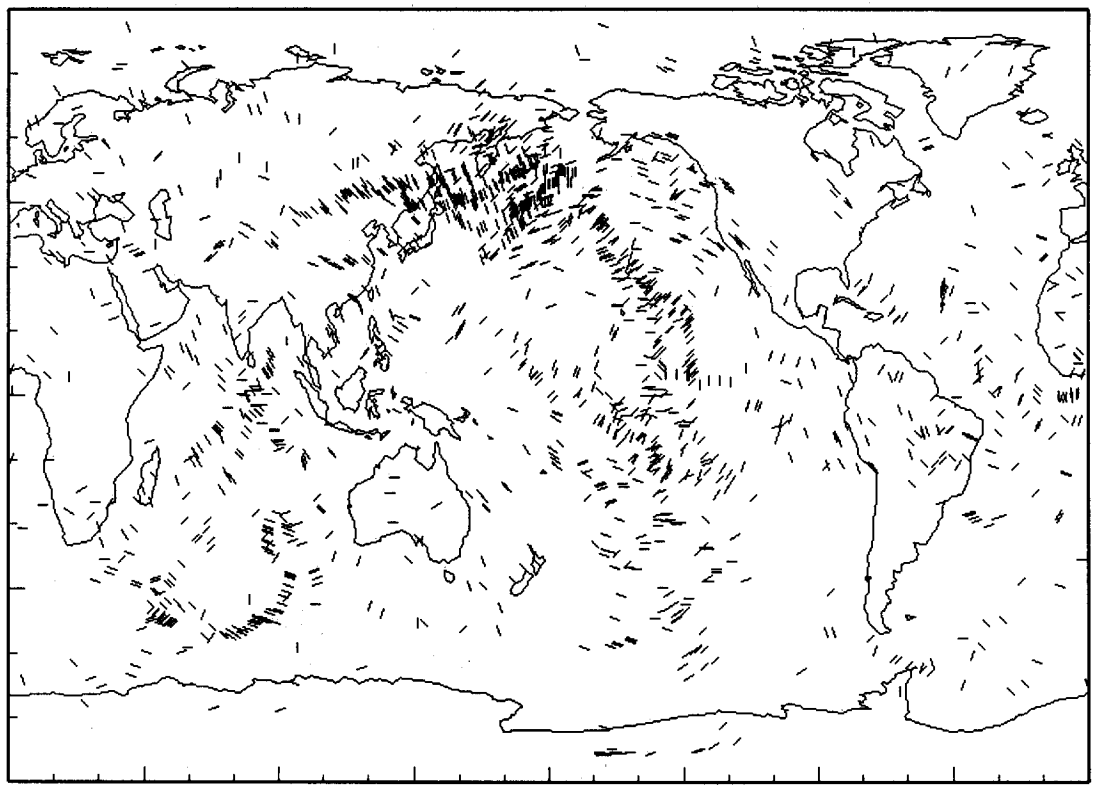

Fig. 15. SS precursor bounce points at source-receiver ranges between 110° and 180°. The local ray azimuth at the bounce point is indicated by the orientation of the lines. Note the dense coverage in the northwest Pacific.

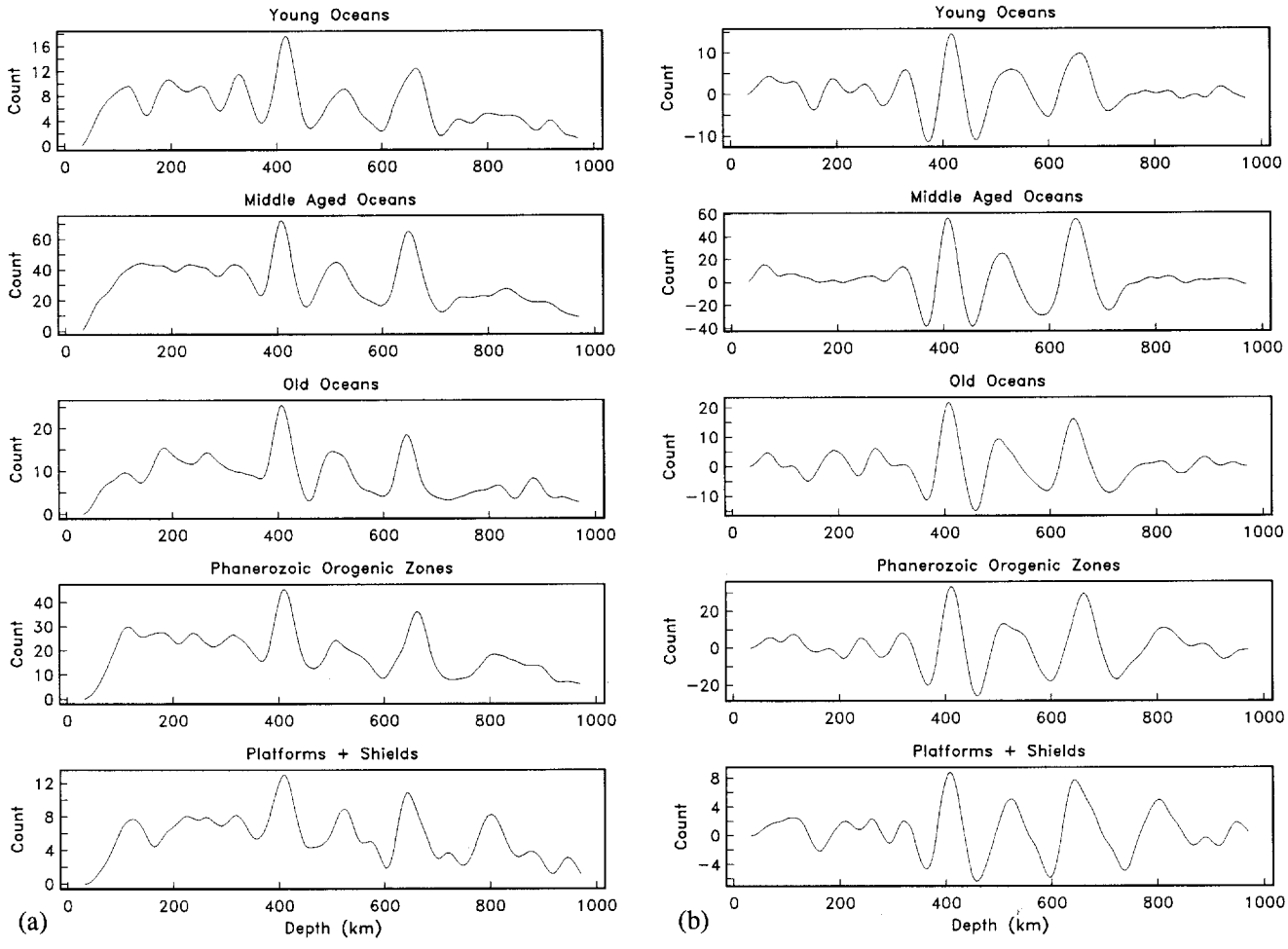

Fig. 16. Number of cross-correlation peaks as a function of apparent discontinuity depths for SS precursors, shown for different tectonic regions. (*a*) Only positively correlated peaks are shown; (*b*) the difference between the positively and negatively correlated peaks is plotted. Tectonic regionalization is from *Jordan* [1981].

effects of incoherent stacking. The discontinuity phases are relatively weak arrivals which are close to the signal-to-noise level on individual seismograms. Thus, in general, they are positively identified only when they are anomalously large. Simple averages of the amplitudes corresponding to the cross-correlation peaks obtained from individual long-period seismograms invariably lead to values which are unrealistically high. A less biased measure of discontinuity phase amplitudes can be obtained from the stacks (Plates 1–5) which combine data from all available seismograms. However, the amplitudes in these stacks are reduced by the effects of incoherent stacking, resulting from small time shifts caused by upper mantle heterogeneity and/or discontinuity topography.

Figure 22 plots apparent amplitudes of the P-to-SV converted phases, the P multiples, the SH multiples, and the SS precursors for the 410-, 520-, and 660-km discontinuities as obtained from the stacked images (before median filtering). Amplitudes are measured by stacking the waveforms along the predicted travel time curve for each phase and finding the maximum amplitude within 10 s of the predicted travel time. Figure 22*a* shows results at 2° increments, while Figure 22*b* plots results at 5° spacing. These amplitude versus range curves exhibit considerable jitter, as might be expected from the sometimes irregular and intermittent appearance of the arrivals in the stacked images. In some cases these irregularities can be attributed to interference from other phases; for example, the underside precursor phases to SS cause distortions where they cross the S multiples at ranges between 80° and 110°. In most cases, however, the scatter in the observed amplitudes probably reflects changes in the source-receiver locations as a function of range. While the overall global coverage of sources and receivers is fairly widespread (see Figure 1), the seismograms available within any particular range bin may be dominated by only a few source-receiver paths. As the range changes the stacked phases are likely to be sensitive to different regions and subject to varying effects of heterogeneity and scattering. Since amplitudes of the upper mantle discontinuity phases in these stacks are relative, the reference phase amplitudes are also important. At ranges beyond about 95°, the P and S wave amplitudes are very sensitive to changes in the velocity structure within D″ and near the core-mantle boundary. The steep rise in the relative amplitudes of the P-to-S converted phases above 110° and the increased SH multiple amplitudes above 105° are probably caused by the amplitude decay with range of P_{diff} and S_{diff}.

In most cases the amplitudes plotted in Figure 22 are smaller than typical upper mantle velocity models predict. For example, synthetic seismograms calculated from PREM

TABLE 3. Apparent Discontinuity Depths From SS Precursors for Different Tectonic Regions

Region	t_{410}	d_{410}	e_{410}	d'_{410}	e'_{410}	t_{520}	d_{520}	e_{520}	d'_{520}	e'_{520}	t_{660}	d_{660}	e_{660}	d'_{660}	e'_{660}
Young oceans	92.6	417	2	416	2	113.7	525	6	520	6	138.6	661	5	654	4
Intermediate oceans	90.8	408	1	414	1	111.4	513	4	518	4	136.7	650	2	658	1
Old oceans	90.9	408	2	417	2	110.8	510	6	520	5	135.7	645	2	657	2
Orogenic regions	91.4	411	2	412	2	111.7	514	6	512	7	138.7	661	3	664	3
Platforms and shields	90.8	408	3	415	2	113.3	523	5	523	5	136.6	650	5	664	4

using a normal mode summation technique [*Shearer and Masters*, 1990] indicate that the $S660S/SS$ amplitude ratio is about 0.06 between 120° and 130°, compared to a ratio of about 0.03 for the data plotted in Figure 22. These synthetics have a $Ss660s/S$ amplitude ratio of 0.09 between 70° and 80°, while the corresponding ratio for the stacked data is about 0.03. The PREM impedance contrast for the 660-km discontinuity (16% change in $\beta\rho$ at 670 km) would need to be reduced by a factor of 2–3 to directly explain these observed amplitudes. A much more likely explanation for the discrepancy between data and synthetics is that incoherent stacking has reduced the amplitudes of the discontinuity phases. The problem is to quantify the size of this effect.

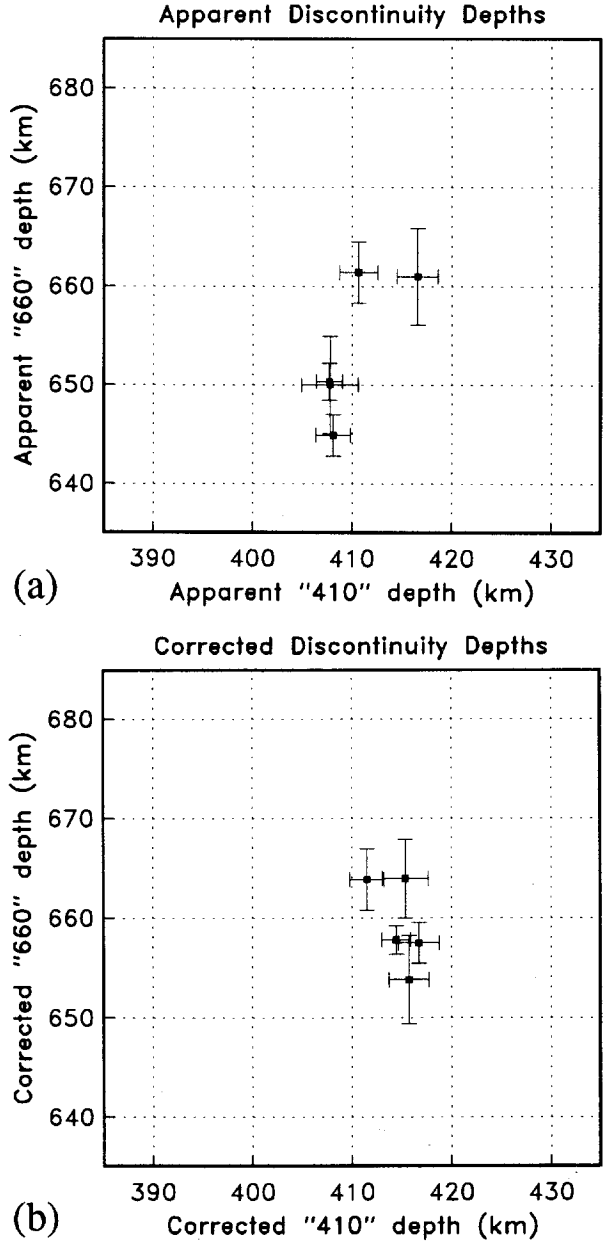

Fig. 17. The 410- versus 660-km apparent discontinuity depths from SS precursors in different tectonic regions obtained using (*a*) raw times and (*b*) WM.SS-S corrected times. These data points, including the one standard error bars, are also listed in Table 3.

Revenaugh and Jordan [1991*a*] faced a similar difficulty in modeling the amplitudes of discontinuity reflectors in ScS reverberation data. They assumed that the time shifts which contribute to the incoherent stacking could be modeled as a Gaussian distribution specified by a standard deviation σ. For a given value of σ it is possible to determine the amount of pulse broadening and amplitude reduction which occurs for any reference wavelet. Revenaugh and Jordan obtained an estimate of σ = 4 s by examining how the amplitude of the 660-km peak changed for low-pass-filtered versions of their data (the effects of incoherent stacking are reduced at lower frequencies due to wider pulse widths). In principle, this approach could also be used to determine the appropriate σ values for the upper mantle discontinuity phases shown in Plates 1–5 by low-pass filtering the seismograms prior to stacking. Unfortunately, attempts to estimate σ in this way produced inconclusive results. The amplitudes in the stacked images did not change in predictable ways for the different frequency bands. In some examples the amplitude of the 660-km phase actually decreased at lower frequency bands, even in cases where the 660- and 410-km wavelets were well separated in time.

An alternative approach to estimating σ is to measure the width of the peaks shown in Figure 12. In this case the apparent depths are first converted to the appropriate vertical travel time (two-way P for the P multiples, two-way S for the S multiples and SS precursors, and one-way $S - P$ for the P-to-SV converted phases), and the best fitting normal distribution is found for the central part of the peaks. Estimated σ values for the 660-km discontinuity phases were 6–7 s for the SS precursors, 6–9 s for the S multiples, and 5–8 s for the P multiples. However, these values are likely to be biased toward larger values due to the effect of background noise on individual seismograms which will tend to randomly shift the observed cross-correlation peaks. This hypothesis is supported by the fact that σ values obtained in this way are not significantly different for the P and S phases, whereas time shifts caused by discontinuity topography or lateral heterogeneity should be roughly a factor of 2 smaller in the case of the P multiples due to the faster P wave velocities.

Ignoring the effects of discontinuity topography, a lower bound on σ may be obtained from models of heterogeneity in the upper mantle. The $SS - S$ residual data set of *Woodward and Masters* [1991] (used to correct the apparent discontinuity

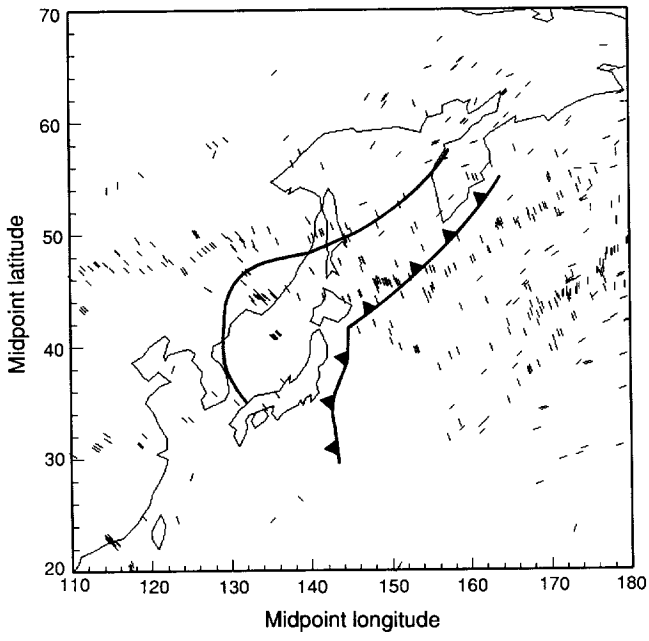

Fig. 18. *SS* precursor bounce points in the northwest Pacific at source-receiver ranges between 110° and 180°. The local ray azimuth at the bounce point is indicated by the orientation of the lines. The solid line indicates the approximate position where the subducting slabs intersect the 660-km discontinuity.

depths) predicts a global σ value of about 3.5 s. However, it is unclear if a single global value of σ is appropriate to use in correcting amplitudes along a given discontinuity phase. As discussed above, the changes in ray path coverage with distance make it likely that σ will be range dependent. At some ranges, only a few regions on the earth will be sampled and the effective value of σ could be reduced. The size of the amplitude correction factor depends strongly on the choice of σ. For $\sigma = 4$, the amplitudes shown in Figure 22 for *Ss660s* and *S660S* should be increased by a factor of about 1.6, whereas for $\sigma = 6$ the correction factor is 2.5.

The *P*-to-*SV* converted phases should be less susceptible to the effects of incoherent stacking because shifts in one-way $S - P$ times are likely to be much smaller than in two-way S times. However, the observed amplitudes (Figure 22) exhibit considerable scatter with several unexplained features. It is unclear why the *P660s* amplitudes increase so much below 50° or why the *P410s* arrivals fade out near 57° and 75°. Figure 23 shows the result of using ray theory to convert the amplitudes shown in Figure 22*b* into *P*-to-*SV* transmission coefficients as a function of ray parameter. This calculation takes into account geometrical spreading and surface ray-angle differences but ignores the effects of attenuation. Upper mantle *P*-to-*SV* converted phases are mainly sensitive to the shear velocity contrast across the discontinuities. The theoretical curves shown in Figure 23 were computed assuming an *S* velocity contrast of 8% at both 410 and 660 km. These velocity changes are much higher than almost all upper mantle velocity models, and, given the scatter in the data, it is difficult to have much confidence that they are real. In general, the uncertainties involved in modeling absolute amplitudes for the upper mantle discontinuity phases are sufficiently large that no reliable conclusions are possible without further analysis.

However, greater accuracy is possible in comparing the amplitudes of phases from different discontinuity depths,

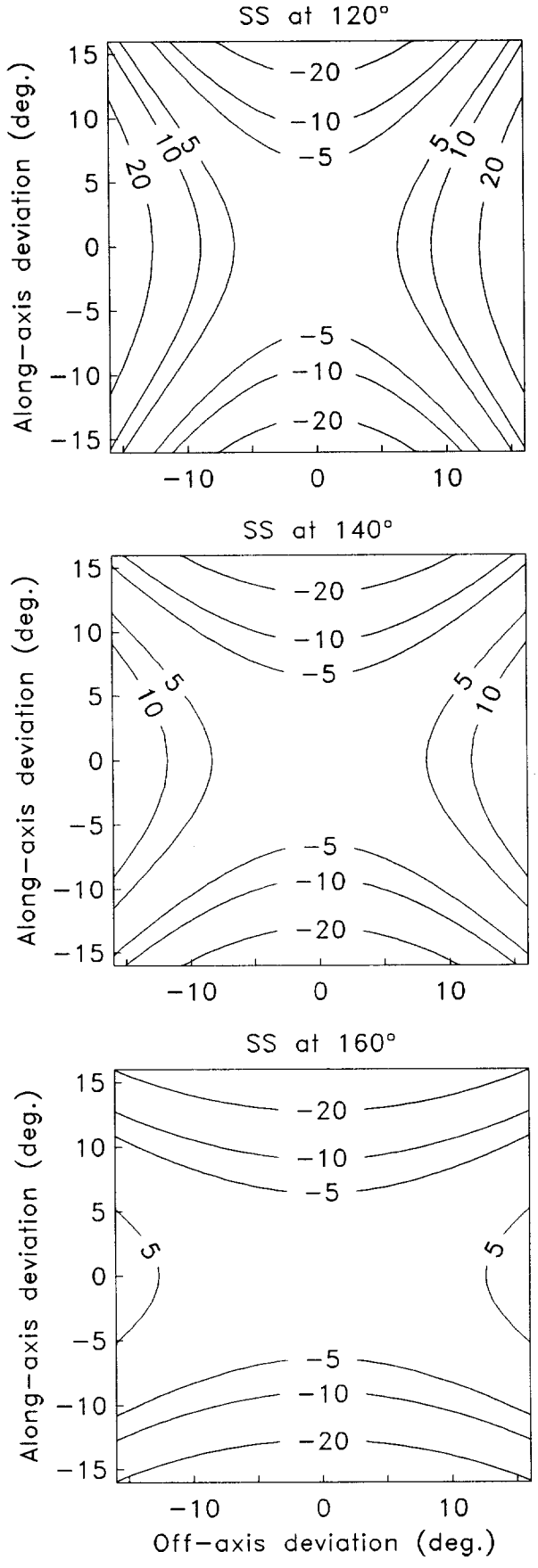

Fig. 19. The change in travel time resulting from perturbations in the *SS* bounce point position, shown for source-receiver ranges of 120°, 140°, and 160°. Note that the *SS* bounce point is a saddle point, rather than a minimum or maximum time path. The Fresnel zone for 20-s waves is given by the ±5-s contours.

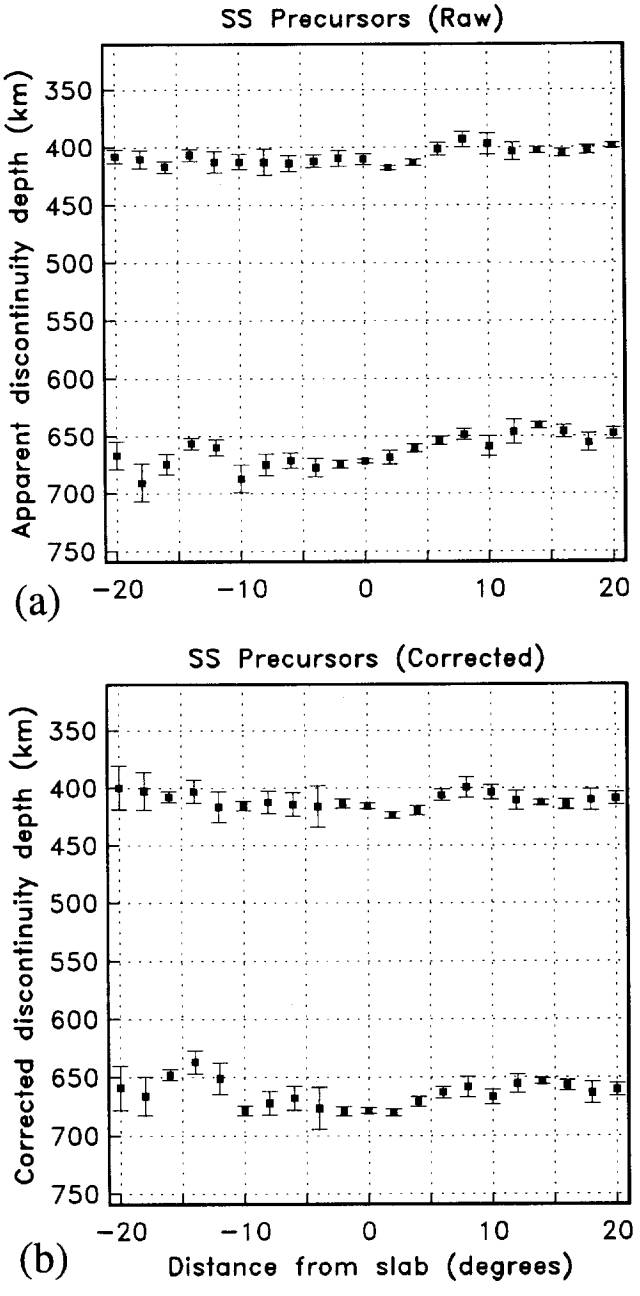

Fig. 20. Apparent and corrected discontinuity depths as a function of distance from the 660-km slab intersection obtained using (*a*) raw times and (*b*) WM.SS-S corrected times. Positions east to northeast from the slab intersection line drawn in Figure 18 are shown as negative distances. Each point contains data from ±2° in distance; adjacent points contain half their data in common. One standard error bars are also shown.

since biases due to incoherent stacking or other effects are likely to be similar between phases. The mean amplitude ratio A_{410}/A_{660} as measured from the values plotted in Figure 22*b* is 0.86 ± 0.17 for *P*-to-*SV* conversions (65° to 95°), 1.13 ± 0.50 for *P* multiples (75° to 95°), 0.89 ± 0.15 for *SH* multiples (70° to 95°), and 1.03 ± 0.18 for *SS* precursors (110° to 165°). The slightly increased relative amplitude of the 410-km discontinuity phase for the *SS* precursors compared with the *SH* multiples is puzzling since both transition zone attenuation and geometrical spreading effects would predict the opposite relationship (i.e., *S*660*S* has a shorter path than *S*410*S*, *Ss*660*s* has a longer path than *Ss*410*s*, see Figure 10). This inconsistency, which also shows up in comparisons with synthetic seismograms, suggests that these amplitude ratios may be in error by 10–20%. However, the rough agreement in the amplitude ratios between the different discontinuity phases suggests that 0.8–1.1 is a reasonable estimate of the size of the *P* and *S* impedance change at 410 km compared to the change at 660 km.

In contrast with this estimate, PREM *P* and *S* wave impedance changes at 670 km are almost twice the size of the changes at 400 km and predict A_{410}/A_{660} amplitude ratios of about 0.5–0.7. However, the PREM *P* wave velocity contrast of 2.6% at 400 km is unusually low compared to most recent velocity models (see *Nolet and Wortel* [1989] for a review of upper mantle models). These models contain *P*

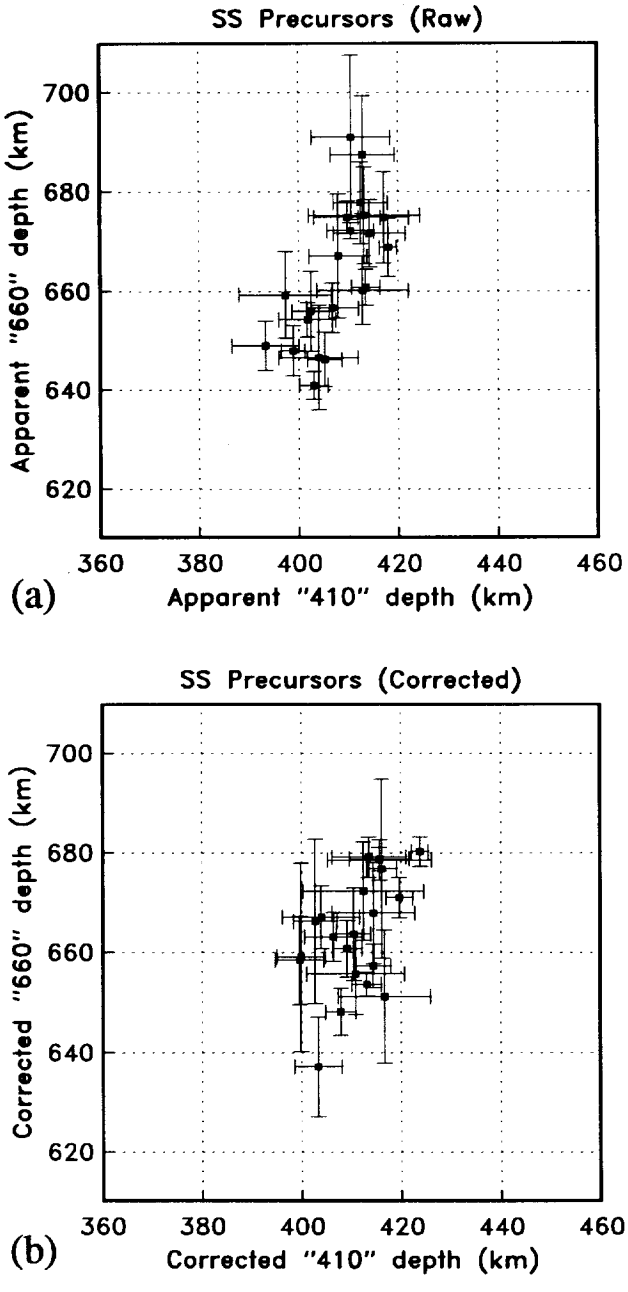

Fig. 21. The 410-km versus 660-km apparent discontinuity depths in the northwest Pacific for the *SS* precursor data in Figure 20, obtained using (*a*) raw times and (*b*) WM.SS-S corrected times.

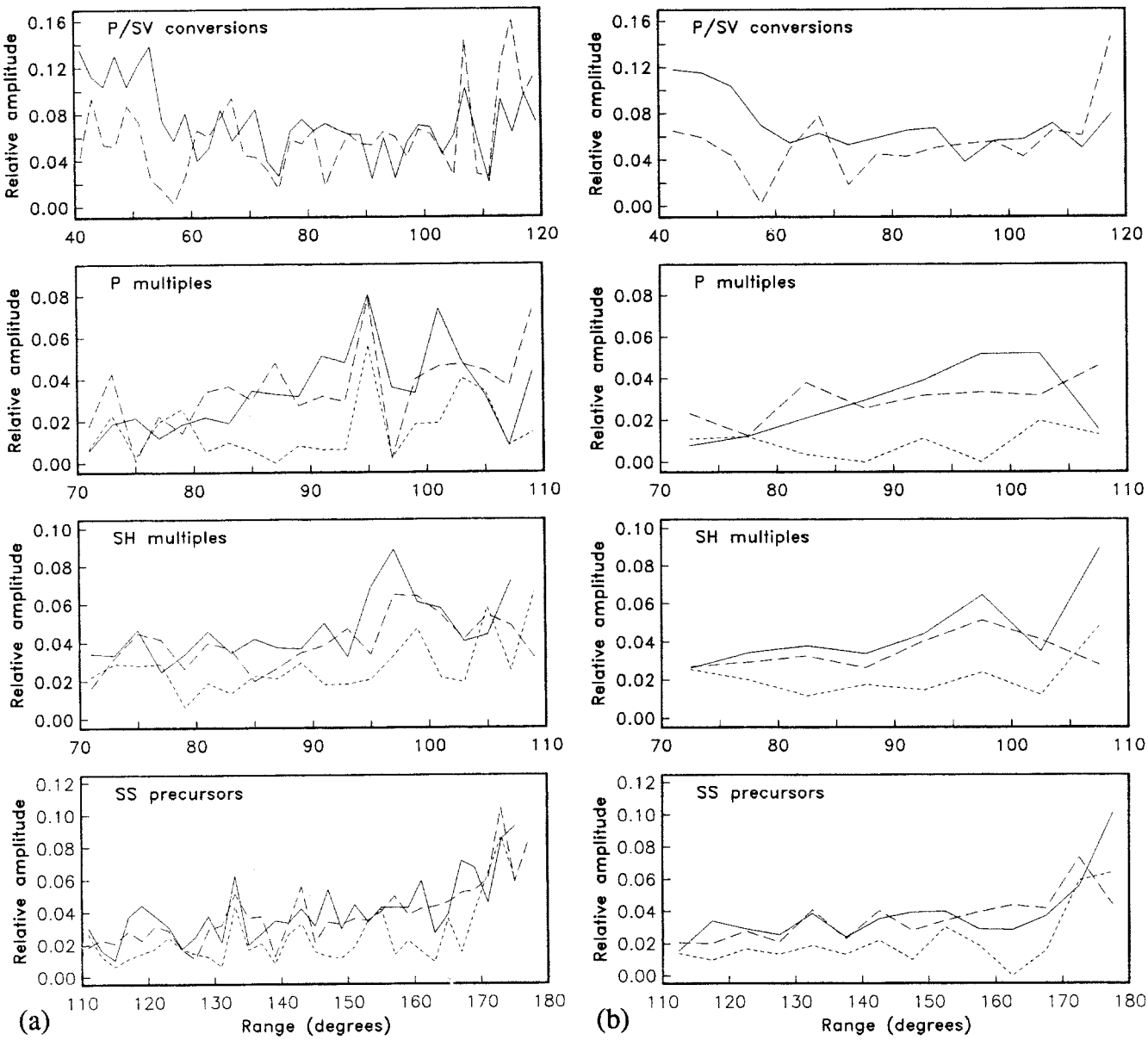

Fig. 22. Amplitudes (relative to the reference phase) of the 660-km (solid lines), 410-km (dashed lines), and 520-km (dotted lines) discontinuity phases obtained from the waveform stacks. Measured amplitudes are obtained by stacking along the travel time curve of the desired phase at (*a*) 2° increments, and (*b*) 5° increments.

wave contrasts near 410 km ranging from 4.4% to 6.8% and similar or even smaller values for the contrast near 660 km [*King and Calcagnile*, 1976; *Fukao*, 1977; *Burdick and Helmberger*, 1978; *Given and Helmberger*, 1980; *Burdick*, 1981; *Walck*, 1984; *Leven*, 1985; *LeFevre and Helmberger*, 1989]. Thus, while the observed similarity in *Pp*410*p* and *Pp*660*p* amplitudes does not agree with PREM, it does appear to be consistent with the majority of upper mantle *P* wave models.

Shear wave models for the upper mantle are less common but contain velocity contrasts near 410 and 660 km that are in rough agreement with PREM. The *S* wave models of *Grand and Helmberger* [1984*a*,*b*] contain velocity contrasts of 4.5% at 405 km and 7.2% at 660 km, indicating a 410/660 ratio of about 0.6. Using long-period *ScS* reverberation data, *Revenaugh and Jordan* [1991*a*] obtained estimates of the 410-km and 660-km reflection coefficients which imply that the *S* impedance contrast at 410 km is about 0.6 the size of the contrast at 660 km. All of these ratios are significantly lower than those obtained from the waveform stacks of *S* multiples, *SS* precursors, and *P*-to-*SV* converted phases. One possible explanation for this discrepancy could be that the observed greater variability in the apparent depths to the 660-km discontinuity has resulted in larger reductions in apparent amplitudes due to incoherent stacking for the 660-km phases. The Revenaugh and Jordan results were obtained at lower frequencies (40 s) where the effects of incoherent stacking are less important. However, it is difficult to see how differences in incoherent stacking corrections could be large enough to explain the observed inconsistency of about 40% in the 410/660 amplitude ratio obtained from these stacks compared to other studies, particularly for the *P*-to-*SV* converted phases.

The amplitude of the 520-km discontinuity can be measured

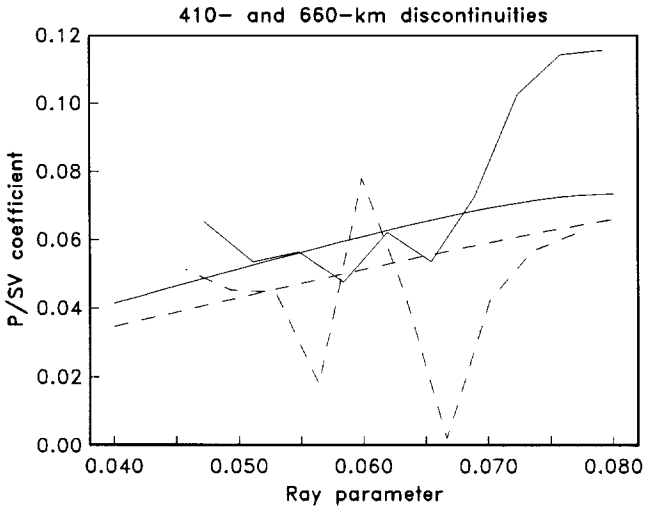

Fig. 23. Apparent upgoing P-to-SV transmission coefficients obtained from the waveform stacks for the 410-km discontinuity (bumpy dashed line) and 660-km discontinuity (bumpy solid line) as a function of ray parameter. The smooth curves show the fit obtained by assuming velocity and density contrasts of 8% at the discontinuities. The data curves were obtained from the amplitudes of the P-to-SV converted phases shown in Figure 22, after correcting for geometrical spreading and ray angle differences. Note that the theoretical transmission coefficients increase as the rays strike the discontinuities more obliquely (i.e., at greater ray parameters). This is why the transmission coefficients at 660 km are slightly higher than the coefficients at 410 km (the higher velocities at 660 km result in more horizontal ray paths). The ray parameters in this plot are appropriate for the actual velocities at the discontinuities (not the Earth flattened velocities).

relative to the 410-km discontinuity. The mean amplitude ratio A_{520}/A_{410} as determined from the values plotted in Figure 22*b* is 0.36 ± 0.22 for P multiples (75° to 95°), 0.60 ± 0.11 for SH multiples (70° to 95°), and 0.52 ± 0.07 for SS precursors (110° to 165°). The $Ss520s$ and $S520$ amplitudes are probably overestimated because these phases arrive at nearly the same time as a positive sidelobe of the 410-km phase. It is possible to correct for this effect by noting the sidelobe heights of the reference pulse (see examples in Figure 4). Due to the asymmetry in the sidelobe amplitudes about the main pulse, this effect is larger for the SH multiples than the SS precursors. Corrected values of A_{520}/A_{410} are 0.45 ± 0.08 for SH multiples, and 0.47 ± 0.07 for SS precursors. A conservative interpretation of these results suggests that the P and S wave impedance contrasts at 520 km are between 30% and 60% the size of the contrast at 410 km.

Estimates of discontinuity phase amplitudes obtained from individual long-period seismograms exhibit considerable scatter and are generally biased toward large values. Figure 24 plots 660- versus 410-km amplitudes for P-to-SV converted phases, P multiples, SH multiples, and SS precursors. Each point shows amplitudes obtained from a pair of cross-correlation peaks on a single seismogram, for which the apparent depths were within 30 km of 410 and 660 km (±50 km for the P-to-SV converted waves). Note the rough but consistent correlation between 410- and 660-km amplitudes. This correlation is most likely a result of the focusing and defocusing effects of lateral heterogeneity along the ray paths. Since the ray paths for the 410- and 660-km discontinuity phases are much closer to each other than to the reference phase ray path, these variations will naturally result in correlated 410- and 660-km amplitudes. Focusing due to discontinuity topography is a less probable explanation since temperature variations in the transition zone would cause the 410-km and 660-km discontinuities to move in opposing directions due to the opposite sign of their Clapeyron slopes. Direct variations in impedance or roughness on the discontinuities are also possible but unlikely to be responsible for the large changes (factors of 5 and greater) in amplitude seen in Figure 24.

Revenaugh and Jordan [1991*a*] observed a correlation between the S wave reflection coefficient and apparent depth of the 660-km discontinuity, with the reflection coefficient becoming smaller as the discontinuity becomes deeper. In order to examine the possibility of a such a correlation, I computed apparent depths (WM.SS-S corrected) to the 410- and 660-km discontinuities as a function of SS precursor amplitudes. Figure 25 shows the results of this analysis for the entire SS precursor data set and for the near-slab data from the northwest Pacific (also shown in Figure 20). The global data are binned at increments of 0.05 in amplitude, while the less numerous near-slab data are binned at increments of 0.1. Despite large variations in amplitude, computed depths to the discontinuities vary by less than 10 km, with no correlation with amplitude. As discussed above, most of the observed amplitude variations are probably due to ray path focusing effects which have nothing to do with discontinuity reflection coefficients. However, apparent depths to the 660-km discontinuity exhibit lateral variations of up to 30 km for the near-slab data (see Figure 20), a depth change which the Revenaugh and Jordan observations suggest may be associated with a factor of 2 change in the 660-km reflection coefficient. Despite the large scatter in the observed SS precursor amplitudes, the results shown in Figure 25 appear to be inconsistent with such a strong depth dependence of amplitude. The Revenaugh and Jordan study examined regions in the southwest Pacific and Indonesia, areas that contain relatively few SS precursors, so it is possible that the depth-amplitude dependence is specific to these regions.

THE 520-km DISCONTINUITY

The P, SH, and SS wave stacks suggest the presence of phases resulting from reflections off a 520-km discontinuity, with apparent amplitudes roughly half the size of the 410-km discontinuity phases. However, because these phases occur between the 410- and 660-km phases, the possibility must be considered that they are artifacts from the sidelobes of these phases. Several factors argue against this interpretation and suggest that the 520-km phases are real. These include the following:

1. The 520-km phases are not centered between the 410- and 660-km phases but are closer in time to the 410-km phases. The time separation is too great for them to be affected by the sidelobes of the 660-km phases.

2. The 520-km phases are adjacent to the 410-km phases, but no corresponding phases are seen adjacent to the 660-km phases.

3. Cross-correlation analyses of the $Pp520p$, $Ss520s$, and $S520S$ phases give the same apparent depth to the 520-km discontinuity despite the different time separation between the P and S wave phases due to the different velocities of P and S. If the 520-km phase were simply a sidelobe of the 410-km phase, one would expect its apparent depth to be

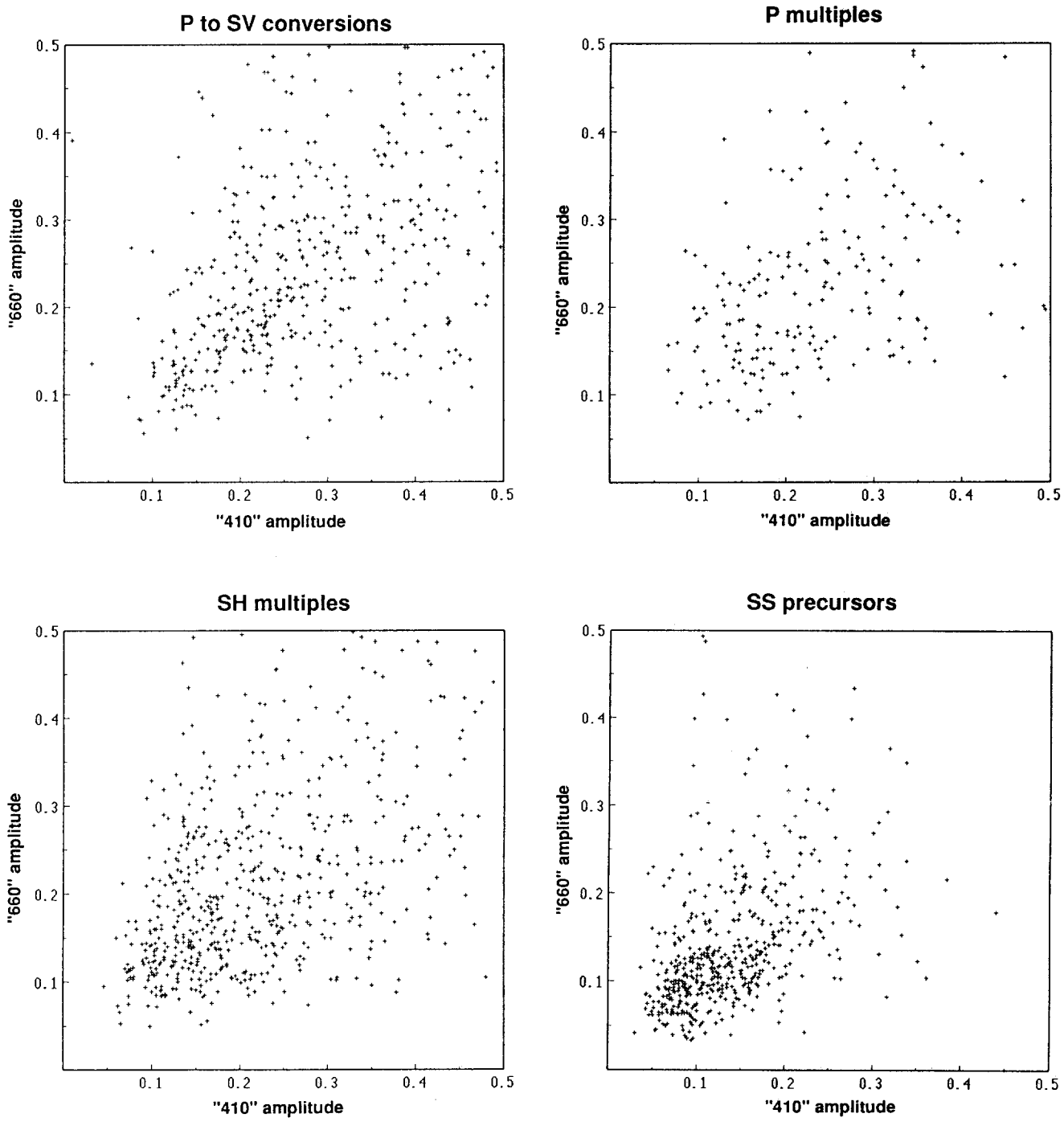

Fig. 24. The 410- versus 660-km discontinuity phase amplitudes for P-to-SV converted waves, P wave multiples, SH wave multiples, and SS precursors. Each point shows amplitudes obtained from a pair of cross-correlation peaks on a single seismogram, for which the apparent depths were within 30 km of 410 and 660 km (±50 km for the P-to-SV converted waves). Note the consistent correlation between 410- and 660-km amplitudes.

significantly different for the P multiples compared with the S multiples. In addition, $Ss520s$ arrives after $Ss410s$, while $S520S$ arrives before $S410S$.

4. The amplitudes of the 520-km discontinuity phases are much larger than the expected amplitudes of the sidelobes of the 410-km phases. The positive sidelobes of the reference phases are only 5–15% of the amplitude of the main pulse, whereas the observed amplitudes of the 520-km discontinuity phases are 35–60% of the 410-km amplitudes.

5. The pulse shapes of waves which travel through the crust will change slightly (mainly as a result of the interface at the Moho). However, 520-km discontinuity phases are seen in both the S multiples (for which the discontinuity phases contain two extra crustal transits) and in the SS precursors (for which the reference phase contains two extra crustal transits), suggesting that this effect cannot have caused the 520-km phases.

6. Long-period synthetic seismograms computed for PREM

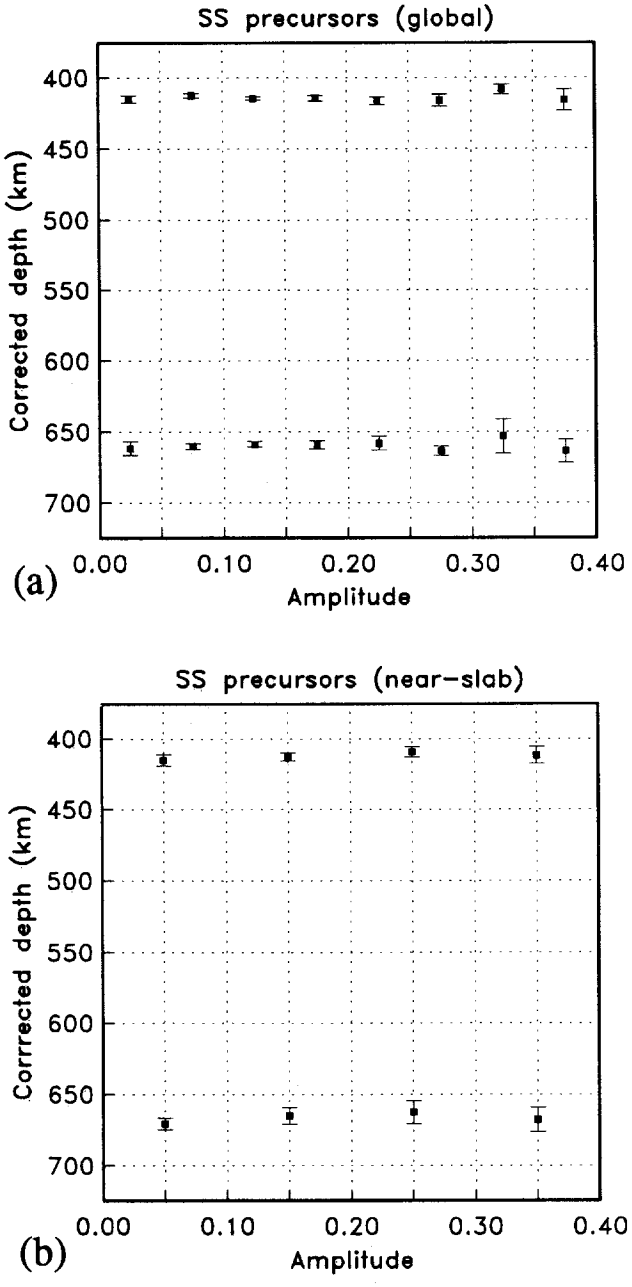

Fig. 25. Depths to the 410- and 660-km discontinuities versus SS precursor amplitudes, for (*a*) the global SS data set and (*b*) the northwest Pacific events. Note the consistency in the discontinuity depths over large ranges of precursor amplitudes.

[*Shearer and Masters*, 1990] do not show any evidence for waveforms which could be mistaken for $Ss520s$ or $S520S$. Since PREM contains discontinuities at 400 and 670 km, but not 520 km, the lack of 520-km phases in these synthetics indicates that the observed 520-km phases are real.

During the 1970s a number of studies found evidence for either a discontinuity or a kink in the velocity depth profile at or near 520 km. These analyses included short-period precursors to the phase $P'P'$ [*Whitcomb and Anderson*, 1970], P wave slowness data from arrays [*Simpson et al.*, 1974; *Fukao*, 1977], P wave refraction data [*Helmberger and Wiggins*, 1971; *Wiggins and Helmberger*, 1973; *Hales et al.*, 1980], S wave refraction data [*Helmberger and Engen*, 1974], and higher-mode Rayleigh waves [*Nolet*, 1977]. However, models based on more recent refraction studies have not included structure near 520 km [e.g., *Grand and Helmberger*, 1984*a*,*b*; *Walck*, 1984; *Bowman and Kennett*, 1990], and recent observations of upper mantle discontinuity phases have not identified 520-km phases [e.g., *Paulssen*, 1988; *Nakanishi*, 1989; *Davis et al.*, 1989]. A notable exception is the ScS reverberation study of *Revenaugh and Jordan* [1991*a*], who found evidence for minor discontinuities at 520, 710, and 900 km, in addition to the major discontinuities at 410 and 660 km. The evidence for the 520-km discontinuity is most persuasive in long-period data, where at least four different types of 520-km discontinuity phases have now been identified ($Pp520p$, $Ss520s$, $S520S$, and the ScS reflections seen by Revenaugh and Jordan). Evidence for $S520S$ can be found in SS precursor data for different tectonic regions with good agreement in the apparent discontinuity depths, suggesting that the 520-km discontinuity is a globally coherent feature.

Amplitude ratios from the waveform stacks indicate that the impedance contrast (for both P and S waves) at 520 km is $45 \pm 15\%$ of the change at 410 km. Assuming an 8–12% change in impedance at 410-km (PREM is 8%), this implies that the impedance jump at 520 km is between 2.4 and 7.2%. The partitioning of this impedance change into velocity and density can vary widely for different phase changes [e.g., *Liebermann*, 1979]. Assuming that $\partial \ln v / \partial \ln \rho$ is between 1 and 2, then the velocity jump at 520 km is between 1.2% and 4.8%. The fact that the 520-km discontinuity is not routinely observed in P and S wave refraction studies [e.g., *Jones and Helmberger*, 1990; *Cummins et al.*, 1991] argues for the lower side of this range.

Long-period data cannot distinguish between a sharp discontinuity or a region of enhanced velocity gradient. Long-period shear waves (~25 s) have a wavelength λ of about 125 km in the transition zone. The near-vertical reflection coefficient for a gradient region falls off rapidly when the thickness of the region exceeds $\lambda/5$ [e.g., *Richards*, 1972], implying that the impedance changes discussed above occur within a gradient region less than 25 km thick. *Cummins et al.* [1991] recently suggested that a 50-km transition might explain why short-period refraction data do not indicate a discontinuity at 520 km, while 520-km reflections are seen at long periods. The data presented here do not exclude the possibility of a 50-km-thick gradient region, but the impedance contrasts required in this case would be at least a factor of 2 larger than those for a sharper discontinuity. There is also some evidence for a 520-km reflector from quarry blast explosions (*Hoffman et al.* [1961] noted a reflector at a two-way vertical P travel time of 126.8 s, corresponding to a PREM depth of 538 km) and short-period precursors to the phase $P'P'$ [*Whitcomb and Anderson*, 1970]. If these observations do represent reflections of high-frequency energy off a 520-km discontinuity, then at least in some locations the discontinuity must be relatively sharp (less than ~4 km thick), just as other short-period $P'P'$ precursors imply a locally sharp 660-km discontinuity [*Richards*, 1972; *Lees et al.*, 1983].

Comparison With Mineral Physics Results

High-pressure experiments in mineral physics suggest that the 410-km discontinuity is caused mostly by the phase change between α- and β-olivine [e.g., *Bernal*, 1936; *Ringwood*, 1975; *Weidner and Ito*, 1987], and the 660-km discontinuity is mainly due to the transformation γ-spinel → perovskite +

magnesiowüstite [e.g., *Liu*, 1976, 1979; *Jackson*, 1983; *Ito et al.*, 1984], although some researchers argue that chemical changes also occur at these discontinuities [*Anderson and Bass*, 1986; *Duffy and Anderson*, 1989]. These phase changes will occur at different depths in the mantle depending upon both composition and temperature. The pressure dependence on temperature (Clapeyron slope $\gamma = dP/dT$) is of particular interest because it relates variations in discontinuity topography to variations in mantle temperature. Measured values of the Clapeyron slope for the olivine → β-phase change near 410 km include $\gamma = 3.5$ MPa/°K [*Suito*, 1977], $\gamma = 2.5$ MPa/°K [*Ashida et al.*, 1987], $\gamma = 2.5$ MPa/°K [*Katsura and Ito*, 1989], and $\gamma = 1.5 \pm 0.8$ MPa/°K [*Akaogi et al.*, 1989]. Values obtained for the γ-spinel → perovskite + magnesiowüstite phase change near 660 km include $\gamma = -2.0$ MPa/°K [*Ito and Yamada*, 1982], $\gamma = -2.8$ MPa/°K [*Ito and Takahashi*, 1989], and $\gamma = -4.0 \pm 2.0$ MPa/°K [*Ito et al.*, 1990]. For comparison with these measurements, a computer simulation of lattice properties [*Price et al.*, 1989] predicted $\gamma = 1.8$ MPa/°K for olivine → β-phase and $\gamma = -3.3$ MPa/°K for γ-spinel → perovskite + magnesiowüstite.

The positive values of γ for the 410-km phase change indicate an exothermic reaction in which the discontinuity moves toward deeper depths at higher temperatures. In contrast, the negative Clapeyron slope for the 660-km phase change implies an endothermic reaction in which the discontinuity moves upward at higher temperatures. The reaction ilmenite → perovskite may also be important near 660 km [e.g., *Ito and Yamada*, 1982]. Negative Clapeyron slopes have been measured for this reaction as well, with values including $\gamma = -2.5$ MPa/°K [*Ito and Takahashi*, 1989], and $\gamma = -5.0 \pm 2.0$ MPa/°K [*Ito et al.*, 1990]. At transition zone pressures, a Clapeyron slope of +2 MPa/°K implies that every 100°K increase in mantle temperature will cause roughly a 6 km increase in depth to the 410-km discontinuity and a 5 km increase in depth to the 660-km discontinuity. For uniform temperature anomalies in the transition zone, the opposite sign of the Clapeyron slopes for the 410- and 660-km phase changes implies that the discontinuities should move in opposing directions. In this case the 410- and 660-km depths would be anticorrelated (contrary to most of the results shown here, but see discussion below). Although early measurements suggested that $|\gamma_{410}| > |\gamma_{660}|$, the most recent studies imply the opposite relationship, i.e., that $|\gamma_{660}| > |\gamma_{410}|$. The *Akaogi et al.* [1989] and *Ito et al.* [1990] results and the *Price et al.* [1989] modeling suggest that the magnitude of the Clapeyron slope near 660 km is 2–3 times the size of the slope at 410 km. These results are consistent with the greater variability in apparent depths to the 660-km discontinuity seen in the cross-correlation analyses discussed above.

The most obvious potential phase change responsible for the 520-km discontinuity is β-phase → spinel [e.g., *Whitcomb and Anderson*, 1970; *Ringwood*, 1975]. However, high-pressure experiments [*Weidner et al.*, 1984] indicate that the change in velocity associated with this phase change occurs gradually and is too small to explain the observations, which require an impedance change of at least 2.4% in a gradient region less than 25 km thick. If an olivine phase change alone is insufficient, there is no shortage of possible phase changes in other minerals, including pyroxene, garnet, and diopside (see discussion in *Ringwood* [1975] and *Revenaugh and Jordan* [1991*a*]).

DISCUSSION

Absolute Discontinuity Depths

Obtaining accurate estimates of the depths of upper mantle discontinuities is important, since these depths can be used in conjunction with the results of mineral physics experiments to measure the temperatures in the upper mantle [e.g., *Ito and Katsura*, 1989]. Global averages of the apparent depths to the upper mantle discontinuities are in reasonably good agreement (see Table 1). For the WM.SS-S corrected data, apparent depths to the 410-km discontinuity are 414 km for the P-to-SV conversions, 419 km for the P multiples, 417 km for the SH multiples, and 415 km for the SS precursors. Depths to the 520-km discontinuity are 526 km for the P multiples, 519 km for the SH multiples, and 519 km for the SS precursors. Depths to the 660-km discontinuity are 669 km for the P-to-SV conversions, 663 km for the P multiples, 653 km for the SH multiples, and 659 km for the SS precursors. Some of the disagreement in the depths from the P-to-SV conversions and P multiples is probably due to inadequacies in scaling the WM.SS-S shear wave model to account for P velocity variations. The SS precursor data should give the best discontinuity depth estimates, since the WM.SS-S model is most appropriate for these data. In addition, the wide distribution of the SS bouncepoints should result in a better estimate of the true global average depths than is possible for the other phases.

Thus the most reliable values for average discontinuity depths are given by the SS precursor values of 415, 519, and 659 km. The small standard errors listed in Table 1 probably exaggerate the precision of these numbers, since they do not take into account the possibility of systematic errors in the velocity model or uneven global sampling. A conservative estimate of the maximum likely error is ±5 km. For comparison, PREM contains discontinuities at 400 and 670 km, and the means and standard deviations of discontinuity depths in recent upper mantle velocity models, as summarized by *Nolet and Wortel* [1989], are 401 ± 11 km and 662 ± 6 km. The estimated discontinuity depths from the SS precursors agree remarkably well with the values of 414, 524, and 660 km recently obtained by *Revenaugh and Jordan* [1991*a*] from analysis of ScS reverberation data. There is also close agreement with the estimates of 417 and 660 km obtained by *Kind and Vinnik* [1988] through analysis of P-to-SV converted phases recorded at the Gräfenberg array.

The 410-km Versus 660-km depths

The greater variability in the 660-km depths is a common feature throughout the analyses in this paper, including the broader 660-km peaks seen in the global cross-correlation counts from four different discontinuity phases (Figure 12), the broader 660-km peaks for SS precursors from each of five different tectonic regions (Figure 16), and the greater variations in the mean apparent depths to the 660-km discontinuity within these regions (Figure 17) and in localized regions near a subducting slab (Figure 21). Only the depths obtained for individual seismic stations from P-to-SV converted phases do not show this feature (Figure 14), but these estimated depths have substantially larger error bars than those of the other plots, indicating that noise may have swamped the signal.

Another feature of many of these plots is a weak correlation between the 410- and 660-km depths (e.g., Figures 17 and 21). This contrasts with the negative correlation which would be predicted by the Clapeyron slopes discussed above, assuming a uniform temperature anomaly in the transition zone. The most likely explanation for this positive correlation is lateral heterogeneity above the transition zone, which will tend to bias both the 410- and 660-km discontinuities in the same direction. The corrections for the WM.SS-S model appear to have removed this effect in the case of the regionalized values obtained from the SS precursors (Figure 17), with the WM.SS-S corrected estimates exhibiting a negative correlation as predicted by the Clapeyron slopes. However, in the case of the near-slab SS precursor averages (Figure 21), a positive correlation is seen even after the WM.SS-S corrections are applied. This is a more severe test of the resolution of the WM.SS-S model than the regionalized averages shown in Figure 17.

The uncorrected plots of 410- versus 660-km discontinuity depths may provide information regarding the relationship between heterogeneity in the shallow mantle and temperature variations in the transition zone. In particular, the data appear to be incompatible with vertically coherent temperature variations throughout the upper mantle. If temperatures above the 410-km discontinuity were positively correlated with variations within the transition zone, then a cold temperature anomaly would have the effect of decreasing the 410-km discontinuity depth and increasing the 660-km discontinuity depth (due to the Clapeyron slopes), while decreasing both the 410- and 660-km apparent depths (due to faster travel times through the uppermost mantle). The net result would be an exaggeration of the depth variations to the 410-km discontinuity, a reduction in the depth variations to the 660-km discontinuity, and a negative correlation between apparent depths to the 410- and 660-km discontinuities. This is exactly opposite to what is observed (Figures 17 and 21), implying that temperature variations within the transition zone must be uncorrelated or anticorrelated with variations above the 410-km discontinuity. This conclusion is in contrast to some seismic models of upper mantle structure; heterogeneity above and below the 410-km discontinuity is weakly correlated in model M84C [*Woodhouse and Dziewonski*, 1984] and strongly correlated in MDLSH [*Tanimoto*, 1990]. However, the depth resolution of these models is limited, and it is unclear if these correlations are required by the data or are simply a result of the inversion procedure.

The interpretation of these results depends strongly upon the assumed values for the Clapeyron slopes. If $|\gamma_{410}|$ and $|\gamma_{660}|$ are actually about equal in size, the observed greater variability in 660-km discontinuity depths implies that the lateral temperature variations at 660-km depth are greater than the variations at 410 km, or significant heterogeneity must be present in the transition zone which has not been accounted for by the WM.SS-S times. However, for the WM.SS-S corrected depths transition zone heterogeneity would increase the variability in the 410-km depths rather than the 660-km depths. *Revenaugh and Jordan* [1991*a*] show that for reasonable values of the dependence of shear velocity on temperature ($\partial v_s/\partial T$) and the Clapeyron slopes γ_{410} and γ_{660}, reflected phase travel time differences due to vertically coherent temperature anomalies in the transition zone depend much more strongly on discontinuity displacement than on transition zone velocity changes. Thus it appears unlikely that the observed greater variability in 660-km discontinuity depths (seen in both the raw and WM.SS-S corrected depths) is due to transition zone heterogeneity. Another possibility is that a small discontinuity of fluctuating brightness or depth exists near the 660-km discontinuity, biasing apparent depths to the 660-km discontinuity by variable amounts. This model seems less straightforward than simply assuming that $|\gamma_{660}| > |\gamma_{410}|$, but clearly there is no substitute for independent and reliable measurements of the Clapeyron slopes from mineral physics experiments.

After using the WM.SS-S model to correct for the effects of lateral heterogeneity, mean apparent depths to the 410- and 660-km discontinuities exhibit only small variations between different tectonic regions (Table 3). 410-km discontinuity depths show a maximum variation of 5 km, while 660-km depths show up to a 10-km variation. Assuming the *Akaogi et al.* [1989] and *Ito et al.* [1990] values for the Clapeyron slopes (γ_{410} = 1.5 MPa/°K $\approx$ 0.05 km/°K, γ_{660} = −4.0 MPa/°K $\approx$ 0.10 km/°K), these numbers imply that regional temperature variations at both 410 and 660 km do not exceed about 100°. There is a suggestion from the 410-km values that orogenic regions may be somewhat colder at depth than the global average, while the 660-km values indicate that orogenic regions, platforms, and shields may be colder at depth than the global average. Care should be taken in interpreting these regionalization results since the tectonic regions may not be optimal for resolving lateral variations in discontinuity depths. Greater differences in discontinuity depths may well be present if these variations are averaged out within each tectonic region. Nevertheless, the regionalization results do limit the size of any consistent variation in discontinuity depths between different regions and, by using Clapeyron slope data, also imply limits on regional temperature variations. For example, these data suggest that average continental versus oceanic temperature profiles do not vary by more than 100° at 410 km.

Evidence for larger variations in discontinuity topography is provided by the P-to-SV results for individual stations and the SS precursor data from the northwest Pacific. Apparent depths to the 410- and 660-km discontinuities obtained for individual seismic stations (see Table 2 and Figure 14) exhibit differences of up to 40 km, although much of this variability can be attributed to the large error bars associated with many depth estimates. Assuming γ_{410} = 1.5 MPa/°K and γ_{660} = −4.0 MPa/°K, this limits lateral temperature variations at 410 km to less than 850° and variations at 660 km to less than 400°, at least beneath the continents where most of the seismic stations are located. Note that discontinuity depth and temperature variations of this size are not required by the data; given the large error bars associated with individual station estimates, it cannot be said with certainty that any depth variations are present beneath the stations.

Discontinuity Topography Near Subducting Slabs

The SS precursor results from the northwest Pacific suggest the presence of a broad 20-km depression in the 660-km discontinuity near the point where the subducting slabs intersect the discontinuity (Figure 20). This feature appears to extend about 1000 km to the west (backarc) side of the slab intersection point and about 500 km to the east, although the lateral resolution of the long-period data is very limited.

Assuming $\gamma_{660} = -4.0$ MPa/°K, a 20-km depression in the 660-km discontinuity implies that temperatures are about 200° cooler in this region. Thermal models of subducting slabs which slice cleanly through the 660-km discontinuity [e.g., *Schubert et al.*, 1975; *Creager and Jordan*, 1986] generally contain temperatures within the subducting slab which are 800°–1000° cooler than the surrounding mantle, with this anomaly confined to a 100- to 200-km-wide zone within the slab. A 1000° temperature anomaly should cause a 100 km depression in the 660-km discontinuity, assuming $\gamma_{660} = -4.0$ MPa/°K and ignoring dynamic effects. Since this feature would only be present within the slab itself, it would not be resolvable by the long-period SS precursor data considered here. However, some evidence against the occurrence of such large perturbations to the 660-km discontinuity within subducting slabs, at least in one area, is provided by the short-period S-to-P conversions from deep focus events in Tonga [*Barley et al.*, 1982; *Bock and Ha*, 1984; *Richards and Wicks*, 1990]. Richards and Wicks' results indicate that the 660-km discontinuity may be depressed by about 20–30 km (but no more than 50 km) within or very close to the subducting slab at Tonga.

The hint in Figure 20 of a similar depression in the 410-km discontinuity is puzzling. While in some cases the 410-km discontinuity can be depressed in a fast-subducting slab despite its positive Clapeyron slope [*Sung and Burns*, 1976*a*,*b*; *Poirier*, 1981], this effect would be confined to the immediate vicinity of the slab rather than appearing as a broad regional feature. If this depression is real, the implication is that temperatures near 410 km are elevated in a 5°–15° region in the vicinity of the subducting slab. Alternatively, this apparent depression may be an artifact resulting from inadequate corrections for lateral heterogeneity above the 410-km discontinuity (i.e., a slow region in the uppermost mantle) or inappropriate corrections resulting from transition zone heterogeneity (i.e., a fast region in the transition zone). The latter explanation seems more likely since the WM.SS-S model has fairly good coverage in this area and the apparent depression in the 410-km discontinuity is clearer in the WM.SS-S corrected depths than in the raw depths.

The existence of a broad 1000–1500-km-wide region of moderately reduced temperatures in the vicinity of subducting slabs at 660 km is not predicted by thermal models of slabs which slice cleanly through the discontinuity. Rather, it supports models in which the subducting slab spreads out near 660 km. Such models would include the gravitationally trapped megalith hypothesis [*Ringwood*, 1982; *Ringwood and Irifune*, 1988] and some of the numerical simulations of subducting slabs encountering a viscosity contrast performed by *Gurnis and Hager* [1988]. These models predict a relatively broad region of moderately cooler temperatures on the backarc side of the slab intersection point. A specific megalith model described by Ringwood and Irfune predicts a temperature anomaly of 300° within a megalith trapped on the 660-km discontinuity, in rough agreement with the SS precursor observations described above. An simple alternative to these models of slab entrapment would be to hypothesize that the surrounding mantle may have been cooled in this region by long-standing subduction. However, this model does not directly explain why the thermal anomaly should be displaced toward the backarc side.

It is interesting to note that larger values of $|\gamma_{660}|$ are associated with increasing resistance to slab penetration. *Christensen and Yuen* [1984] computed that a negative Clapeyron slope of $\gamma_{660} = -6$ MPa/°K would impede whole mantle convection, even with no compositional density change at 660 km. Recent modeling results of *Machetel and Weber* [1991] suggest that a Clapeyron slope of $\gamma_{660} = -4$ MPa/°K will result in layered convection, with a mixture of whole-mantle and layered convection occurring for $\gamma_{660} = -2$ MPa/°K. If a compositional discontinuity is present near 660 km, modeling results have shown that it should be displaced several hundred kilometers or more by subducting slabs [e.g., *Hagar and Raefsky*, 1981; *Christensen and Yuen*, 1984]. The fact that such displacements are not observed argues against the possibility of a purely chemical change at 660 km, as noted by *Richards and Wicks* [1990] and *Revenaugh and Jordan* [1991*a*]. However, a small chemical change in density at or near the 660-km phase change cannot be ruled out, since even large perturbations in its depth might not be seen in seismic observations.

Although the apparent discontinuity depths shown in Figure 20 are suggestive, some caution is warranted in their interpretation. Many of the data points on the backarc side of the slab intersection are near the bend between the Japan and Kurile-Kamchatka subduction zones where the slab structure is poorly constrained and possibly anomalous. The apparent depths to the 410-km discontinuity exhibit variations which may indicate the presence of uncorrected upper mantle heterogeneity. Long-period SS precursors have limited resolution so the boundaries of possible discontinuity topography are not well defined. However, despite these uncertainties it is clear that SS precursor data have great potential for mapping discontinuity topography, and future more detailed analyses can only improve on the results shown here. Regional and global maps of discontinuity topography would be extremely useful in constraining models of mantle dynamics, particularly if more reliable estimates of the Clapeyron slopes could be obtained.

Other Discontinuities?

In addition to the well-established major discontinuities near 410 and 660 km, there is some seismic evidence for additional upper mantle discontinuities. Indeed, it would be hard to find a depth in the upper mantle for which a discontinuity has not at some time been proposed. As discussed above, long-period reflected phases support earlier evidence for a 520-km discontinuity. Another discontinuity which has often been proposed occurs near 220 km [e.g., *Lehmann*, 1959; *Hales et al.*, 1980; *Drummond et al.*, 1982; *Leven et al.*, 1981], and it has been suggested that a 220-km discontinuity is an important global feature which occurs beneath both oceans and continents [*Anderson*, 1979]. PREM contains a 220-km discontinuity which is comparable in size to discontinuities at 400 and 670 km. Proposed explanations for a 220-km discontinuity have included a composition change between garnet lherzolite and eclogite [*Anderson*, 1979] and the existence of an anisotropic layer caused by preferred alignment of olivine crystals [*Leven et al.*, 1981].

No evidence is found for a 220-km discontinuity in any of the stacked images (Plates 1–5). The global cross-correlation plots also do not show a 220-km peak (Figure 12), nor do the SS precursor plots for individual tectonic regions (Figure 16). This is consistent with many upper mantle velocity models [e.g., *Walck*, 1984; *Grand and Helmberger*, 1984*a*,*b*],

which do not have significant structure at this depth. Other models, however, do contain large discontinuities at 220 km, and in some areas there is strong evidence for structure near this depth [*Hales et al.*, 1980; *Drummond et al.*, 1982; *Leven*, 1985]. PREM contains P and S wave impedance contrasts at 220 km that are roughly comparable in size to the contrasts at 400 km. Given that P and S wave phases from the 400-km discontinuity are easily visible in the stacks, a 220-km discontinuity of comparable size should also be seen. The absence of visible 220-km discontinuity phases indicates that the impedance contrast at 220 km must be much less than PREM or that its depth is so variable that no coherent reflections are formed. The regionalization results (Figure 16) suggest that a significant 220-km discontinuity is not a general feature of any tectonic region. This result largely agrees with the ScS reverberation observations of *Revenaugh and Jordan* [1991*b*], who found no evidence for a 220-km discontinuity for most of their paths. Where a 220-km reflector was observed in the ScS data (e.g., beneath northern Australia), its depth was so variable (up to 100 km) that it would be difficult to image in the global stacks of 25-s data considered in this paper.

The stacks and cross-correlation plots do not indicate the existence of any discontinuities other than those at 410, 520, and 660 km. There are hints of additional discontinuities on some of the plots, but these features are not consistent between plots so it is hard to have any confidence in their existence. However, weak discontinuties could be missed, especially if they were close in depth to a major discontinuity since these long-period images can only resolve reflectors if they are well-separated in time from other reflectors. In particular, near-surface interfaces such as the Moho or the 80-km discontinuity observed with waveform modeling by *Revenaugh and Jordan* [1991*b*] cannot be seen.

CONCLUSIONS

The main conclusions of this paper may be summarized as follows:

1. Long-period GDSN data are sufficiently coherent that simple stacking techniques using a reference phase can be used to image minor seismic phases resulting from reflections and conversions at upper mantle discontinuities. Particularly well resolved are the P-to-SV converted phases from discontinuities beneath the receivers, P and S wave multiples off the top of the discontinuities, and precursors to SS resulting from bottomside discontinuity reflections. These phases can be clearly seen both in the waveform stacks and in cross-correlation analysis of individual seismograms.

2. These images indicate discontinuities near 410, 520, and 660 km. The 520-km discontinuity is seen for three different phase types and in every tectonic region, supporting earlier studies which indicated an interface at this depth. No evidence is found for a 220-km discontinuity, although phases associated with such a discontinuity should be visible if the 220-km discontinuity were a significant global feature.

3. Average apparent depths to the discontinuities for the different phases agree to within ± 3 km for the 410-km discontinuity, to within ± 4 km for the 520-km discontinuity, and to within ± 8 km for the 660-km discontinuity. The best global averages are obtained from the SS precursor data which indicate discontinuities at 415, 519, and 659 km.

4. The P-to-SV converted phases can be used to estimate discontinuity depths beneath over 35 individual seismic stations. These depths show differences of up to ± 20 km, although the actual variations are probably less because of relatively large errors associated with individual estimates.

5. Apparent depths to the 660-km discontinuity consistently exhibit greater variability than depths to the 410-km discontinuity, supporting recent laboratory results which indicate that the Clapeyron slope for the 660-km discontinuity is significantly larger in magnitude than the slope for the 410-km discontinuity.

6. Precursors to SS (seen between 110° and 180° range) are particularly useful for mapping possible lateral variations in discontinuity depths since each arrival can be associated with a single underside reflection point. Apparent discontinuity depths computed from SS precursors for different tectonic regions agree to within about ± 5 km, implying that there are no large temperature variations in the transition zone between different regions.

7. SS precursors from subduction zones in the northwest Pacific suggest the presence of a broad 1000–1500-km-wide region near the slab in which the 660-km discontinuity is depressed by about 20 km. These results are preliminary, but the existence of such an anomaly would argue against models of clean slab penetration through the 660-km discontinuity and favor models in which the thermal and/or dynamic effects of the descending slab spread out near the discontinuity.

8. Measuring absolute amplitudes for these phases is difficult due to the large corrections required to compensate for the effects of incoherent stacking. Relative amplitude analysis suggests that the P and S wave impedance changes at 410 km are about 0.8–1.1 times the size of the changes at 660 km and that the contrasts at 520 km are between 0.3 and 0.6 of the change at 410 km. The amplitudes of the 410- and 660-km discontinuity phases are correlated on individual seismograms, probably due to similar focusing effects from heterogeneity along the ray paths. Amplitudes of discontinuity phases do not appear to be related to discontinuity depth.

Upper mantle discontinuity phases can be seen relatively easily in long-period data, indicating that detailed mapping of discontinuity topography is a real possibility, especially as the global station coverage continues to improve. The integration of these results with travel time and other data sets will lead to the formulation of three-dimensional velocity models which include boundary perturbations. Such models will provide invaluable constraints for modeling temperature and flow in the mantle.

Acknowledgments. Guy Masters offered advice and subroutines for using the GDSN data, and computed normal-mode synthetic seismograms for comparison purposes. Bob Woodward provided advice and code for using the SS-S residual data set. Justin Revenaugh and Tom Jordan sent preprints of their ScS reverberation work, and Justin Revenaugh provided a thorough and helpful review of this paper. I am also grateful to the National Earthquake Information Center and the U.S. Geological Survey for making the GDSN data available on CD-ROM. This research was supported by National Science Foundation grants EAR-89-15821 and EAR-90-04378 and funding from the Cecil and Ida Green Foundation.

REFERENCES

Adams, R.D., Reflections from discontinuities beneath Antarctica, *Bull. Seismol. Soc. Am.*, *61*, 1441–1451, 1971.

Akaogi, M., E. Ito, and A. Navrotsky, Olivine-modified spinel-spinel transitions in the system Mg_2SiO_4 – Fe_2SiO_4: Calorimetric measurements, thermodynamic calculation, and geophysical application, *J. Geophys. Res.*, *94*, 15,671–15,685, 1989.

Ammon, C.J., G.E. Randall, and G. Zandt, On the nonuniqueness of

receiver function inversions, *J. Geophys. Res.*, *95*, 15,303–15,318, 1990.

Anderson, D.L., The deep structure of continents, *J. Geophys. Res.*, *84*, 7555–7560, 1979.

Anderson, D.L., and J.D. Bass, Transition region of the Earth's upper mantle, *Nature*, *320*, 321–328, 1986.

Ashida, T., S. Kume, and E. Ito, Thermodynamic aspects of phase boundary among α-, β-, and γ-Mg_2SiO_4, in *High-Pressure Research in Mineral Physics*, edited by M.H. Manghnani and Y. Syono, pp. 269–274, Terra Scientific, Tokyo, 1987.

Baag, C.-E., and C.A. Langston, Shear coupled PL, *Geophys. J. R. Astron. Soc.*, *80*, 363–386, 1985.

Barley, B.J., J.A. Hudson, and A. Douglas, S to P scattering at the 650 km discontinuity, *Geophys. J. R. Astron. Soc.*, *69*, 159–172, 1982.

Baumgardt, D.R., and S.S. Alexander, Structure of the mantle beneath Montana LASA from analysis of long-period mode-converted phases, *Bull. Seismol. Soc. Am.*, *74*, 1683–1702, 1984.

Bernal, J.D., Discussion, *Observatory*, *59*, 268, 1936.

Bock, G., *Sp* phases from the Australian upper mantle, *Geophys. J.*, *94*, 73–81, 1988.

Bock, G., and J. Ha, Short-period S–P conversion in the mantle at a depth near 700 km, *Geophys. J. R. Astron. Soc.*, *77*, 593–615, 1984.

Bolt, B.A., PdP and $PKiKP$ waves and diffracted PcP waves, *Geophys. J. R. Astron. Soc.*, *20*, 367–382, 1970.

Bowman, J.R., and B.L.N. Kennett, An investigation of the upper mantle beneath northwestern Australia using a hybrid seismograph array, *Geophys. J. Int.*, *101*, 411–424, 1990.

Burbach, G.V., and C. Frohlich, Intermediate and deep seismicity and lateral structure of subducted lithosphere in the circum-Pacific region, *Rev. Geophys.*, *24*, 833–874, 1986.

Burdick, L.J., A comparison of upper mantle structure beneath North America and Europe, *J. Geophys. Res.*, *86*, 5926–5936, 1981.

Burdick, L.J., and D.V. Helmberger, The upper mantle P velocity structure of the western United States, *J. Geophys. Res.*, *83*, 1699–1712, 1978.

Burdick, L.J., and C.A. Langston, Modeling crustal structure through the use of converted phases in teleseismic body-waveforms, *Bull. Seismol. Soc. Am.*, *67*, 677–691, 1977.

Byerly, P., The Montana earthquake of June 28, 1925, *Bull. Seismol. Soc. Am.*, *16*, 209–265, 1926.

Choy, G.L., and P.G. Richards, Pulse distortion and Hilbert transformation in multiply reflected and refracted body waves, *Bull. Seismol. Soc. Am.*, *65*, 55–70, 1975.

Christensen, U.R., and D.A. Yuen, The interaction of a subducting lithospheric slab with a chemical or phase boundary, *J. Geophys. Res.*, *89*, 4389–4402, 1984.

Creager, K.C., and T.H. Jordan, Slab penetration into the lower mantle beneath the Mariana and other island arcs of the northeast Pacific, *J. Geophys. Res.*, *91*, 3573–3589, 1986.

Cummins, P.R., B.L.N. Kennett, J.R. Bowman, and M.G. Bostok, The 530 km discontinuity?, *Bull. Seismol. Soc. Am.*, in press, 1991.

Davies, D., E.J. Kelly, and J.R. Filson, Vespa process for analysis of seismic signals, *Nature*, *232*, 8–13, 1971.

Davis, J.P., R. Kind, and I.S. Sacks, Precursors to $P'P'$ re-examined using broad-band data, *Geophys. J. Int.*, *99*, 595–604, 1989.

Drummond, B.J., K.J. Muirhead, and A.L. Hales, Evidence for a seismic discontinuity near 200 km depth under a continental margin, *Geophys. J. R. Astron. Soc.*, *70*, 67–77, 1982.

Duffy, T.S., and D.L. Anderson, Seismic velocities in mantle minerals and the mineralogy of the upper mantle, *J. Geophys. Res.*, *94*, 1895–1912, 1989.

Dziewonski, A.M., and D.L. Anderson, Preliminary reference Earth model, *Phys. Earth Planet. Inter.*, *25*, 297–356, 1981.

Efron, B., and R. Tibshirani, Bootstrap methods for standard errors, confidence intervals, and other measures of statistical accuracy, *Stat. Sci.*, *1*, 54–77, 1986.

Engdahl, E.R., and E.A. Flinn, Seismic waves reflected from discontinuities within Earth's upper mantle, *Science*, *163*, 177–179, 1969.

Faber, S., and G. Müller, *Sp* phases from the transition zone between the upper and lower mantle, *Bull. Seismol. Soc. Am.*, *70*, 487–508, 1980.

Faber, S., and G. Müller, Converted phases from the mantle transition zone observed at European stations, *J. Geophys.*, *54*, 183–194, 1984.

Frazer, N.L., Synthesis of shear coupled PL, Ph.D. thesis, Princeton Univ., Princeton, N. J., 1977.

Fukao, Y., Upper mantle P structure on the ocean side of the Japan-Kurile arc, *Geophys. J. R. Astron. Soc.*, *50*, 621–642, 1977.

Given, J.W., and D.V. Helmberger, Upper mantle structure of northwestern Eurasia, *J. Geophys. Res.*, *85*, 7183–7194, 1980.

Grand, S.P., and D.V. Helmberger, Upper mantle shear structure of North America, *Geophys. J. R. Astron. Soc.*, *76*, 399–438, 1984*a*.

Grand, S.P., and D.V. Helmberger, Upper mantle shear structure beneath the northwest Atlantic Ocean, *J. Geophys. Res.*, *89*, 11,465–11,475, 1984*b*.

Gurnis, M., and B.H. Hagar, Controls of the structure of subducted slabs, *Nature*, *335*, 317–321, 1988.

Gurrola, H., and B. Minster, Receiver responses at IRIS/IDA stations in the USSR, *Eos Trans. AGU*, *71*, 1450, 1990.

Gutowski, P.R., and E.R. Kanasewich, Velocity spectral evidence of upper mantle discontinuities, *Geophys. J. R. Astron. Soc.*, *36*, 21–32, 1974.

Hager, B.H., and A. Raefsky, Deformation of seismic discontinuities and the scale of mantle convection, *Eos Trans. AGU*, *62*, 1074, 1981.

Hales, A.L., K.J. Muirhead, and J.M.W. Rynn, A compressional velocity distribution for the upper mantle, *Tectonophysics*, *63*, 309–348, 1980.

Helmberger, D.V., and G.R. Engen, Upper mantle shear structure, *J. Geophys. Res.*, *79*, 4017–4028, 1974.

Helmberger, D.V., and R.A. Wiggins, Upper mantle structure of midwestern United States, *J. Geophys. Res.*, *76*, 3229–3245, 1971.

Hoffman, J.P., J.W. Berg, and K.L. Cook, Discontinuities in the Earth's upper mantle as indicated by reflected seismic energy, *Bull. Seismol. Soc. Am.*, *51*, 17–27, 1961.

Husebye, E., and R. Madariaga, The origins of precursors to core waves, *Bull. Seismol. Soc. Am.*, *60*, 939–952, 1970.

Husebye, E.S., R.A.W. Haddon, and D.W. King, Precursors to $P'P'$ and upper mantle discontinuities, *J. Geophys.*, *43*, 535–543, 1977.

Isacks, B., and P. Molnar, Distribution of stresses in the descending lithosphere from a global survey of focal-mechanism solutions of mantle earthquakes, *Rev. Geophys.*, *9*, 103–174, 1971.

Ito, E., and T. Katsura, A temperature profile of the mantle transition zone, *Geophys. Res. Lett.*, *16*, 425–428, 1989.

Ito, E., and E. Takahashi, Postspinel transformations in the system Mg_2SiO_4-Fe_2SiO_4 and some geophysical implications, *J. Geophys. Res.*, *94*, 10,637–10,646, 1989.

Ito, E., and H. Yamada, Stability relations of silicate spinels, ilmenites, and perovskites, in *High-Pressure Research in Mineral Physics*, edited by S. Akimoto and M.H. Manghnani, pp. 405–419, Center for Academic Publications, Tokyo, 1982.

Ito, E., E. Takahashi, and Y. Matsui, The mineralogy and chemistry of the lower mantle: An implication of the ultrahigh-pressure phase relations in the system MgO-FeO-SiO_2, *Phys. Earth Planet. Inter.*, *67*, 238–248, 1984.

Ito, E., M. Akaogi, L. Topor, and A. Navrotsky, Negative pressure-temperature slopes for reactions forming $MgSiO_3$ perovskite from calorimetry, *Science*, *249*, 1275–1278, 1990.

Jackson, I., Some geophysical constraints on the chemical composition of the Earth's lower mantle, *Earth Planet. Sci. Lett.*, *62*, 91–103, 1983.

Jeanloz, R., High pressure chemistry of the Earth's mantle and core. in *Mantle Convection: Plate Tectonics and Global Dynamics*, edited by W.R. Peltier, pp. 203–259, Gordon and Breach, New York, 1989.

Jeffreys, S.H., The structure of the earth down to the 20° discontinuity, *Mon. Not. R. Astron. Soc. Geophys. Suppl.*, *3*, 401–422, 1936.

Jones, L.E., and D.V. Helmberger, Modeling the 520 discontinuity: A detailed study of record sections from several small Mexican events, *Eos Trans. AGU*, *71*, 1472, 1990.

Jordan, T.H., Global tectonic regionalization for seismological data analysis, *Bull. Seismol. Soc. Am.*, *71*, 1131–1141, 1981.

Jordan, T.H., A.L. Lerner-Lam, and K.C. Creager, Seismic imaging of boundary layers and deep mantle convection, in *Mantle Convection: Plate Tectonics and Global Dynamics*, edited by W.R. Peltier, pp. 98–201, Gordon and Breach, New York, 1989.

Kampfmann, W., and G. Müller, PcP amplitude calculations for a core-mantle boundary with topography, *Geophys. Res. Lett.*, *16*, 653–656, 1989.

Katsura, T., and E. Ito, The system Mg_2SiO_4-Fe_2SiO_4 at high pressures and temperatures: Precise determination of stabilities of

olivine, modified spinel, and spinel, *J. Geophys. Res.*, *94*, 15,663–15,670, 1989.

Kind, R., G.L. Kosarev, L.I. Makeyeva, and L.P. Vinnik, Observations of laterally inhomogeneous anisotropy in the continental lithosphere, *Nature*, *318*, 358–361, 1985.

Kind, R., and L.P. Vinnik, The upper mantle discontinuities underneath the GRF array from *P*-to-*S* converted phases, *J. Geophys.*, *62*, 138–147, 1988.

King, D.W., and G. Calcagnile, *P* wave velocities in the upper mantle beneath Fennoscandia and western Russia, *Geophys. J. R. Astron. Soc.*, *46*, 407–432, 1976.

Kosarev, G.L., L.I. Makeyeva, and L.P. Vinnik, Anisotropy of the mantle inferred from observations of *P* to *S* converted waves, *Geophys. J. R. Astron. Soc.*, *76*, 209–220, 1984.

Lees, A.C., M.S.T. Bukowinski, and R. Jeanloz, Reflection properties of phase transition and compositional change models of the 670-km discontinuity, *J. Geophys. Res.*, *88*, 8145–8159, 1983.

LeFevre, L.V., and D.V. Helmberger, Upper mantle *P* velocity structure of the Canadian shield, *J. Geophys. Res.*, *94*, 17749–17765, 1989.

Lehmann, I., Velocities of longitudinal waves in the upper part of the Earth's mantle, *Ann. Geophys.*, *15*, 93–118, 1959.

Liebermann, R.C., Elasticity of the mantle, in *The Earth: Its Origin, Structure and Evolution*, edited by M.W. McElhinny, pp. 203–226, Academic, San Diego, Calif., 1979.

Leven, J.H., The application of synthetic seismograms to the interpretation of the upper mantle *P*-wave velocity structure in northern Australia, *Phys. Earth Planet. Inter.*, *38*, 9–27, 1985.

Leven, J.H., I. Jackson, and A.E. Ringwood, Upper mantle seismic anisotropy and lithospheric decoupling, *Nature*, *289*, 234–239, 1981.

Liu, L.-G., The post-spinel phase of forsterite, *Nature*, *262*, 770–772, 1976.

Liu, L.-G., Phase transformations and the constitution of the deep mantle, in *The Earth: Its Origin, Structure and Evolution*, edited by M.W. McElhinny, pp. 177–202, Academic, San Diego, Calif., 1979.

Machetel, P., and P. Weber, Intermittent layered convection in a model with an endothermic phase change at 670 km, *Nature*, *350*, 55–57, 1991.

Masters, G. and H. Bolton, Long-period absolute *S* times and lower-mantle structure, *Eos Trans. AGU*, *71*, 1464–1465, 1990.

Nakanishi, I., Reflections of *P'P'* from upper mantle discontinuities beneath the Mid-Atlantic Ridge, *Geophys. J.*, *93*, 335–346, 1988.

Nolet, G., The upper mantle under western Europe inferred from the dispersion of Rayleigh modes, *J. Geophys.*, *43*, 265–285, 1977.

Nolet, G., and M.J.R. Wortel, Mantle, upper: structure. in *The Encylopedia of Solid Earth Geophysics*, edited by D.E. James, pp. 775–788, Van Nostrand Reinhold, New York, 1989.

Nguyen-Hai, Propagation des ondes longitudinales dans le noyau terrestre, *Ann. Geophys.*, *15*, 285–346, 1963.

Oliver, J., On the long period character of shear waves, *Bull. Seismol. Soc. Am.*, *51*, 1–12, 1961.

Olson, P., P.G. Silver, and R.W. Carlson, The large-scale structure of convection in the Earth's mantle, *Nature*, *344*, 209–215, 1990.

Owens, T.J., G. Zandt, and S.R. Taylor, Seismic evidence for an ancient rift beneath the Cumberland Plateau, Tennessee: A detailed analysis of broadband teleseismic *P* waveforms, *J. Geophys. Res.*, *89*, 7783–7795, 1984.

Owens, T.J., S.R. Taylor, and G. Zandt, Crustal structure at Regional Seismic Test Network stations determined from inversion of broadband teleseismic *P* waveforms, *Bull. Seismol. Soc. Am.*, *77*, 631–662, 1987.

Paulssen, H., Upper mantle converted waves beneath the NARS array, *Geophys. Res. Lett.*, *12*, 709–712, 1985.

Paulssen, H., Evidence for a sharp 670-km discontinuity as inferred from *P*-to-*S* converted waves, *J. Geophys. Res.*, *93*, 10,489–10,500, 1988.

Poirier, J.P., On the kinetics of olivine–spinel transition, *Phys. Earth Planet. Inter.*, *26*, 179–187, 1981.

Price, G.D., A. Wall, and S.C. Parker, The properties and behaviour of mantle minerals: a computer simulation approach, *Philos. Trans. R. Soc. London, Ser. A*, *328*, 391–407, 1989.

Revenaugh, J., and T.H. Jordan, Observations of first-order mantle reverberations, *Bull. Seismol. Soc. Am.*, *77*, 1704–1717, 1987.

Revenaugh, J., and T.H. Jordan, A study of mantle layering beneath the western Pacific, *J. Geophys. Res.*, *94*, 5787–5813, 1989.

Revenaugh, J., and T.H. Jordan, Mantle layering from *ScS* reverberations, 2, The transition zone, *J. Geophys. Res.*, in press, 1991*a*.

Revenaugh, J., and T.H. Jordan, Mantle layering from *ScS* reverberations, 3, The upper mantle, *J. Geophys. Res.*, in press, 1991*b*.

Richards, M.A., and C.W. Wicks, *S–P* conversion from the transition zone beneath Tonga and the nature of the 670 km discontinuity, *Geophys. J. Int.*, *101*, 1-35, 1990.

Richards, P.G., Seismic waves reflected from velocity gradient anomalies within the Earth's upper mantle, *J. Geophys.*, *38*, 517–527, 1972.

Ringwood, A.E., *Composition and Petrology of the Earth's Mantle*. 604 pp., McGraw-Hill, New York, 1975.

Ringwood, A.E., Phase transformations and differentiation in subducted lithosphere, implications for mantle dynamics, basalt petrogenesis, and crustal evolution, *J. Geol.*, *90*, 611–643, 1982.

Ringwood, A.E., and T. Irifune, Nature of the 650-km seismic discontinuity: Implications for mantle dynamics and differentiation, *Nature*, *331*, 131–136, 1988.

Safar, M.H., What is the area required for reflecting a seismic pulse?. paper presented at the 51st Meeting of the European Association of Exploration Geophysics, Berlin, May 29 – June 2, 1989.

Schubert, G., D.A. Yuen, and D.L. Turcotte, Role of phase transitions in a dynamic mantle, *Geophys. J. R. Astron. Soc.*, *42*, 705–735, 1975.

Shearer, P.M., Seismic imaging of upper mantle structure with new evidence for a 520-km discontinuity, *Nature*, *344*, 121–126, 1990.

Shearer, P.M., Imaging global body-wave phases by stacking long-period seismograms, *J. Geophys. Res.*, in press, 1991.

Shearer, P.M., and T.G. Masters, Global seismic record sections – Data and synthetics, *Eos Trans. AGU*, *71*, 1465, 1990.

Silver, P.G., R.W. Carlson, and P. Olson, Deep slabs, geochemical heterogeneity, and the large-scale structure of mantle convection: Investigation of an enduring paradox, *Annu. Rev. Earth Planet. Sci.*, *16*, 477–541, 1988.

Simpson, D.W., R.F. Mereu, and D.W. King, An array study of *P*-wave velocities in the upper mantle transition zone beneath northeastern Australia, *Bull. Seismol. Soc. Am.*, *64*, 1757–1788, 1974.

Suito, K., Phase relations of pure MG_2SiO_4, up to 200 kilobars, in *High-Pressure Research in Mineral Physics*, edited by M.H. Manghnani and Y. Syono, pp. 255–266, Terra Scientific, Tokyo, 1977.

Sung, C.-M., and R.G. Burns, Kinetics of high-pressure phase transformations: Implications to the evolution of the olivine → spinel transition in the downgoing lithosphere and its consequences on the dynamics of the mantle, *Tectonophysics*, *31*, 1–32, 1976a.

Sung, C.-M., and R.G. Burns, Kinetics of the olivine → spinel transition: implications to deep-focus earthquakes, *Earth Planet. Sci. Lett.*, *32*, 165–175, 1976b.

Tanimoto, T., Long-wavelength *S*-wave velocity structure throughout the mantle, *Geophys. J. Int.*, *100*, 327–336, 1990.

Vinnik, L.P., Detection of waves converted from *P* to *SV* in the mantle, *Phys. Earth Planet. Inter.*, *15*, 39–45, 1977.

Vinnik, L.P., R.A. Avetisjan, and N.G. Mikhailova, Heterogeneities in the mantle transition zone from observations of *P*-to-*SV* converted waves, *Phys. Earth Planet. Inter.*, *33*, 149–163, 1983.

Vinnik, L.P., G.L. Kosarev, and L.I. Makeyeva, Anisotropy of the lithosphere from the observations of *SKS* and *SKKS* (in Russian), *Proc. Acad. Sci. USSR*, *278*, 1335–1339, 1984.

Vinnik, L.P., R. Kind, G.L. Kosarev, and L.I. Makeyeva, Azimuthal anisotropy in the lithosphere from observations of long-period S-waves, *Geophys. J. Int.*, *99*, 549–559, 1989.

Wajeman, N., Detection of underside P reflections at mantle discontinuities by stacking broadband data, *Geophys. Res. Lett.*, *15*, 669–672, 1988.

Walck, M.C., The *P*-wave upper mantle structure beneath an active spreading centre: The Gulf of California, *Geophys. J. R. Astron. Soc.*, *76*, 697–723, 1984.

Ward, S.N., Long-period reflected and converted upper mantle phases, *Bull. Seismol. Soc. Am.*, *68*, 133–153, 1978.

Weber, M., and J.P. Davis, Evidence of a laterally variable lower mantle structure from *P*- and *S*-waves, *Geophys. J. Int.*, *102*, 231–255, 1990.

Weidner, D.J., and E. Ito, Mineral physics constraints on a uniform mantle composition, in *High-Pressure Research in Mineral Physics*, edited by M.H. Manghnani and Y. Syono, pp. 269–274, Terra Scientific, Tokyo, 1987.

Weidner, D.J., H. Sawamoto, S. Sasaki, and M. Kumazawa, Single-

crystal elastic properties of the spinel phase of Mg_2SiO_4, *J. Geophys. Res.*, *89*, 7852–7860, 1984.
Whitcomb, J.H., and D.L. Anderson, Reflection of $P'P'$ seismic waves from discontinuities in the mantle, *J. Geophys. Res.*, *75*, 5713–5728, 1970.
Wiggins, R.A., and D.V. Helmberger, Upper mantle structure of the western United States, *J. Geophys. Res.*, *78*, 1870–1880, 1973.
Woodhouse, J.H., and A.M. Dziewonski, Mapping of the upper mantle: Three-dimensional modeling of Earth structure by inversion of seismic waveforms, *J. Geophys. Res.*, *89*, 5953–5986, 1984.
Woodward, R.L., and G. Masters, Global upper mantle structure from long-period differential travel times, *J. Geophys. Res.*, *96*, 6351–6377, 1991.

P. M. Shearer, Institute of Geophysics and Planetary Physics, Scripps Institution of Oceanography, University of California, San Diego A-025, La Jolla, CA 92093.

(Received January 28, 1991;
revised June 7, 1991;
accepted May 3, 1991.)